An Experimental And Theoretical Study Of The Confined Vortex With High Flow Rate.

SHAKESPEARE, WALTER JEFFREY

AN EXPERIMENTAL AND THEORETICAL STUDY OF THE CONFINED VORTEX WITH HIGH FLOW RATE

Lehigh University PH.D. 1979

PLEASE NOTE:

In all cases this material has been filmed in the best possible way from the available copy. Problems encountered with this document have been identified here with a check mark ✓.

1. Glossy photographs _____
2. Colored illustrations _____
3. Photographs with dark background _____
4. Illustrations are poor copy _____
5. Print shows through as there is text on both sides of page _____
6. Indistinct, broken or small print on several pages _____ throughout _____
7. Tightly bound copy with print lost in spine _____
8. Computer printout pages with indistinct print _____
9. Page(s) 86 lacking when material received, and not available from school or author ✓
10. Page(s) _____ seem to be missing in numbering only as text follows _____
11. Poor carbon copy _____
12. Not original copy, several pages with blurred type _____
13. Appendix pages are poor copy _____
14. Original copy with light type _____
15. Curling and wrinkled pages _____
16. Other _____

AN EXPERIMENTAL AND THEORETICAL STUDY OF THE CONFINED VORTEX WITH HIGH FLOW RATE

by

Walter Jeffrey Shakespeare

A Dissertation
Presented to the Graduate Committee
of Lehigh University
in Candidacy for the Degree of
Doctor of Philosophy

in

Mechanical Engineering

Lehigh University
1979

Approved and recommended for acceptance as a dissertation in partial fulfillment of the requirements for the degree of Doctor of Philosophy.

September 25, 1979
(date)

Edward K. Levy
Professor in Charge

Accepted September 25, 1979
(date)

Special committee directing the doctoral work of
Walter Jeffrey Shakespeare

Edward K Levy
Chairman

Raymond J Emrich

John C. Thon

Bert Phillips

ACKNOWLEDGEMENT

This work was done under a National Science Foundation Energy Taineeship and a grant from the United States Department of Energy. The author would like to express the deepest gratitude to Professor Edward K. Levy not only for making possible the opportunity to do this work but also for his constant guidance and encouragement throughout the program. Special thanks to my wife whose patience and belief in me never waivered throughout the years of study.

TABLE OF CONTENTS

NOMENCLATURE

A	Constant in hot wire calibration equation
a	Finite difference grid spacing ratio
B	Constant in hot wire calibration equation
$b_{\frac{1}{2}}$	Half width of probe wake
C	Elements of finite difference coefficient matrices
d	Diameter of probe tip
E	Anemometer output voltage
H	Nondimensional height of boundary layer grid
h	Nondimensional grid spacing in region I analysis
i	Radial finite difference grid index
j	Axial finite difference grid index
K	Angular hot wire calibration constant
L	Chamber height
M	Number of axial nodel positions
N	Number of radial nodel positions
n	Constant in hot wire calibration equation
P	Pressure
p	Nondimensional pressure ($P/\rho U_0^2$)
Q	Volumetric flow rate
q	Nondimensional flow rate ($Q/U_0 R_0^2$)
R	Radial coordinate
r	Nondimensional radial coordinate (R/R_0)
S	Swirl (V_0/U_0)
t	Time

U	Radial velocity
u	Nondimensional radial velocity (U/U_0)
V	Tangential velocity
v	Nondimensional tangential velocity (V/U_0)
W	Axial velocity
w	Nondimensional axial velocity (W/U_0)
x	Distance coordinate
Z	Axial coordinate
z	Nondimensional axial coordinate (Z/R_0)

Greek

δ	Boundary layer thickness
θ	Azimuthal coordinate
μ	Dynamic viscosity
ν	Kinematic viscosity
ρ	Density
Φ	Potential function
ϕ	Nondimensional potential function (Φ/U_0R_0)
ω	Angular velocity

LIST OF FIGURES

List of Figures (continued) Page

List of Figures (concluded) Page

ABSTRACT

The subject of this investigation is the confined vortex flow of air inside a rotating cylindrical chamber. The air enters the chamber radially through the porous cylindrical surface and exits through an opening in one end. The general vortex phenomenon has been studied extensively in recent years. However, interest has generally focused on the case of dominant tangential velocity and relatively low throughflow. Unusual flow patterns resulting from the interaction of the viscous and centrifugal forces near the solid surfaces have been reported in the literature. These studies show that for strongly swirling flows the radial movement of fluid occurs close to the end walls and recirculation near the chamber midplane may occur. It has been found that the tangential velocity increases to a maximum at some radial position and then falls linearly to zero at the axis of symmetry. The resultant radial pressure distribution in the exit plane may cause a backflow of fluid into the chamber near the centerline. The extent to which these phenomena persist as the throughflow is increased is not addressed by any of the previous investigators.

The purpose of this work is to investigate the behavior of the flow field in the vortex chamber when the radial and tangential velocities are of equal order of magnitude at the cylindrical distributor and the Reynolds number based on chamber radius and radial velocity is of order 10^4.

A model is developed by piecing together the analyses for three regions, including the main part of the flow field, the portion near the end walls and the viscous core close to the axis of symmetry. It is shown that although the end wall secondary flow patterns persist, the end wall boundary layers may be uncoupled from the flow in the main region. An explanation for the variation in the size of the viscous core region with changes in operating parameters is presented and compared with a previous theory now used extensively in vortex modelling. Finally, a parametric analysis of the radial velocity profiles with changes in geometry has been done.

One of the applications of this work is to optimize the design of machines using this configuration. To investigate the behavior of the flow field as the geometry is altered, a parametric study was performed and comparison plots made for $R_o/L = 0.5$, 1.0, and 2.0. The short chamber exhibits the most uniform radial velocity profiles in Region I. The boundary layers appear to be much more sensitive to changes in swirl than to variation in geometry. There is a design tradeoff between minimizing the fraction of the chamber occupied by end wall boundary layers and minimizing the nonuniformity in radial velocity caused by larger aspect ratio.

I. INTRODUCTION

The subject of this investigation is the flow of air in a rotating cylindrical chamber (Figure 1). The chamber has impervious top and bottom end walls which rotate with the porous cylindrical surface. Air enters the chamber radially, moves inward toward the centerline, and flows out through the exit opening in the top end wall. This type of flow is known as a confined vortex, and it occurs in a number of practical devices including the cyclone dust separator, fluidic vortex valve, Ranque Hilsch tube, and various kinds of combustors. One such combustor - the centrifugal fluidized bed - is the motivation for the present work. This system operates with a mass of granular material held against the cylindrical surface by centrifugal force. The drag of the radial flow of air into the chamber tends to balance the centrifugal force on the particles, fluidizing the bed. Successful operation of the device is dependent upon the balance between body forces on the particles and the drag [1,2,3]. To understand the operating characteristics of the centrifugal fluidized bed, a thorough knowledge of the fluid mechanics inside the chamber is required. Particle trajectories, stability of operation, and the most favorable combustor geometry may be evaluated. Moreover, since the confined vortex occurs in many practical devices, the results of the work to be described in the following pages need not be limited to the centrifugal fluidized bed.

Essentially, there are two methods for creating the confined vortex. One method, described above, is to rotate the chamber. A

second technique is to inject the fluid tangentially into a stationary container. This method eliminates some of the rotating seals but reduces flexibility of operation. The second technique is by far the more common, having been studied much more extensively.

Lewellen [4] published a review of the literature containing nearly 500 references. Common practice is to divide the interior of the chamber into three regions (Figure 2).

i) Main Region (Region I)

ii) End Wall Boundary Layers (Region II)

iii) Viscous Core (Region III)

Since viscous effects play a dominant role in the development of the flow field, the Reynolds number is used to characterize the operating conditions. The two definitions of Re, used to reflect the operating parameters, angular velocity and flow rate, are:

$$Re_N = \frac{U_o R_o}{\nu} \qquad \text{Radial Reynolds Number}$$

$$Re_t = \frac{\omega R_o^2}{\nu} = \frac{V_o R_o}{\nu} \qquad \text{Tangential Reynolds Number}$$

The ratio of tangential to radial velocity at the distribuor is called the swirl, $S = V_o/U_o$. Most of the information available in the literature pertains to the case where $S \gg 1$ and/or $Re_N < 10^2$. Experimental data for $S \gg 1$ in a chamber with a stationary end wall has been obtained. Chang and coworkers [5,6] used a cylindrical screen over a stationary table with a hood and fan over the top.

Velocity profiles were taken inside the chamber. The screen rotation and fan capacity correspond to $Re_N \sim 10^2$ and $Re_t \sim 10^4$ to 10^6. Kotas [7] used an optical technique to determine velocities, exploring the flow in a static chamber with tangential injection. Savino and Keshock [12], using a pitot tube, measured velocities in a short vortex chamber with tangential injection. In each case the data show that in the vicinity of the end wall, Region II, the tangential velocity is reduced by viscous forces. Since the centrifugal force on a fluid particle is $\sim v^2/r$, the reduction in tangential velocity near the wall permits fluid to move down close to the wall and radially inward causing a rather large radial velocity overshoot (Figure 3). If the amount of radial flow through the end wall regions surpasses the total throughflow, there is recirculation in Region I (Figure 4). This has been shown analytically by Kuo [13] for the case of low Re_N by solving the full viscous equations numerically. In the main part of the chamber (Region I), the data show that there is a 1/r increase in tangential velocity as the centerline is approached. At some point, viscous forces limit this increase and there is a linear decrease in V to zero at the centerline. This is the viscous core (Region III). Some analytical work has been done to model the core region. In particular, the analysis of Rott [8] shows the characteristic peak in tangential velocity for laminar axisymmetric stagnation point flow with radial flow inward and a superimposed free vortex. Pressure distributions in the vortex chamber have been measured by Smithson [9] using a series of pressure taps in the bottom end wall. The results show a

significant pressure drop which increases as the centerline is approached. The pressure gradient is attributed to the centrifugal force of the swirling motion. Similar results were obtained by Roschke and Pivirotto [10]. Both studies show that the pressure drop is influenced by the size of the exit opening. Donaldson and Snedeker [11], using a pitot probe in the exit plane of an open-ended vortex chamber, showed that in Region III the pressure sometimes falls low enough to permit reverse flow, pulling fluid into the chamber (Figure 5).

Although a significant amount of data and analysis exists in each of the three regions for $S>>1$ and $Re_N < 10^2$, very little analysis and no data have been found for $S \mathcal{O} 1$ and $Re_N \mathcal{O} 10^4$. This is the region of operation of the centrifugal combustor.

Each region of the flow field is considered in this study. The goal of the work is to develop a model of the fluid mechanics to aid in centrifugal combustor design. Therefore, attention has been focused on a number of critical parameters. These include the radial, tangential and axial velocity distributions. The chamber pressure drop is also important from an operating and efficiency standpoint and must be related to the other operating parameters. In addition, it is important to identify any unstable operating modes or regions of recirculation or reverse flow.

II. REGION I

A. Experimental Investigation

1. Test Section

The experimental apparatus (Figure 8) consists of a porous cylindrical chamber 0.305 m in diameter and 0.159 m high, with impervious top and bottom end walls. The bottom wall is attached to a shaft which is driven by a variable speed electric motor. Air is supplied to the plenum chamber which completely surrounds the cylinder and is sealed by a teflon ring and metal sheet to the top wall of the chamber and to the shaft on the bottom. The top end wall contains the exit opening, 0.152 m in diameter and is constructed of 1.9 cm thick plexiglass. The cylinder is completely surrounded by honeycomb sections so that air is accelerated to the proper tangential velocity before reaching the distributor. The distributor in turn is wrapped with cloth to provide a pressure drop large enough to ensure even distribution of the air flow. The air supply system is capable of delivering approximately 0.378 m^3/s (800 scfm) to the chamber which is capable of angular velocities up to 42 sec^{-1} (400 rpm). The angular velocity of the chamber is determined by a calibrated strobe light focused on a mark on the chamber drive shaft. The air flow rate is determined with a pitot static probe oriented in the direction of flow at the supply duct centerline. Air flow calibration is carried out by measuring the dynamic pressure at a number of radial positions in the supply duct, computing the velocities, and then integrating the velocity profiles for

various flow rates. The measured flow rate is correlated with centerline dynamic pressure.

Most of the experiments were carried out using the apparatus described above, except for some early measurements in Region I. These were made on another device with essentially the same features, except that it operated at lower air flow rates and angular velocities.

2. *Anemometer System*

The investigation of the flow in Region I involves determining the three-dimensional velocity field at each point in the r-z plane, assuming tangential symmetry. A number of instruments have potential application for this type of measurement. Most commonly used are the 3D pitot static probe, hot wire anemometer, and laser-Doppler velocimeter (LDV). Because the LDV is capable of measurement without physically entering the flow field, it is very attractive for use in a swirling flow. However the system is quite expensive, particularly for three-dimensional work and it would be difficult to accurately align the system to probe through a moving plexiglass end wall or the exit opening. This type of probe seems most suitable for Region III since the laser source could be positioned at the chamber exit; and in Region III, the wake effects of a probe are most serious.

The pitot static probe is not well suited for measurements in a swirling flow for the following reasons. The strong centrifugal force field of the swirling motion results in static pressure

variations of unknown magnitude. Therefore, to measure the dynamic pressure the probe would first have to be aligned in the direction of the velocity vector so that a static pressure measurement could be obtained. This would be difficult to achieve accurately since the velocity magnitudes are relatively small. In addition, the very sensitive type of micromanometer needed to accurately measure these velocities has a very long response time. Because of the bulky mechanical linkage, interference with the flow, and relatively low directional accuracy this system is unattractive.

Because the pitot static approach is not well suited for this type of flow and an LDV was not available to the investigator, a hot wire anemometer system was used for all measurements in Regions I, II, and at the exit. Velocity measurements were carried out using a DISA 55D01 anemometer, 55D30 DC voltmeter with both hot wire and hot film probes. The probes have a cylindrical sensor supported at the ends by prongs molded into a ceramic body. Hot wire sensors are of platinum-rhodium wire; the film sensor is made of a quartz filament upon which a thin coating of nickel has been deposited. A schematic of the DISA system is shown in Figure 7.

The sensor resistance, which is a function of its temperature is measured by subtracting the resistances of the cables and supporting prongs from the measured total resistance.

$$R_s = R_{total} - R_{cables} - R_{leads}$$

This sensor resistance is multiplied by an overheat ratio, r', (1.8 for wires, 1.6 for films) and the operating resistance is

computed:

$$R_{operate} = r'R_s + R_{cables} + R_{leads} \quad .$$

This value of operating resistance is set on adjustable resistance dials and the probe is energized. Current flows through the sensor, generating heat which is transferred to the surroundings. Any imbalance between the heat generated and transferred causes a change in sensor temperature and resistance. The servo-amplifier detects the change in resistance as a bridge imbalance and responds by changing the voltage at the bridge top to maintain the sensor temperature at r' times ambient. The heat transfer from the sensor occurs principally by convection to the surrounding fluid and is influenced by both the magnitude and direction of the velocity with respect to the sensor. The voltage supplied by the servo-amplifier is a measure of the velocity.

3. Calibration Procedure

Each sensor is slightly different and must be calibrated to obtain accurate data. The calibration equipment is shown in Figure 7. A probe holder which is attached to the nozzle exit allows the probe to be oriented in each of three perpendicular directions without moving the probe tip. Air flows through the nozzle past the probe which is initially oriented so that the velocity vector is perpendicular to the sensor and in the plane of the supports. A number of velocities are measured with the pitot probe and micromanometer; and the voltages at the bridge top are recorded. The

micromanometer is manufactured by Flow Corporation and is reported to be accurate to ± 2 percent at the minimum dynamic pressures measured (0.1 mm H_2O).

Accepted procedure (14) is to correlate velocities using King's Law:

$$U^n = A + BE^2$$

The three constants in the calibration equation A, B, and n, are determined as follows. The measured velocities are raised to the power n = 0.3 to 0.8 and the variables U^n and E^2 are correlated by linear regression using a library routine [15]. One measure of the quality of fit [16] is the standard error of the estimate defined by

$$S = \{\sum_{j}^{N} (Y_j - (A + Bx_j)\}^2/(N-2)\}^{\frac{1}{2}}$$

This represents the standard deviation of the distribution of measured velocities about the regression line. For each value of n, A and B obtained when S is a minimum are the calibrated constants. A sample calibration curve is shown in Figure 9.

Next the probe is oriented with the velocity vector parallel to the sensor and finally perpendicular to both sensor and supports and for each orientation the procedure is repeated. The three-dimensional calibration equation is:

$$u_{eff}^n = K_1^2 u_x^2 + u_y^2 + K_2^2 u_z^2$$

Using this equation and the King's Law calibration, K_1 and K_2 may be

determined. Although K_1 and K_2 are usually assumed constant, it has been found that each is influenced by the magnitude of the velocity vector. Fitting this variation with a least square parabolic equation improves the accuracy somewhat. Typical curves for K_1 and K_2 are shown in Figures 10 and 11.

When the probe has been calibrated for angular response, it is possible to determine each of the three components of velocity by orienting the probe in the three perpendicular directions in a flow field, and recording the voltages.

4. Experimental Procedure

The calibration procedure for the probe is carried out at the temperature of the air leaving the calibration nozzle. To ensure that the calibration remains valid in case the temperature changes, the probe total resistance is measured with the probe inside the test chamber with air flowing. The operating resistance is determined in the same way as during calibration so that the temperature difference between probe and surrounding fluid is always the same. Then assuming the convective heat transfer coefficient is essentially uninfluenced by small changes in the film temperature, the heat dissipation for a given fluid velocity will remain the same.

Orientation of the probe in the test section has been accomplished using a probe holder designed to allow angling the probe 45° up or down to reach into the corners. This procedure also reduces the possibility of wake interference in regions of high tangential velocity. The probe and holder are positioned by means of a

traversing mechanism located on top of the plenum chamber. The traversing mechanism allows horizontal motion of the carriage on two parallel shafts, motion is controlled by a threaded rod and handle. The vertical movement of the trolley is accomplished in two ways. In Region I of the chamber, relatively large movements of ~0.25 cm are desirable. This is accomplished with a threaded rod similar to the horizontal system. The trolley is split into two sections both on the vertical shaft. The top section is threaded onto the rod but the bottom is free to slide and is connected to the top by a micrometer. Fine vertical movements of $\sim 10^{-3}$ cm may be made with the micrometer. This is important near the end walls, in Region II.

In the early experiments, there were some problems with contamination of the air with particles. The particles would strike the 5μ diameter hot wire sensor causing damage. The solution to this problem was to use a film probe which is mechanically much stronger. Although film probes have poorer frequency response characteristics than hot wires, it is very well suited for the measurements made in this study.

The experimental procedure is to place the probe in one orientation and move it vertically, recording the voltages at radial positions of 0.9 R_o, 0.75 R_o, 0.50 R_o, and 0.25 R_o as shown in Figure 12. Next, the probe orientation is changed and the process repeated.

5. *Results*

To interpret the data, a computer program has been written. The flow diagram is shown in Figure 13. The recorded voltages are entered for each orientation and fit with a cubic spline using a library routine [15]. When the voltages for each of the three orientations at a specific set of positions have been found, the calibration equations are used to find the values of the velocity components. A check is made on K_1 and K_2 and, after iterating to convergence, the results are printed. Figure 14 shows a plot of the nondimensional radial velocity as a function of dimensionless chamber height at radial positions of $r = 0.90$, 0.75, 0.50, and 0.25. The chamber aspect ratio is $R_o/L = 1$ and the conditions are $Re_N = 1.8 \times 10^4$ and $Re_t = 1.6 \times 10^4$. The profiles are nonuniform with height showing an increasing radial velocity as the top end wall is approached. The nonuniformity becomes more pronounced with decreasing radius. The profiles at $r = 0.25$ are not considered reliable for reasons discussed in Chapter IV. The solid lines in Figures 14 through 16 are theoretical results; and these are discussed in the next section.

The tangential velocity profiles are plotted on the same format (Figure 15). Figure 17 shows the tangential velocity as a function of radius. The magnitudes increase with decreasing radius in approximately the same way at each axial position. The axial velocities are shown in Figures 16 and 18 plotted as function of height and radius respectively. The axial velocity increases to a maximum at a height of about $z = 0.8$ and then decreases toward zero at the

top end wall. The magnitude of the axial velocity generally increases with decreasing radius as shown in Figure 18. Figures 19, 20, and 21 are plots of the nondimensional radial, tangential and axial velocities with height for a chamber aspect ratio $R_o/L = 2$ at the radial positions of $r = 0.9$, 0.75, and 0.50. The conditions in this case are $Re_N = 1.8 \times 10^4$ and $Re_t = 1.6 \times 10^4$. The data exhibit the same general features as for $R_o/L = 1$.

To determine the effects of viscous forces on the flow, a series of experiments was performed. The angular velocity (i.e. tangential Reynolds number) was held constant, and the velocity profiles were obtained for a variety of air flow rates (i.e. radial Reynolds numbers), as shown in Figures 23a through 23c. A similar procedure is followed for constant Re_N and various Re_t (Figures 23a through 23c). The data positions form a cross on the flow regime map (Figure 24) and cover the practical range of operation of the experimental apparatus. Despite the wide variation in the operating parameters the prominent features of the data persist. There appear to be no clear trends with changing Reynolds number. Each of the profiles shows the same basic characteristics discussed above. This suggests that the effects of Reynolds number on the flow field in Region I are probably small.

6. Sources of Uncertainty

A general discussion of the propagation of error through the hot wire system and calibration is contained in Appendix A. However, certain other types of error may be present because of the

experimental apparatus, and should be discussed. These include:

i) Natural or centrifugal convection. Convection effects due to the swirling flow could affect the heat transfer. It would seem that these effects would be more pronounced if the probe itself were rotating than in the present system since, with a stationary sensor, the fluid boundary layer on the probe surface has a minimal streamline curvature. Very little data exist even for the rotating probe problem and a quantitative extimate has not been attempted. Instead, the radial velocity profiles inside the chamber have been integrated and compared with the measure flow rate from the supply duct. Agreement to within 10 percent is obtained and therefore any centrifugal convection effects, if present, would seem to be minimal.

ii) Wake interference. Wake interference could result if the wake of the fluid past the probe tip is swept around and into the tip again. The problem would occur in regions of low radial and axial velocity and high tangential velocity. An estimate of the effect has been made from the growth of a two-dimensional wake [17]. If the probe tip is considered to be a circular cylinder of width $d = 0.25$ cm, the half width of the wake is known to vary as:

$$b_{\frac{1}{2}} = \frac{1}{4} (xC_D d)^{\frac{1}{2}}$$

For a tangential velocity relative to the probe of ~100 cm/s, the Reynolds number based on probe diameter is:

$$Re_d = \frac{Vd}{\nu} = 168.2$$

and

$$C_D \cong 1.0$$

$$b_{\frac{1}{2}} = \frac{1}{4}\,(x \cdot 1.0 \cdot 0.25)^{\frac{1}{2}}$$

where

$$x = 2\pi R$$

For this wake to be swept clear, a particle of fluid must move radially a distance $b_{\frac{1}{2}}$ for each tangential motion of $2\pi R$. Hence

$$\frac{v}{u} < \frac{2\pi R}{\frac{1}{4}\,(2\pi R d)^{\frac{1}{2}}} = 4\ (2\pi R/d)^{\frac{1}{2}}$$

A similar criterion involving the axial velocity may be employed. A check on the experimental data indicates that the criteria are satisfied throughout Region I for the conditions measured.

iii) Positioning the probe. The probe position is determined both radially and axially by a scale attached to the traversing mechanism and graduated in 0.01 inch increments. The position of the probe tip is therefore assumed correct to $\pm$ 0.025 cm. The sensor element is approximately 0.25 cm long and this dimension must be considered the size of a "point" at which the velocity is determined. In Region I, changes in velocity are negligible over this distance according to the data. The effects of the orientation of the probe with respect to the velocity vector are discussed in Appendix A. However, some of the data have been taken for the

same conditions with two different orientations and the results agree to within the experimental accuracy stated.

iv) Radiation. Radiation from the sensor is known to make an appreciable contribution to the total heat transfer only in the immediate vicinity of a wall i.e. 0.025 cm away [18].

v) Distributor. The design and construction of the distributor has been one of the most troublesome of the experimental problems. In the original apparatus a number of porous foam rubber layers surrounded the perforated metal distributor. Perfectly symmetrical distribution of the air is quite difficult to achieve and a number of configurations were tried before satisfactory results were obtained. In the second apparatus, a layer of closely woven cloth surrounds the metal distributor on the outside with a layer of foam rubber 1.2 cm thick inside. The distributor with cloth and foam is sealed by silicon sealant to the top and bottom walls. Experimental data for Region I were obtained in both pieces of apparatus and the same behavior was observed. This fact, coupled with the results of pressure drop measurements for both freeboard and distributor to be discussed in Chapter IV, show that the behavior is not related to the distributor design.

vi) Conduction to supports. Conduction to the supports as well as natural convection become significant only at very low velocities of the order 30 - 40 cm/s [14]. Although one component may at times be less than this, the magnitude of the velocity vector is always much larger in Region I, for the conditions measured.

B. Theoretical Analysis

1. Formulation

Based on the results of Section A, it appears that the flow patterns in Region I are relatively insensitive to Reynolds number. This has led to the explanation of the flow field in terms of an inviscid, irrotational model. The Euler momentum equation in vector form for the flow of an inviscid fluid is:

$$\frac{D\vec{V}}{dt} = -\frac{1}{\rho}\,\vec{\nabla}P - \vec{\nabla}\Omega$$

The circulation is defined as

$$\Gamma = \int_C \vec{V}\cdot d\vec{r}$$

Hence

$$\frac{D\Gamma}{Dt} = \int \frac{D\vec{V}}{Dt}\cdot d\vec{r}$$

$$\frac{D\Gamma}{Dt} = \int \left(-\frac{1}{\rho}\,\vec{\nabla}P - \vec{\nabla}\Omega\right)\cdot d\vec{r}$$

and for P, ρ, and Ω single valued scalar functions we have

$$\frac{D\Gamma}{Dt} = 0$$

If there is no initial circulation for a reducible circuit, in the r-z plane, $\Gamma = 0$ throughout. From Stokes theorem

$$\int \vec{V}\cdot d\vec{r} = \int_A (\vec{\nabla}\times\vec{V})\cdot d\vec{A}$$

Hence, $\vec{\nabla}\cdot\vec{V} = 0$ and from the vector identity $\vec{\nabla}\times\vec{\nabla}\Phi = 0$ let

$\vec{V} = \vec{\nabla}\Phi$ where Φ is a single valued scalar field function. For the flow of an incompressible fluid, conservation of mass requires: $\vec{\nabla} \cdot \vec{V} = 0$. Hence $\vec{\nabla} \cdot \vec{\nabla}\Phi = 0$ which is Laplace's equation or $\nabla^2\Phi = 0$. The geometry of concern is a circular cylinder. Expressing Laplace's equation in cylindrical coordinates:

$$\frac{1}{R}\frac{\partial}{\partial R}\left(R\frac{\partial \Phi}{\partial R}\right) + \frac{1}{R^2}\frac{\partial^2 \Phi}{\partial \theta^2} + \frac{\partial^2 \Phi}{\partial Z^2} = 0 \qquad (1)$$

where

$$u = \frac{\partial \Phi}{\partial R} \quad (a) \qquad V = \frac{\partial \Phi}{\partial \theta} \quad (b) \qquad W = \frac{\partial \Phi}{\partial Z} \quad (c) \qquad (2)$$

The solution is best obtained by dividing the problem into two separate problems, and since the equation is linear, adding the equations:

$$\Phi(R,\theta,Z) = \Phi_1(\theta) + \Phi_2(R,Z) \qquad (3)$$

2. Solution Procedure

The first problem corresponds to pure tangential velocity in the chamber. The governing equation is:

$$\frac{1}{R^2}\frac{d^2\Phi_1}{d\theta^2} = 0 \qquad (4)$$

Subject to the boundary condition

$$\frac{1}{R_o}\frac{d\Phi_1}{d\theta}\bigg|_{R_o} = V(R_o) = \omega R_o \qquad (5)$$

Since

$$\frac{d^2\Phi_1}{d\theta^2} = 0 \quad , \quad \frac{d\Phi_1}{d\theta} = \text{constant} = \omega R_o \tag{6}$$

$$V = \frac{\omega R_o^2}{R} \quad \text{a free vortex} \tag{7}$$

The 1/R singularity in the tangential velocity distribution makes the model invalid as the centerline of the chamber is approached. Therefore the model applies only to Region I and it is convenient to define the boundary between Regions I and III as a cylinder of radius R_c, through which there is no radial flow. The justification for imposing this condition is a result of measurements of the axial velocity in the exit plane and will be discussed in greater detail in Chapter IV. With this constraint the second problem becomes

$$\frac{1}{R}\frac{\partial}{\partial R}\left(R\frac{\partial\Phi_2}{\partial R}\right) + \frac{\partial^2\Phi_2}{\partial Z^2} = 0 \tag{8}$$

Subject to the boundary conditions:

$$R = R_o \qquad -\frac{\partial\Phi_2}{\partial R} = u_o \tag{9}$$

$$R = R_c \qquad \frac{\partial\Phi_2}{\partial R} = 0 \tag{10}$$

$$Z = 0 \qquad \frac{\partial\Phi_2}{\partial Z} = 0 \tag{11}$$

$$\begin{aligned} &Z = L \\ &R \geq R_E \quad \frac{\partial\Phi_2}{\partial Z} = 0 \\ &R < R_E \quad \Phi_2 = 1 \end{aligned} \tag{12}$$

The last condition at the exit is the result of the need for a Dirichlet boundary condition on the problem. It corresponds to having the streamlines in the R-Z plane straight, parallel, and perpendicular to the exit.

Because of the discontinuity in boundary conditions at the exit it was necessary to solve the second problem numerically. Nondimensionalizing equation (8) with respect to U_o and R_o,

$$r = \frac{R}{R_o} \quad z = \frac{Z}{R_o} \quad u = \frac{U}{U_o} \quad w = \frac{W}{U_o} \quad \phi = \frac{\Phi_1}{R_o U_o} \tag{13}$$

equation (8) may be rewritten:

$$\frac{\partial^2 \phi}{\partial u^2} + \frac{1}{r}\frac{\partial \phi}{\partial r} + \frac{\partial^2 \phi}{\partial z^2} = 0 \tag{14}$$

The r-z plane was divided into a finite difference network (Figure 25). The derivatives in equation (14) may be represented by finite difference approximations. These approximations are derived for the general case of variable grid spacing in Appendix B. Making use of equations (B9) and (B10) with $a = 1$, equation (14) may be written at the position i,j:

$$\frac{\phi_{i-1,j} - 2\phi_{i,j} + \phi_{i+1,j}}{(\Delta r)^2} + \frac{1}{4}\frac{\phi_{i+1,j} - \phi_{i-1,j}}{2\Delta r}$$

$$+ \frac{\phi_{i,j-1} - 2\phi_{i,j} + \phi_{i,j+1}}{(\Delta z)^2} = 0$$

Let the grid positions be equally spaced; $\Delta r = \Delta z = h$ and rearrange the governing equation:

$$\left(1 - \frac{1}{2(i + \frac{r_c}{h})}\right) \phi_{i-1,j} - 4\phi_{i,j} + \left(1 + \frac{1}{2(i + \frac{r_c}{h})}\right) \phi_{i+1,j}$$

$$+ \phi_{i,j-1} + \phi_{i,j+1} = 0$$

The boundary conditions, equations (9) - (12) are:

$$\left.\frac{\partial \phi}{\partial r}\right|_{r=1} = 1 \qquad \phi_{N+1,j} = \frac{1}{3}(-2h + 4\phi_{N,j} - \phi_{N-1,j})$$

$$\left.\frac{\partial \phi}{\partial r}\right|_{r=r_c} = 0 \qquad \phi_{0,j} = \frac{1}{3}(4\phi_{1,j} - \phi_{2,j})$$

$$\left.\frac{\partial \phi}{\partial z}\right|_{z=0} = 0 \qquad \phi_{i,0} = \frac{1}{3}(4\phi_{i,1} - \phi_{i,2})$$

$$\left.\frac{\partial \phi}{\partial z}\right|_{z=\ell} = 0 \qquad r \geq r_E \quad \phi_{i,N+1} = \frac{1}{3}(4\phi_{i,m} - \phi_{i,m-1})$$

$$\phi/z = \ell = 1.0 \qquad r < r_E \quad \phi_{i,m+1} = 1.0$$

Introducing the grid numbering scheme shown in Figure 25, allows a statement of the equations in compact, banded matrix form. Let

$$C_1 = \left(1 - \frac{1}{2(i + \frac{r_o}{r})}\right)$$

$$C_2 = -4$$

$$C_3 = \left(1 + \frac{1}{2(i + \frac{r_o}{r})}\right)$$

$$C_4 = 1$$

$$C_5 = 1$$

The resultant banded matrix system represents M x N equations in M x N unknown interior values of the potential. A library routine [15] for banded matrix inversion and storage has been used to solve the system of equations. When the values of potential have been computed, the radial and axial velocities may be found using equations 2a and 2c. Figures 14 through 16 show plots of the computed radial, tangential, and axial velocities superimposed on the experimental data. The error bands shown on the data represent probable upper bound calculated on the basis of the analysis presented in Appendix A.

3. Results

It can be seen that the features noted in the experimental data are shown by the theory. The convergence of the streamlines near the top wall as the fluid moves towards the exit results in the vertical nonuniformity of the radial velocity. The way in which the fluid is directed toward the opening causes the peak observed in the axial velocity at $Z/L = 0.8$, and the increase in axial velocity with decreasing radius. A qualitative picture of the streamline is shown in Figure 26. The theoretical profiles in Figures 19 and 21, for the aspect ratio $R_o/L = 2$ are similar to those discussed above but it is interesting to note that the nonuniformities in radial velocity with height are not as pronounced.

Measurement of three-dimensional velocity profiles in the confined vortex presents many experimental problems as discussed above. Therefore, the agreement between the measurements shown and a

theoretical prediction is not likely to be exact. The importance of the data is in revealing any trends and the sensitivity of those trends to variation of the operating parameters. The potential flow model for Region I exhibits the same trends as the data and in some respects the predictions are quite good. For this reason, it is believed that the flow in Region I may be adequately described mathematically by the simple inviscid-irrotational model.

III. REGION II

A. Analysis

One of the consequences of the existance of potential flow in Region I is that it makes it possible to partially uncouple this region from the flow in Region II. Once the potential flow has been calculated it can be used as the boundary condition for the boundary layer analysis close to the end walls. The validity of the approach depends on the thickness of the viscous layer and on the amount of fluid entrained in the boundary layer compared to the total through-flow. The approximation should work best for thin layers and relatively high through flow rates i.e. $Re_N >> 1$ and $Re_N \mathcal{O} Re_t$. An estimate of the thickness of the end wall layer based on the result for a flat plate (17) gives

$$\delta \mathcal{O} \left(\frac{\nu x}{u_\infty}\right)^{1/2}$$

Assuming $x \mathcal{O} R_o$

$$\frac{\delta}{R_o} \mathcal{O} \frac{1}{\sqrt{Re_N}}$$

For $Re_N \sim 10^4$

$$\frac{\delta}{R_o} \mathcal{O} 10^{-2}$$

The exact solution (17) for the case of stagnant fluid over a rotating plate or rotating fluid over a stationary plate yields:

$$\delta O\left(\frac{\nu}{\omega}\right)^{1/2} \qquad \frac{\delta}{R_o} O \frac{1}{\sqrt{Re_t}}$$

For $Re_t O 10^4$

$$\frac{\delta}{R_o} O\ 10^{-2}$$

It would appear that for large radial throughflow the boundary layer thickness criterion should be satisfied.

1. An Idealized Problem

The structure of the end wall boundary layers is governed by boundary conditions imposed by the main region potential flow. To explore the general behavior of the boundary layers, it is convenient to consider the problem shown in Figure 27. A line sink and free vortex exists on the axis of symmetry of a disk of radius R_o. The flow is assumed to move radially inward from the distributor toward the axis of symmetry with a uniform angular velocity of ω resulting in rigid body rotation on the plate and free vortex in the free stream. The solution is sought for values of R large enough to exclude the radial viscous effects of a core region. The solution is assumed to be laminar and the logical starting point for the analysis is the Navier-Stokes equations in cylindrical coordinates:

R - Momentum:

Steady Axisymmetric

$$\frac{\partial U}{\partial T} + u\frac{\partial U}{\partial R} + \frac{V}{R}\frac{\partial U}{\partial \theta} - \frac{V^2}{R} + w\frac{\partial U}{\partial Z} =$$

No Body Forces Axisymmetric

$$F_R - \frac{1}{\rho}\frac{\partial P}{\partial R} + \nu\left(\frac{\partial^2 U}{\partial R^2} + \frac{1}{R}\frac{\partial U}{\partial R} - \frac{U}{R^2} + \frac{1}{R^2}\frac{\partial U^2}{\partial \theta^2} - \frac{2}{R^2}\frac{\partial U}{\partial \theta} + \frac{\partial^2 U}{\partial Z^2}\right) \qquad (1)$$

θ - Momentum:

Steady Axisymmetric

$$\frac{\partial V}{\partial T} + U\frac{\partial V}{\partial R} + \frac{V}{R}\frac{\partial V}{\partial \theta} + \frac{UV}{R} + w\frac{\partial V}{\partial Z} =$$

No Body Force Axisymmetric

$$F_\theta - \frac{1}{\rho R}\frac{\partial P}{\partial \theta} + \nu\left(\frac{\partial^2 V}{\partial R^2} + \frac{1}{R}\frac{\partial V}{\partial R} - \frac{V}{R^2} + \frac{1}{R^2}\frac{\partial^2 V}{\partial \theta^2} + \frac{2}{R^2}\frac{\partial U}{\partial \theta} + \frac{\partial^2 V}{\partial Z^2}\right) \qquad (2)$$

Z - Momentum:

Steady

$$\frac{\partial W}{\partial T} + u\frac{\partial W}{\partial R} + \frac{V}{R}\frac{\partial W}{\partial \theta} + w\frac{\partial W}{\partial Z} =$$

No Body Force Axisymmetric

$$F_z - \frac{1}{\rho}\frac{\partial P}{\partial Z} + \nu\left(\frac{\partial^2 W}{\partial R^2} + \frac{1}{R}\frac{\partial W}{\partial R} + \frac{1}{R^2}\frac{\partial^2 W}{\partial \theta^2} + \frac{\partial^2 W}{\partial Z^2}\right) \qquad (3)$$

Continuity

Axisymmetric

$$\frac{\partial U}{\partial R} + \frac{U}{R} + \frac{1}{R}\frac{\partial V}{\partial \theta} + \frac{\partial W}{\partial Z} = 0 \qquad (4)$$

Nondimensionalize each of the variables:

$$u = \frac{U}{U_o} \qquad v = \frac{V}{U_o} \qquad w = \frac{W}{U_o} \qquad p = \frac{P}{PU_o^2} \qquad z = \frac{Z}{R_o} \qquad r = \frac{R}{R_o}$$

Equations (1) - (4) become

$$u \frac{\partial u}{\partial r} - \frac{v^2}{r} + w \frac{\partial u}{\partial z} = -\frac{\partial P}{\partial r} + \frac{1}{Re_N} \left[\frac{\partial^2 u}{\partial r^2} + \frac{1}{r} \frac{\partial u}{\partial r} - \frac{u}{r^2} + \frac{\partial^2 u}{\partial z^2} \right] \tag{5}$$

$$u \frac{\partial v}{\partial r} + \frac{uv}{r} + w \frac{\partial v}{\partial z} = \frac{1}{Re_N} \left[\frac{\partial^2 v}{\partial r^2} + \frac{1}{r} \frac{\partial v}{\partial r} - \frac{v}{r^2} + \frac{\partial^2 v}{\partial z^2} \right] \tag{6}$$

$$u \frac{\partial w}{\partial u} + w \frac{\partial w}{\partial z} = -\frac{\partial P}{\partial z} + \frac{1}{Re_N} \left[\frac{\partial^2 w}{\partial r^2} + \frac{1}{r} \frac{\partial w}{\partial r} + \frac{2}{\partial z^2} w \right] \tag{7}$$

$$\frac{\partial u}{\partial r} + \frac{u}{r} + \frac{\partial w}{\partial z} = o \tag{8}$$

For the problem under consideration, there is assumed to be a boundary layer of thin axial extent. Let the dimensionless boundary layer thickness by δ and $\delta << 1$ where as $v \mathcal{O} u \mathcal{O} 1$ and $r \mathcal{O} 1$. Dimensional analysis of the continuity equation yields:

$$\frac{\partial u}{\partial r} + \frac{u}{r} + \frac{\partial w}{\partial z} = o$$

$$\frac{\mathcal{O}(1)}{\mathcal{O}(1)} + \frac{\mathcal{O}(1)}{\mathcal{O}(1)} + \frac{\mathcal{O}(w)}{\mathcal{O}(\delta)} = o \quad \text{which implies } w \mathcal{O} \delta$$

Applying this result to the momentum equations:

$$u\frac{\partial u}{\partial r} - \frac{v^2}{r} + w\frac{\partial u}{\partial z} = -\frac{\partial p}{\partial r} + \frac{1}{Re_N}\left[\frac{\partial^2 u}{\partial r^2} + \frac{1}{r}\frac{\partial u}{\partial r} - \frac{u}{r^2} + \frac{\partial^2 u}{\partial z^2}\right] \qquad (5)$$

$$\frac{O(1)xO(1)}{O(1)} - \frac{O(1)}{O(1)} + \frac{O(\delta)xO(1)}{O(\delta)} =$$

$$O\left[\frac{\partial p}{\partial r}\right] + \frac{1}{O(Re_N)}\left\langle\left[\frac{O(1)}{O(1)} + \frac{O(1)}{O(1)} - \frac{O(1)}{O(1)} + \frac{O(1)}{O(\delta^2)}\right]\right\rangle$$

For inertial and viscous forces of the same order of magnitude, the equation implies

$$Re_N O\frac{1}{\delta^2} \quad \text{and} \quad \frac{\partial p}{\partial r} O\ \delta$$

$$u\frac{\partial w}{\partial r} + w\frac{\partial w}{\partial z} = -\frac{\partial p}{\partial z} + \frac{1}{Re_N}\frac{\partial^2 w}{\partial r^2} + \frac{1}{r}\frac{\partial w}{\partial r} + \frac{\partial^2 w}{\partial z^2} \qquad (7)$$

$$\frac{O(1)O(\delta)}{O(1)} + \frac{O(\delta)O(\delta)}{O(\delta)} = O\left[\frac{\partial p}{\partial z}\right] + O(\delta^2)\left\langle\left[\frac{O(\delta)}{O(\delta^2)} + \frac{O(\delta)}{O(1)} + \frac{O(\delta)}{O(\delta^2)}\right]\right\rangle$$

Equation (7) implies that $\frac{\partial p}{\partial z} O\delta$ and hence the pressure

is "impressed" on the boundary layer from the free stream as expected. It may be argued that in this type of flow the radial velocity overshoot which has been observed by other investigators is caused by a pressure imbalance in the boundary layer. Hence, neglecting this variation cancels a principal driving force. However, the free stream radial pressure gradient is balanced by the centrifugal force term $\frac{v^2}{r}$. The decreasing magnitude of the tangential velocity near the plate upsets the radial force balance which causes the velocity overshoot. Neglecting the pressure variation with height does not preclude this effect. Under the boundary layer assumptions, (5) - (7) become:

$$u \frac{\partial u}{\partial r} - \frac{v^2}{r} + w \frac{\partial u}{\partial z} = -\frac{\partial p}{\partial z} + \frac{1}{Re_N} \left[\frac{\partial^2 u}{\partial z^2}\right] \tag{9}$$

$$u \frac{\partial u}{\partial r} + \frac{uv}{r} + w \frac{\partial v}{\partial z} = \frac{1}{Re_N} \left[\frac{\partial^2 v}{\partial z^2}\right] \tag{10}$$

$$u \frac{\partial w}{\partial r} + w \frac{\partial w}{\partial z} = -\frac{\partial p}{\partial z} + \frac{1}{Re_N} \left[\frac{\partial^2 w}{\partial z^2}\right] \tag{11}$$

Subject to the boundary conditions

$$u(1,z) = -1 \qquad u(r,o) = 0 \qquad u(u,h) = -\frac{1}{r}$$

$$v(1,z) = S \qquad v(r,o) = Sr \qquad v(v,h) = \frac{S}{r}$$

$$w(1,z) = 0 \qquad w(r,o) = 0$$

The radial pressure gradient may be computed from the

Bernoulli-Euler equation, which is valid in the free stream

$$p_o = p + \frac{1}{2}(u^2 + v^2 + w^2)$$

$$p_o = p + \frac{1}{2}\left[\frac{1}{r^2} + \frac{S^2}{r^2}\right]$$

$$\frac{\partial p}{\partial r} = \frac{1}{r^3}(1 + S^2)$$

The techniques commonly used to obtain solutions to the above system of equations fall into three broad categories including:

(i) Similarity Transformations: The existance of a similarity solution would be very useful for this idealized problem. However, the similarity solutions exist only for certain radial pressure variations and therefore it is not feasible to couple these solutions to the numberically computed potential flow in Region I. Because the r dependence of the tangential velocity component is not the same in the free stream as it is on the plate, a similarity profile is not expected at each radial location even for the idealized case. It may be possible to build up similarity solutions but this would be difficult and because of the need to fit the result with a computed free stream potential flow this avenue was not pursued.

(ii) Momentum Integral: The momentum integral approach is useful in determining certain overall characteristics of the flow such as the torque required to drive the plate. Since the profile shapes

are assumed at the outset, it appears that this method would yield the least information about the flow field.

(iii) Numerical: Numerical techniques are particularly well suited to the solution of equations in parabolic form. An algorithm can be constructed to represent the differential equations implicitly in the cross stream direction, and when the components have been computed at a radial position, the calculation proceeds to the next position, marching in the streamwise direction to complete the flow field. If a region of reverse flow should occur at some point, this type of algorithm fails. However, this would invalidate the assumed form of the governing equations. In this respect, it may be sufficient to know that the equations are not valid and that the flow separates without actually calculating the velocity field after separation.

2. Finite Difference Representation

In an attempt to minimize the number of grid positions needed for an accurate solution to the equations, the finite differences in the cross stream direction have been written with variable grid spacing (Appendix B). Other investigators [19] have noted that the problems of stability associated with the marching procedure can be minimized using "upwind" differences to represent the convective terms. Accordingly, and making use of equations (B1) and (B10), equations (9) and (10) become at the position $i + 1, j$

$$u_{i,j}\left[\frac{u_{i,j} - u_{i+1,j}}{\Delta r}\right] - \frac{v_{i,j}}{r_{i+1}}\,(v_{i+1,j}) + w_{i,j}\left[\frac{u_{i+1,j+1} - u_{i+1,j-1}}{(1+a)\,\Delta z}\right] =$$

$$-\frac{1}{r^3}\,(1 + S^2) + \frac{1}{Re_N}\left[\frac{a u_{i+1,j+1} - (1+a) u_{i+1,j} + u_{i+1,j-1}}{\frac{a}{2}\,(1+a)\,\Delta z^2}\right] \qquad (13)$$

$$u_{i,j}\left[\frac{r_{i,j} - v_{i+1,j}}{\Delta r}\right] + \frac{u_{i,j}\,v_{i+1,j}}{v_{i+1}} + w_{i,j}\left[\frac{v_{i+1,j+1} - v_{i+1,j-1}}{(1+a)\,\Delta z}\right] =$$

$$\frac{1}{Re_N}\left[\frac{a v_{i+1,j+1} - (1+a)\,v_{i+1,j} + v_{i+1,j-1}}{\frac{a}{2}(1+a)\,(\Delta z)^2}\right] \qquad (14)$$

When the values of u and v have been determined for all j at i + 1, the continuity equation (8) may be used to determine the axial velocities:

$$\frac{u_{i,j} - u_{i+1,j}}{\Delta r} + \frac{u_{i+1,j}}{r_{i+1}} + \frac{w_{i+1,j+1} - w_{i+1,j}}{\Delta z} = 0 \qquad (15)$$

Since the pressure has been assumed to be uniform through the boundary layer, equations (8), (9) and (10) have been solved for the unknown u, v and w. Equation (11) is not needed. The equations have been written such that computation begins at 1 - r and proceeds radially inward toward the centerline. Rearranging the equations (13) - (15) and grouping coefficients:

$$\left[\frac{-w_{i,j}}{(1+a)\Delta^2} - \frac{1}{Re_N \frac{a}{2}(1+a)(\Delta z)^2}\right] u_{i+1,j-1}$$

$$+ \left[\frac{-u_{i,j}}{\Delta r} + \frac{(1+a)}{Re_N \frac{a}{2}(1+a)\,\Delta z^2}\right] u_{i+1,j}$$

$$+ \left[\frac{w_{i,j}}{(1+a)\Delta z} - \frac{a}{Re_N \frac{a}{2}(1+a)(\Delta z)^2}\right] u_{i+1,j+1}$$

$$+ \left[\frac{-v_{i,j}}{v_{i+1}}\right] v_{i+1,j} = \frac{1}{r^3}(1+\delta^2) - \frac{u_{i,j}}{\Delta r} \qquad (16)$$

$$\left[\frac{-w_{i,i}}{(1+a)\Delta z} - \frac{1}{Re_N \frac{a}{2}(1+a)\,\Delta z^2}\right] v_{i+i,j-1}$$

$$+ \left[\frac{-u_{i,j}}{\Delta r} + \frac{u_{i,j}}{r_{i+1}} + \frac{(1+a)}{Re_N \frac{a}{2}(1+a)\,\Delta z^2}\right] v_{i+1,j}$$

$$+ \left[\frac{w_{i,j}}{(1+a)\Delta z} - \frac{a}{Re_N \frac{a}{2}(1+a)\,\Delta z^2}\right] v_{i+1,j+1} = \frac{-u_{i,j}\,v_{i,j}}{\Delta r} \qquad (17)$$

$$w_{i+1,j+1} = \Delta z \left[\frac{w_{i+1,j}}{\Delta z} - \frac{u_{i+1,j}}{r_{i+1}} - \frac{r_{i,j} - u_{i+1,j}}{\Delta r}\right] \qquad (18)$$

$$C_1 = \left[\frac{-w_{i,j}}{(1+a)\ \Delta z} - \frac{1}{Re_N \frac{a}{2} (1+a)\ \Delta z^2}\right] \quad C_4 = \frac{-v_{i,j}}{r_{i+1}}$$

$$C_2 = \left[\frac{-u_{i,j}}{\Delta r} + \frac{(1+a)}{Re_N \frac{a}{2} (1+a)\ \Delta z^2}\right] \quad RHS_1 = \left[\frac{-1}{r^3}(1+S^2) - \frac{u_{i,j}^2}{\Delta r}\right]$$

$$C_3 = \left[\frac{w_{i,i}}{(1+a)\ \Delta z} - \frac{a}{Re_N \frac{a}{2} (1+a)\ \Delta z^2}\right]$$

$$C_5 = \left[\frac{-w_{i,j}}{(1+a)\ \Delta z} - \frac{1}{Re_N \frac{a}{2} (1+a)\ \Delta z^2}\right]$$

$$C_6 = \left[\frac{-u_{i,j}}{\Delta r} + \frac{u_{i,j}}{r_{i+1}} + \frac{1+a}{Re_N \frac{a}{2}(1+a)\ \Delta z^2}\right]$$

$$C_7 = \left[\frac{w_{i,j}}{(1+a)\ \Delta z} - \frac{a}{Re_N \frac{a}{2} (1+a)\ \Delta z^2}\right]$$

$$RHS_2 = \frac{-u_{i,j}\ v_{i,j}}{\Delta r}$$

Equations (16) and (17) become

$$C_1\ u_{i+1,j-1} + C_2\ u_{i+1,j} + C_3\ u_{i+1,j+1} + C_4\ v_{i+1,j} = RHS_1$$

$$C_5\ v_{i+1,j-1} + C_6\ v_{o+1,j} + C_7\ v_{i+1,j+1} = RHS_2$$

The system of equations written in matrix form for a 10 point cross stream finite difference grid is:

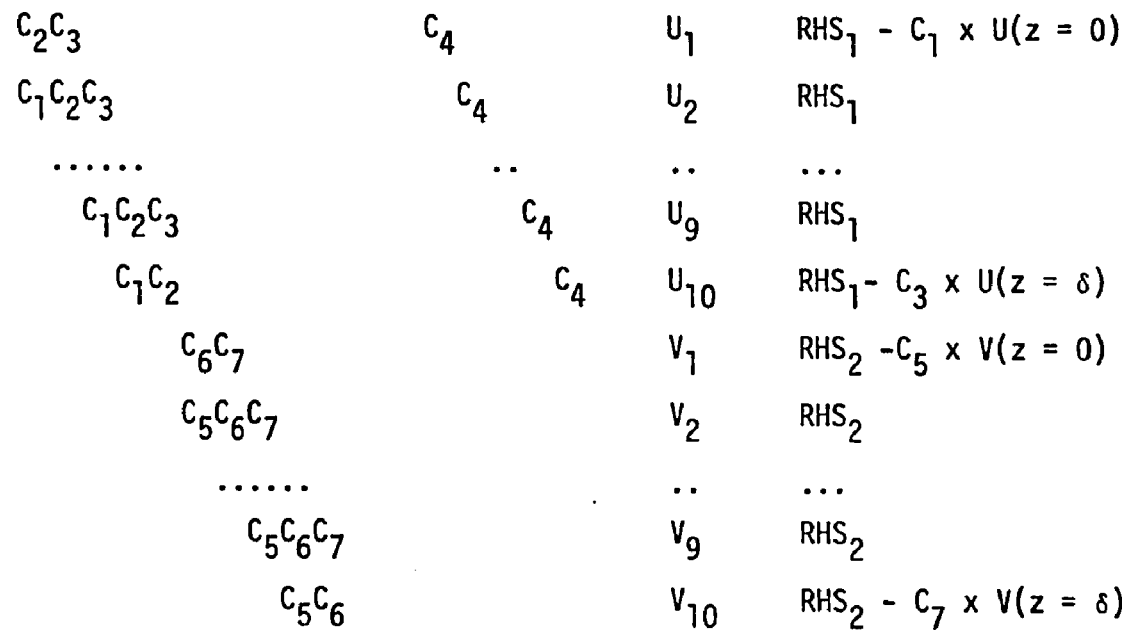
C_2C_3 C_4 U_1 $RHS_1 - C_1 \times U(z = 0)$
$C_1C_2C_3$ C_4 U_2 RHS_1
....
$C_1C_2C_3$ C_4 U_9 RHS_1
C_1C_2 C_4 U_{10} $RHS_1 - C_3 \times U(z = \delta)$
C_6C_7 V_1 $RHS_2 - C_5 \times V(z = 0)$
$C_5C_6C_7$ V_2 RHS_2
....
$C_5C_6C_7$ V_9 RHS_2
C_5C_6 V_{10} $RHS_2 - C_7 \times V(z = \delta)$

The set of simultaneous equations is inverted at each radial position using a library routine [15] for banded matrices. Results for the radial and tangential velocity profiles for $Re_N = 10^3$, S = 1 are shown in Figures 29 through 30. Results for a Reynolds Number $Re_N = 10^3$ and swirl S = 1 indicate a typical boundary layer thickness of less than 0.01 of the chamber radius, confirming the original assumption about the layer thickness. A slight overshoot in radial velocity is noticeable at r = 0.25.

3. Accuracy of the Solution

The following checks were made on the algorithm:

(i) Satisfaction of the original finite difference equations at random points to within the accuracy of the approximations

(ii) Approach to the boundary conditions

(iii) Convergence of values for decreasing r and z step sizes

(iv) Physically reasonable behavior

Because of the variable grid spacing used in the cross stream direction, an analytical estimate of the numerical truncation error is difficult. Therefore, in addition to the usual checks on the algorithm it is useful to compare the results with some known solution. Equations (8) and (9) for the finite disk reduce to the boundary layer equations for flow over a flat plate at large r, since the second term in each of the equations approaches

zero as $r \to \infty$. The solution to this classic problem by means of a similarity transformation is due to Blasius. If the numerical solution to our idealized problem is correct, then it should match the Blasius solution for $r >> 1$ and $S = 0$. Figure 31 is a comparison plot for a point 0.5 from the leading edge of a disk with radius $r = 10^3$. Fifty axial grid points have been used with a grid spacing ratio $a = 0.9$ and streamwise steps of 0.005. The Reynolds Number is $Re_N = 10^3$. The agreement is good and it is believed that the algorithm is functioning correctly.

4. Imposition of the Calculated Potential Flow

The program described above may be used to compute the boundary layers on the top and bottom end walls of the chamber by substituting the values of radial velocity and pressure gradient calculated for Region I in place of the line sink values. The calculation of the potential flow field in Region I must be made using a specific core size. The appropriate size will be discussed in Chapter IV, however, the core size is a function of the angular velocity of the chamber. Therefore, the proper sequence of computation is to:

(i) Specify the chamber geometry

(ii) Specify the operating parameters

(iii) Calculate the core size

(iv) Calculate the potential flow using the computed core size

(v) Calculate the boundary layer using the potential flow.

5. Limitations in the Analysis

As discussed above, the analysis is valid only at radii larger than the core radius. In addition, the layer has to be thin and only a small fraction of the total flow may pass through the layer. Figure 32 shows the values of $B = \frac{M_{BL}}{M_Z}$ holding either Re_N or Re_t constant. Typical values are $B0 \quad 10^{-3}$ so the above assumptions appear justified.

The streamlines calculated for Region I diverge with decreasing radius near the bottom end wall and therefore the radial velocity decreases. Figure 33 shows the theoretical radial pressure gradient along the bottom end wall. For values of swirl less than about 0.5 an adverse pressure gradient exists. Under these conditions, the analysis predicts the development of an inflection point in the radial velocity profile before the algorithm diverges. An example of the profile development with the adverse pressure gradient is shown in Figure 34 for $S = 0$ $Re_N = 10^4$ and a chamber $R_o/L = 1$, $r_E = 0.5$.

B. Experiment

1. Procedure

The results of the analysis for Region II indicate a boundary layer thickness on the bottom wall of less than 0.05 of the cham-

ber height (0.75 cm). The top end wall layer thickness is about 0.02 of the chamber height (0.30 cm). Because the top wall layer, is thin and the features of development are less interesting, measurements have been confined to the bottom wall region.

The measurement technique must insure that the probe is positioned accurately with respect to the wall and moved in precise intervals. The precision of motion near the wall is accomplished with the micrometer on the probe traversing mechanism, which permits accurate movements of less than 0.003 cm. The technique used to position the probe a known distance from the wall is illustrated in Figure 35. A block of metal of known thickness is placed on the chamber bottom. Next, the mirror is tilted so that the top surface of the block appears as a line. Finally, the probe tip is moved into the line. Since the ray of light seen in the mirror must be parallel to the surface of the block which in turn is parallel to the chamber bottom, and since the probe tip is aligned with this ray of light, the tip must be a distance equal to the block thickness from the wall.

It is necessary to insure that the traversing mechanism moves the probe radially parallel to the plate and that the plate rotates essentially in a plane. The probe holder is positioned so that a dummy probe is close enough to the surface to just permit a sheet of paper to be moved between probe and plate. As the chamber is rotated or the probe moved radially, the tightness of

the paper may be checked. Gross inaccuracies in mounting would cause the paper to either bind or loosen. Since the paper is ~ 0.008 cm thick the mounting should be accurate to a fraction of this.

The component of velocity perpendicular to the end wall is small in the immediate vicinity of the wall. In addition, to determine the three dimensional velocity vector, at least one of the sensor positions must lie outside of a plane parallel to the wall. The sensor itself is ~ 0.25 cm in length. Therefore, the practical method of measurement in Region II is to assume that the velocity is two dimensional, and to make traverses with the probe in two perpendicular positions in a plane parallel to the end wall.

The experimental procedure is similar to that used in Region I. The probe in one orientation is moved vertically in steps of 0.127 cm from a height of 1.27 cm above the plate. The last two steps are 0.06 cm. Traverses are made at r = 0.8, 0.7, 0.6, 0.5, and 0.4. The conditions at which data have been taken are shown numbered 2 in Figure 24. Experimental results with theoretical predictions superimposed are shown in Figures 36.

2. Results

The radial velocity profiles for $Re_N = 10^4$ and S = 1 with an aspect ratio of $R_o/L = 1$ (Figure 36a) show a typical boundary layer variation at r = 0.8 from zero velocity at the wall to the free stream value at a height $Z/R_o = 0.04$. As the radius decreases an

inflection point develops and overshoot occurs at about 0.50. This overshoot becomes more pronounced at r = 0.4.

The tangential velocity increases from the value $v_o = \omega r$ on the plate to the free stream potential $v_\theta = \frac{S}{r}$ at the axial position of 0.02. This is approximately the height of the inflection point in the radial velocity. Figures 32c show radial velocities for $Re_N = 10^4$ and S = 2. At the larger swirl, the position of the first noticeable overshoot is at a larger radius, and the magnitude of the overshoot is greater. The height of the inflection point is lower and this is apparently the result of the thinner tangential boundary layer as shown in Figure

Figure 36e shows the radial boundary layer for $Re_N = 10^4$ and S = 5. In this case overshoot begins almost immediately at r = 0.8, the layer is quite thin, δ 0.01, and the peak radial velocity is about 12 times the free stream velocity.

Figures 36g through 36h are for the conditions Re_N 5 x 10^3 and S = 2. The principle difference between these and the profile for $Re_N = 10^4$ and S = 2 is that the boundary layer is thicker (δ = 0.02 for $Re_N = 10^4$ and δ = 0.025 - 0.03 for $Re_N = 5 \times 10^3$).

The data for the tangential velocity appear to agree well with the theory. The radial profiles do not agree nearly as well. However, the radial velocity data appear to show the same characteristics as the theory, i.e. overshoot at the appropriate positions, approximately correct boundary layer thickness, and correct trends with changing conditions. Figures 37 and 38 show

theoretical variation of profiles with swirl holding Re_N constant, at radii of 0.8 and 0.4 respectively. Figures 39 and 40 are profiles for the same conditions determined experimentally.

3. Uncertainties

Wake effects would certainly be present at some axial position in the boundary layer, since the fluid on the plate rotates with it and the radial velocity there is zero. The minimum safe distance from the plate may be found using the criteria discussed in Section II.A.6. The value is less than the minimum axial measuring position for all measured conditions. Near wall radiation effects, as discussed II.A.6, are only significant much closer to the wall. The discrepancy between measured and theoretical radial velocities is primarily thought to be due to slight nonuniformities in the distributor with θ, and imperfections in the smoothness of the bottom end wall.

IV. REGION III

A. Experiment

The experimental technique used in Region I is not suited for Region III because of the strong wake effects there. Instead, velocity measurements have been confined to the exit plane. The purpose of the measurements is to gain insight into governing phenomena behind changes in the core size, and axial and tangential velocity profiles with operating conditions of the chamber. In the absence of concrete data for the whole of Region III, the assumption of uniform core size with height has been made. The analysis for Regions I and II are rather insensitive to the specified core size except near the core and the exit. Parameters affecting the size of the core include exit radius, Re_N, and Re_t. Therefore experiments have been carried out using four different exit sizes r_E = 0.167, 0.250, 0.333, and 0.50.

1. Reverse Flow Detection

Some investigators have reported reverse flow in the core for certain conditions. A hot wire anemometer system cannot be used to determine whether the velocity vector is positive or negative. Therefore, a different system must be used in conjunction with the hot wire to correctly interpret the exit plane data.

A two dimensional or "cobra" pitot probe is oriented so that the probe axis is parallel to the exit plane and the probe tip is

on the centerline. The two ports are connected to a differential pressure manometer. The exit velocity vector contains primarily tangential and axial components. If the velocity is positive, up and out of the chamber; the fluid should impact the lower port, then separate and develop a lower pressure region behind the upper port. Conversely for the flow into the chamber, the pressure should be higher on the upper port. With the probe in place, the air flow rate is set to some value. Next the angular velocity of the chamber is increased slowly until the two water columns of the manometer are equal and then the upper port side dips below by a small amount. At this value of angular velocity, there is reverse flow along the axis of the chamber. A plot of the positions determined this way for $r_E = 0.5$ is shown in Figure . There appears to be some flow dependence. However, as the error bands indicate, the procedure relies on determining the first visible pressure differential from the manometer. Therefore, the results should be regarded as a general indication of the region where reverse flow is expected, not a measure of the relative dependence of the phenomenon on Re_t vs. Re_N.

2. Velocity Profiles

The velocity measurement technique in the exit is virtually identical to that used in Region I except that the probe is traversed radially across the exit opening. The procedure is to obtain a set of radial and tangential velocity profiles for fixed Re_N at four different Re_t, then a similar set for three different Re_N at

fixed Re_t. The results for each of the four exit radii are shown in Figures 41a through 41h. The negative velocities shown on some of the plots are based on the detection of reverse flow at the exit as described above and on the trends of the profiles. Obviously, some judgment is required in interpreting the data, but in general, the procedure is to assume that the axial velocity is negative at the radial position where the decreasing trend form the exit radius first begins to increase.

It is interesting to note the following general features of the data:

(i) the tangential velocity profile peaks at a radius slightly less than the maximum axial velocity and then declines toward zero.

(ii) The size of the region of diminished axial velocity increases with decreasing Re_N and with increasing Re_t.

(iii) The axial velocity profiles for $Re_t = 0$ are essentially uniform.

(iv) The region of uniform axial velocity for $Re_t = 0$ is somewhat smaller in radius than the exit indicating a vena contracta effect.

(v) The profiles for the largest exit opening show nearly uniform axial velocity from

r_E to some radial position where the values sharply decrease.

3. Pressure Drop

The last portion of the experimental investigation is the pressure drop measurements. The procedure is as follows:

(i) With the chamber top removed, the difference between plenum and atmospheric pressure is measured using a water manometer for a series of flow rates. The chamber rotation makes no detectable difference in the measurements. Assuming the velocity in the plenum chamber is negligible, this is the pressure drop associated with the increase in radial velocity from zero to U_0 plus the frictional pressure loss through the distributor, and will be called grid pressure drop. The curve is shown in Figure .

(ii) For each exit radius adjust the flow rate to a specific value and measure the difference between plenum and atmospheric pressure for a series of anglular velocities. Repeat for a number of flow rates. Follow the same procedure holding angular velocity constant and varying flow rate.

(iii) For each value of flow rate determine the grid pressure drop from Figure 42 and subtract from the measured total pressure difference. The result is the chamber pressure drop:

$$\Delta p_{chamber} = \Delta p_{total} - \Delta p_{grid}$$

B. Analysis

The core region is characterized by a peak and decrease in the tangential velocity and by a region of reduced or reversed axial velocity. The size of Region III affects the chamber pressure drop and the boundary condition for the analysis of Region I. Therefore, it is important to develop a model for the size of this region as a function of the operating parameters. Clearly, viscous effects are responsible for the decrease in tangential velocity near the axis of rotation. However, solving the full Navier-Stokes equations for this three dimensional flow region at high Reynolds numbers is a formidable problem. It may be that the core region is highly turbulent and also that the turbulence is not fully developed. In this case, a model is required for the dependence of shear stresses on local flow variables. Moreover, it is not clear that the dependence of core size on operating parameters is the result of viscosity. An idealized model which preserves the fundamental physical behavior of the core is preferred. The following assumptions are made:

(i) Potential flow exists in the region outside the radius of zero axial velocity. This is justified by the experiments which show that the peak in the tangential velocity profile occurs inside the position of reduced axial velocity.

(ii) The radial velocity is zero at the exit

radius in the exit plane. The streamlines converge from inside the chamber on the exit opening and diverge outside.

(iii) The position of the core is determined by the point where the axial velocity is zero and the pressure equals atmospheric pressure.

Since the flow is irrotational up to the core radius, the Bernoulli-Euler equation is valid throughout this portion of the exit plane:

$$p_o = p + \tfrac{1}{2}(u^2 + v^2 + w^2) \tag{1}$$

Since $\vec{\nabla} \times \vec{v} = 0 \qquad \frac{\partial w}{\partial r} - \frac{\partial u}{\partial z} = 0$

and $u << w$. Hence, perhaps $\frac{\partial w}{\partial r} \approx 0$. This is nothing more than assuming that w = constant across the exit to the core radius. At the exit radius in the exit plane, the static pressure is atmospheric and from assumptions (i) and (ii)

$$p_o = \frac{1}{2}\left[\frac{r^2}{r_E^2} + w^2\right] + p_A \tag{2}$$

At the core, according to assumption (iii)

$$p_o = \frac{1}{2}\frac{r^2}{r_c^2} + p_A \tag{3}$$

Equating (2) and (3)

$$\frac{1}{2}\frac{2}{r_c^2} + p_A = \frac{1}{2}\left[\frac{2}{r_E^2} + w^2\right] + p_A \tag{4}$$

$$w = \left[\frac{r^2}{r_c^2} - \frac{r^2}{r_E^2}\right]^{1/2} \tag{5}$$

and from (3)

$$r_c = \frac{r}{\sqrt{2(p_o - p_A)}} \tag{6}$$

Conservation of mass requires

$$q = \int_{r_c}^{r_E} 2\pi r\, w\, dr \tag{7}$$

For w = constant,

$$q = \pi\left[r_E^2 - r_c^2\right] w \tag{8}$$

Making use of (5) and (6) equation (8) becomes

$$q = \pi\left[r_E^2 - \frac{r^2}{2(p_o - p_A)}\right]\left[2(p_o - p_A) - \frac{r^2}{r_E^2}\right]^{1/2} \tag{9}$$

$$\left[\frac{a}{\pi r_E^2}\right]^{2/3} = \left[\left[2(p_o - p_A)\right]^{1/3} - \frac{r^2}{r_E^2}\left[2(p_o - p_A)\right]^{-2/3}\right]$$

Define $DP = \left[2(p_o - p_A)\right]^{1/3}$, $\quad \bar{w} = \dfrac{q}{\pi r_E^2}$

$$DP^3 = \bar{w}^{2/3}\, DP^2 - \frac{r^2}{r_E^2} = 0 \qquad (10)$$

Equation (10) was solved numerically using a successive substitution technique. The result of the process of solving equations (2), (3) and (7) simultaneously subject to assumptions (i) - (iii) are values for the variables r_C, $p_0 - p_A$ and w. The theory seeks to explain the presence of the region of low axial velocity. If a control volume of radius r_C and length L is considered about the chamber centerline, then a region of zero axial velocity from the top of the control volume must imply a region of zero radial velocity if Region III is assumed uniform with height. This is the basis for the boundary condition at r_C in Region I. Since the radial velocity falls to zero at r_C, the radial convection of angular momentum is also zero. The fluid in the core from r = 0 to r_C then rotates as a rigid body just as fluid inside a completely closed rotating container.

Since the tangential velocity is finite for $r < r_C$, the static pressure could fall below atmospheric causing reverse flow along the centerline. The prediction of this phenomenon would probably require the use of the viscous equations. It seems likely that viscous effects would tend to soften the sharp boundary between uniform and zero or negative axial velocity at r_C as shown

by the data. If sufficient axial momentum were carried in toward the centerline, the lower static pressure there could be counterbalanced and the axial velocity in Region III would be up and out of the chamber. Conversely, for a large core, reverse flow is very likely.

Figures 43a to 43d show the nondimensional pressure drop in the chamber for radii of 0.167, 0.25, 0.333, and 0.50. The solid line is the calculated pressure drop based on the above theory. In each case, the values for high swirl are seen to agree quite well. At lower swirl the data are somewhat higher than predicted by the theory. The position of departure from the theory appears to be at lower swirl as the exit radius is increased. One possible explanation for the disagreement is the existance of a vena contracta at the exit plane. This can be seen in some of the axial velocity profiles. The radial pressure gradient at higher swirl tends to affect this. A well designed nozzle at the exit would probably eliminate the effect. The only other analysis known to the author for predicting the size of the core region and chamber pressure drop is from Lewellen (4). The analysis is based on the concept of maximizing the flow rate through the exit with respect to overall chamber pressure drop. The predicted chamber pressure drop is shown by the dashed line in Figures 43a through 43d.

The theoretical definition of the core size is the point where the axial velocity drops to zero. Since the idealized pro-

file does not occur, a working definition of core size is required. Possibilities include the point of maximum tangential velocity, the point of sharp decline in axial velocity, zero axial velocity, or some intermediate point. The midpoint between the maximum and minimum axial velocities on the steep portion of the experimental profile has been chosen as the core size for the purpose of comparison with the theory. It can be seen from the velocity profiles (Figure 41) that the demarcation between core and main flow is not clear particularly at the smaller exit radii. The differences between the definitions for core size listed above are great. However, the purpose here is to compare trends and as long as the definition is consistent this is accomplished. Figures 44a through 44d show measured core sizes according to the above criteria versus the prediction, for the four exit radii. Results obtained from the analysis of Reference 4 are given by the dashed curves. Figure 45 shows the measured and predicted effect of exit radius on core size for a swirl of 4.93. Note that in each of the plots, the core radii have been nondimensionalized with respect to the exit radius rather than the usual chamber radius.

V. CONCLUSIONS

A model for the confined vortex flow of air in a rotating cylindrical chamber has been developed using the analyses for the three general regions of the flow field, including the main region, the end wall region and the viscous core. It is assumed that there is high radial throughflow and that the ratio of tangential to radial velocity is of order one at the outside radius of the chamber. It was found that the flow in the main region of the chamber may be treated as inviscid and irrotational. The size of the core region is determined by a simple inviscid pressure drop analysis based on the Bernoulli equation. The analysis predicts both the chamber pressure drop and the core radius. The end wall boundary layers are less than 5% of the chamber height for the range of parameters of interest i.e. $Re_N \geq 10^4$. As a result, the fraction of the total throughflow passing through the end wall layers is less than 1%.

As stated in Chapter III, the model presented herein is not valid for low radial Reynolds Number and high swirl. In this case, much of the previous work on the confined vortex is applicable. If the Mach number at the exit is greater than about 0.3, the assumption of incompressible flow breaks down. This represents an upper limit for practical application.

Transition to turbulence in both the core and the end walls is possible for large values of Re_t and Re_N. No turbulence was detected in the end wall layers for the conditions measured. The

core region is difficult to probe accurately with the hot wire technique and the existence of turbulence could not be confirmed there. This aspect of the problem is certainly in need of future work. Very little literature exists concerning theoretical transition, structure of the turbulent boundary layer either in the core or on the end wall, or the influence of wall roughness on transition and structure.

The assumption of uniform core size with height was made. Experimental investigation of the core region using a LDV probe and work on the structure at the core and end wall layer interaction region is much needed.

One of the applications of this work is to optimize the design of machines using this configuration. To investigate the behavior of the flow field as the geometry is altered, a parametric study was performed and comparison plots made for R_o/L = 0.5, 1.0, and 2.0. Results are shown in Figures 46a through 46i. The short chamber exhibits the most uniform radial velocity profiles in Region I. The boundary layers appear to be much more sensitive to changes in swirl than to variation in geometry. There is a design tradeoff between minimizing the fraction of the chamber occupied by end wall boundary layers and minimizing the nonuniformity in radial velocity caused by larger aspect ratio.

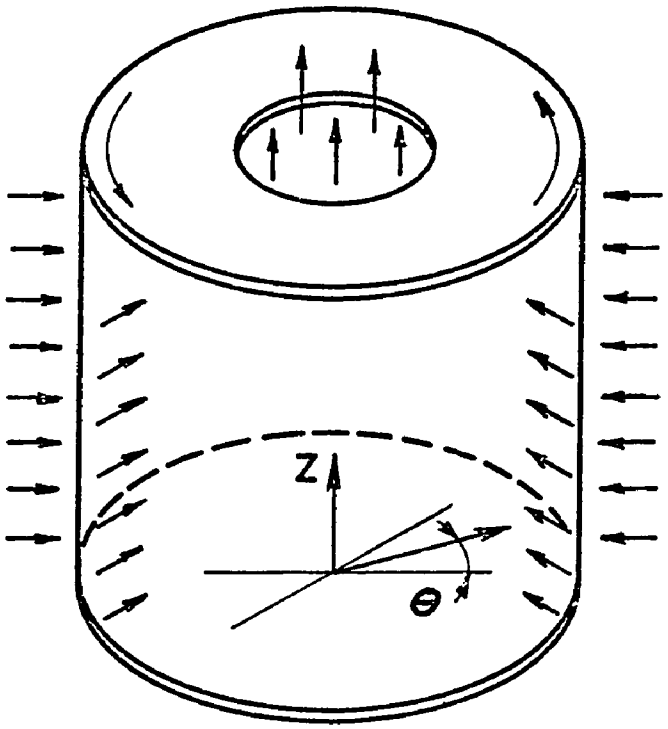

Figure 1 Confined vortex chamber

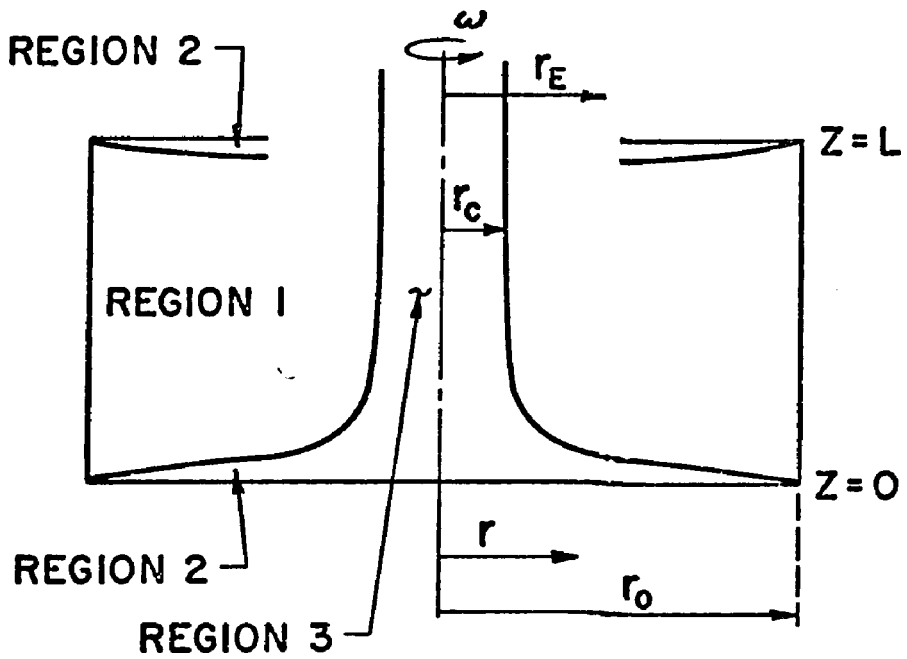

Figure 2 Regions of the flow

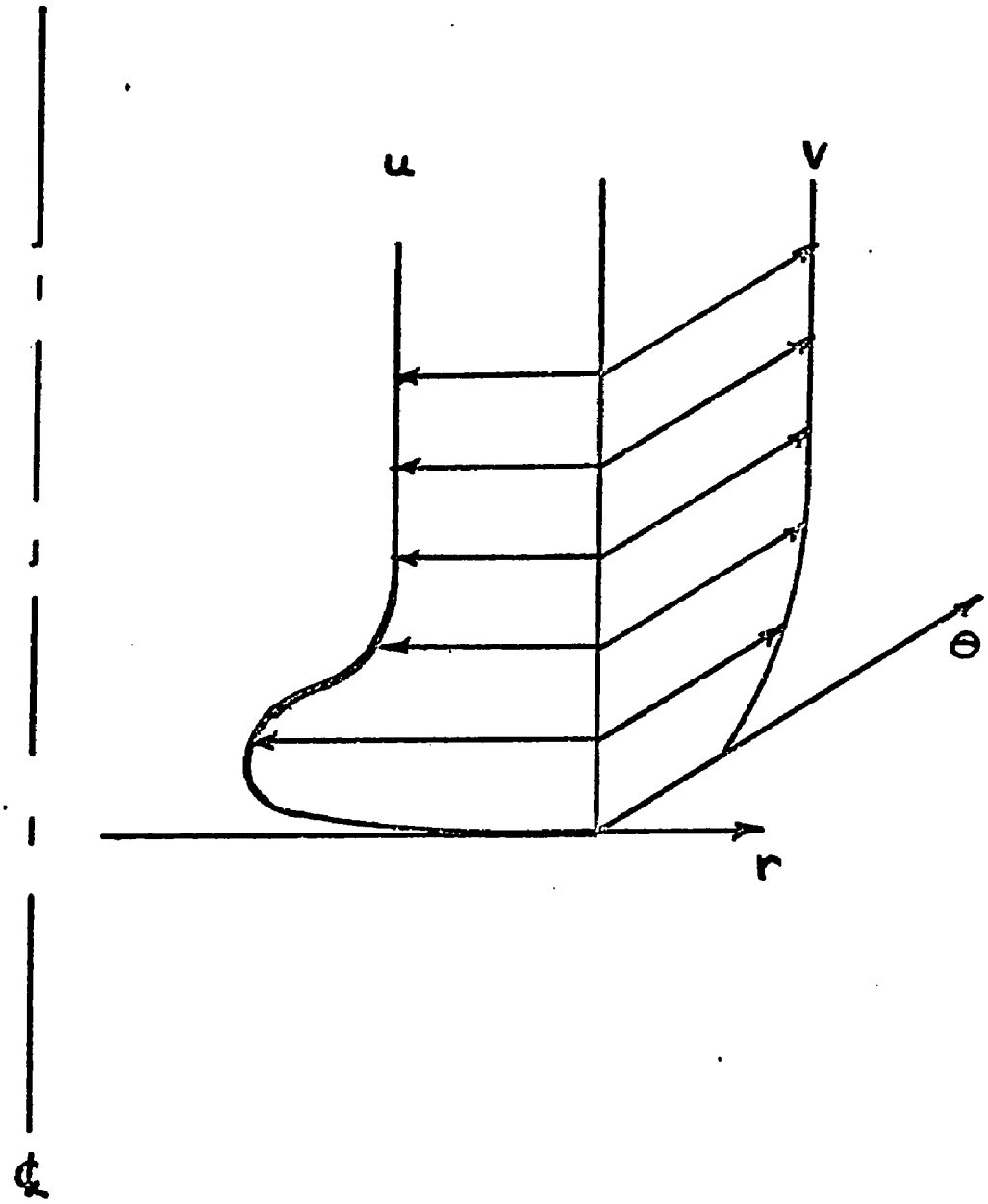

Figure 3 Velocity distribution near the end wall

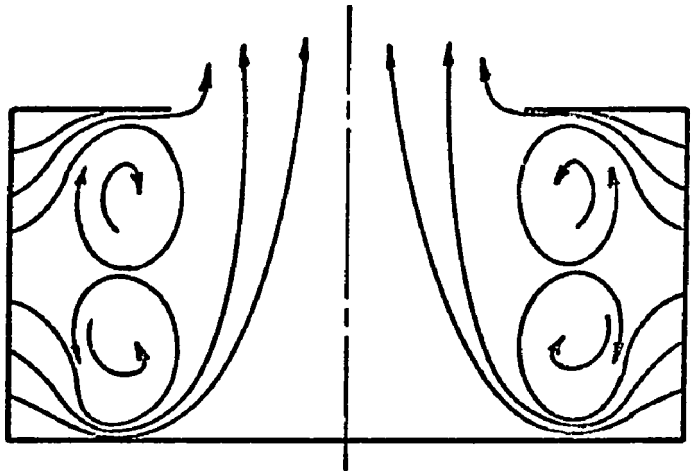

Figure 4 Flow patterns with high swirl

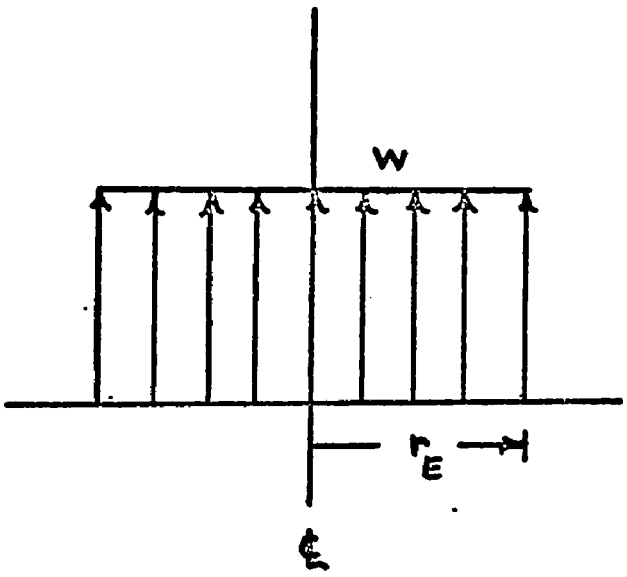

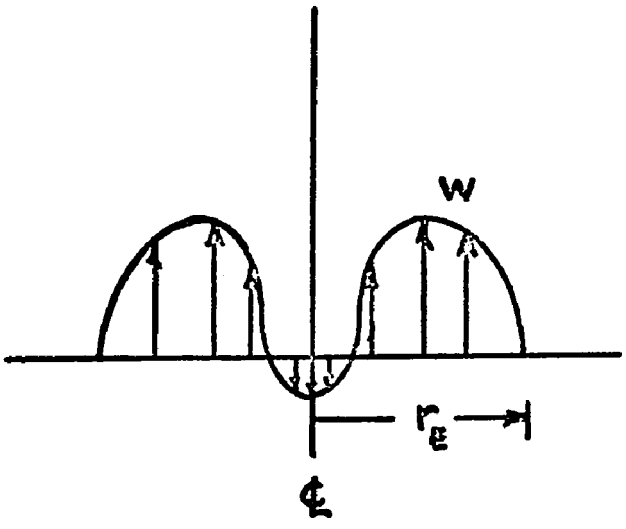

Figure 5 Exit plane flow patterns

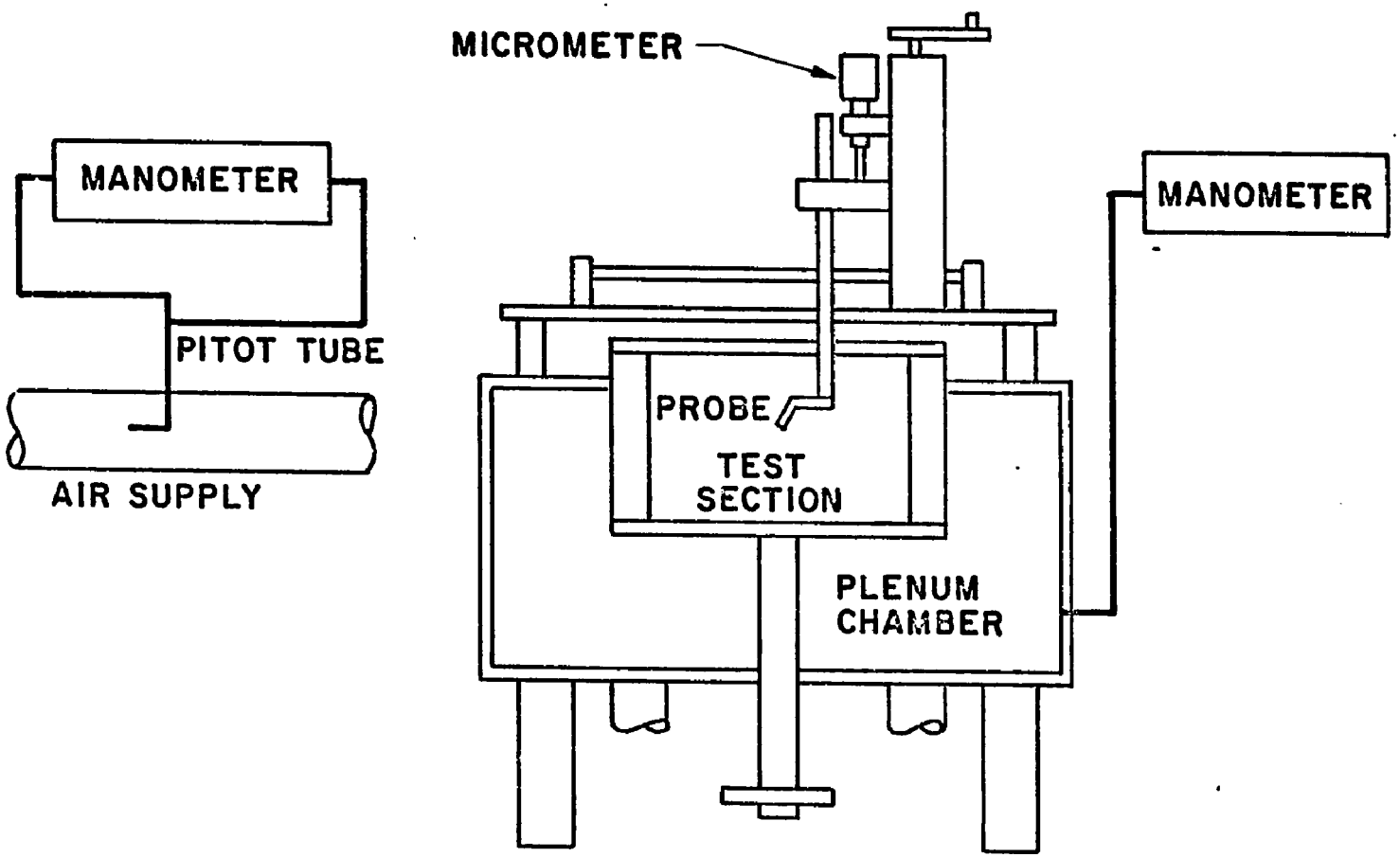

Figure 6 Experimental apparatus

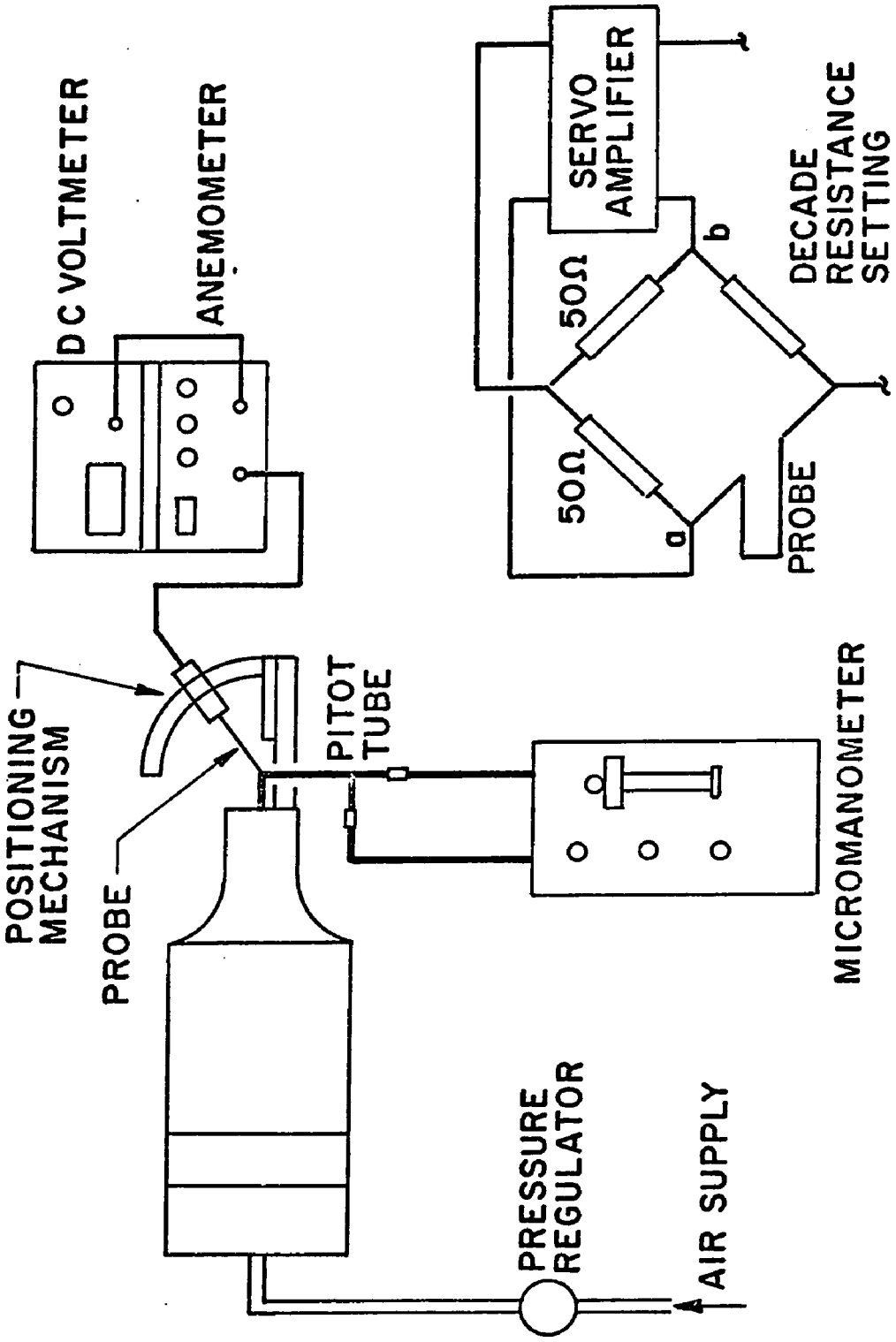

Figure 7 Calibration equipment

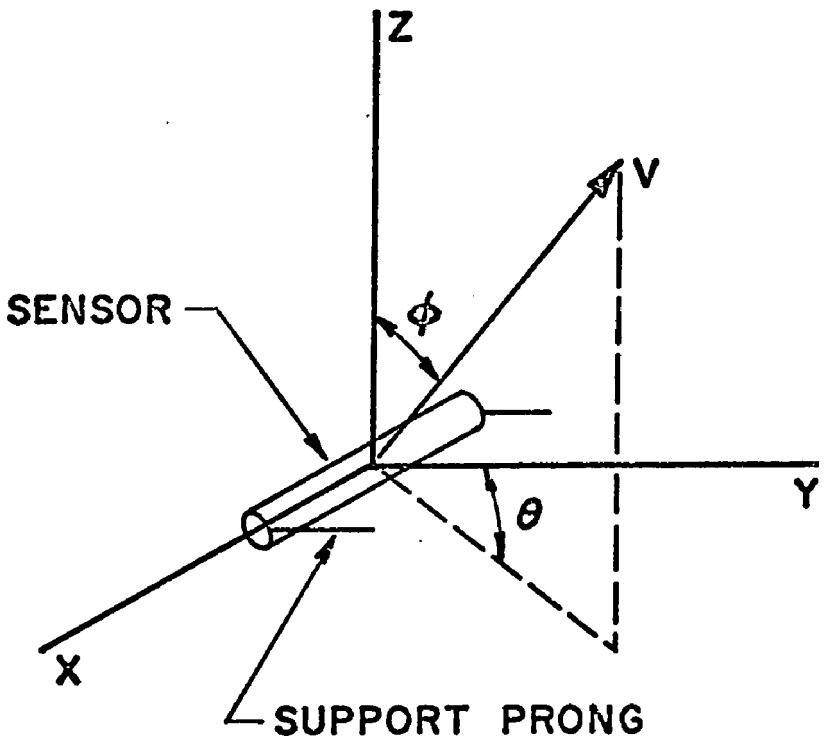

Figure 8 Coordinate system for probe calibration

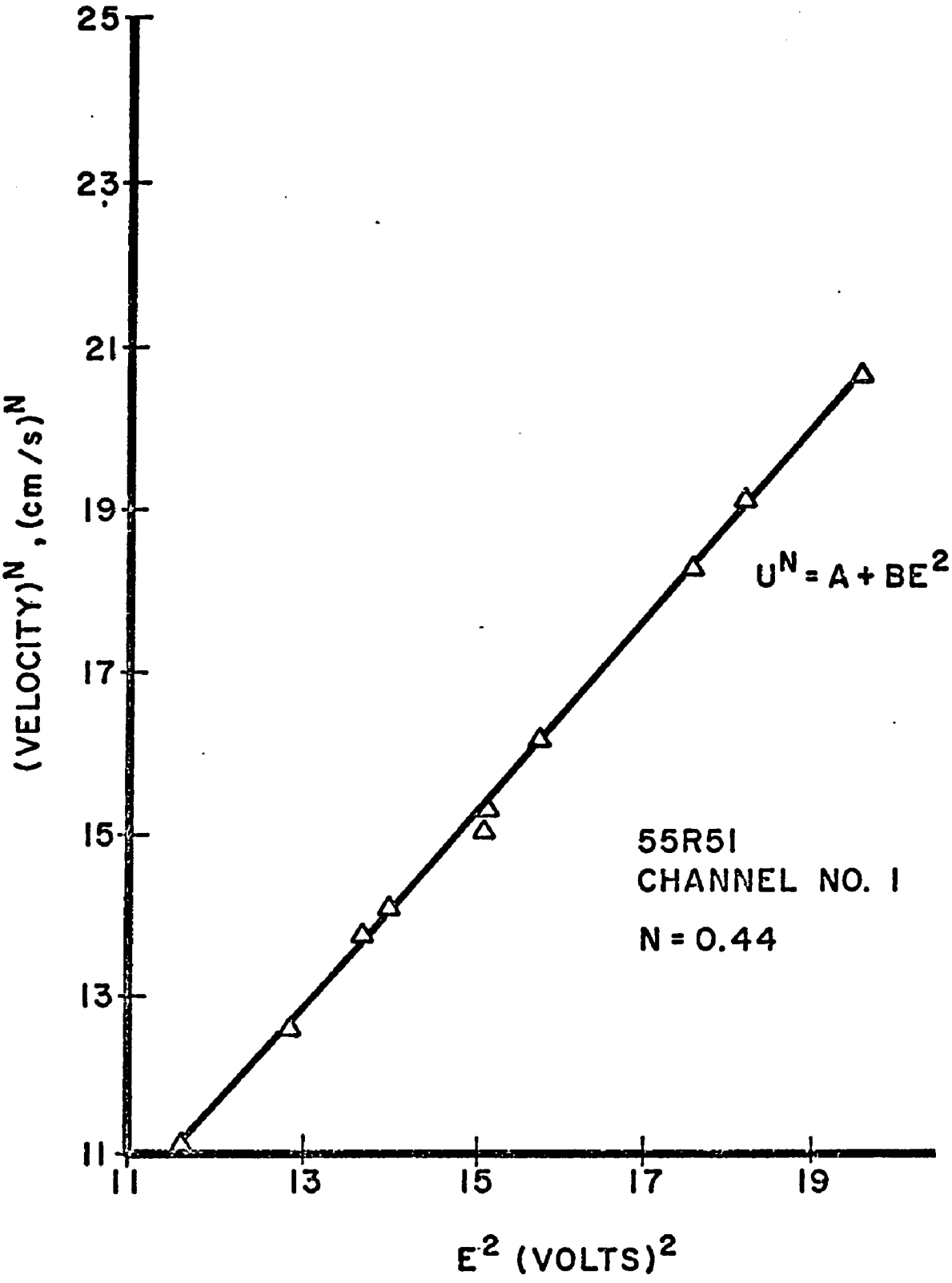

Figure 9 Calibration curve

Figure 10 Variation of K_1 with velocity

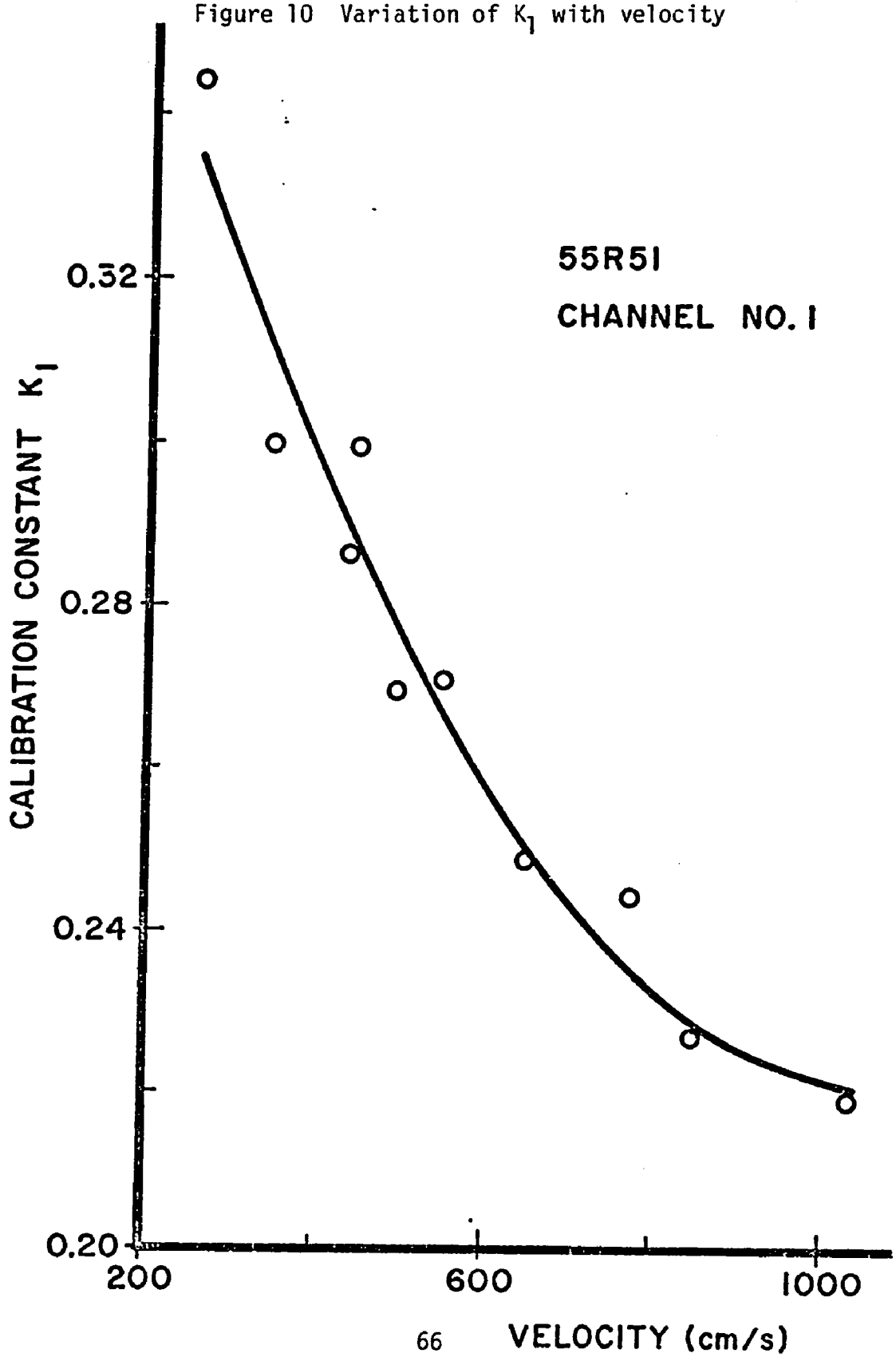

Figure 11 Variation of K_2 with velocity

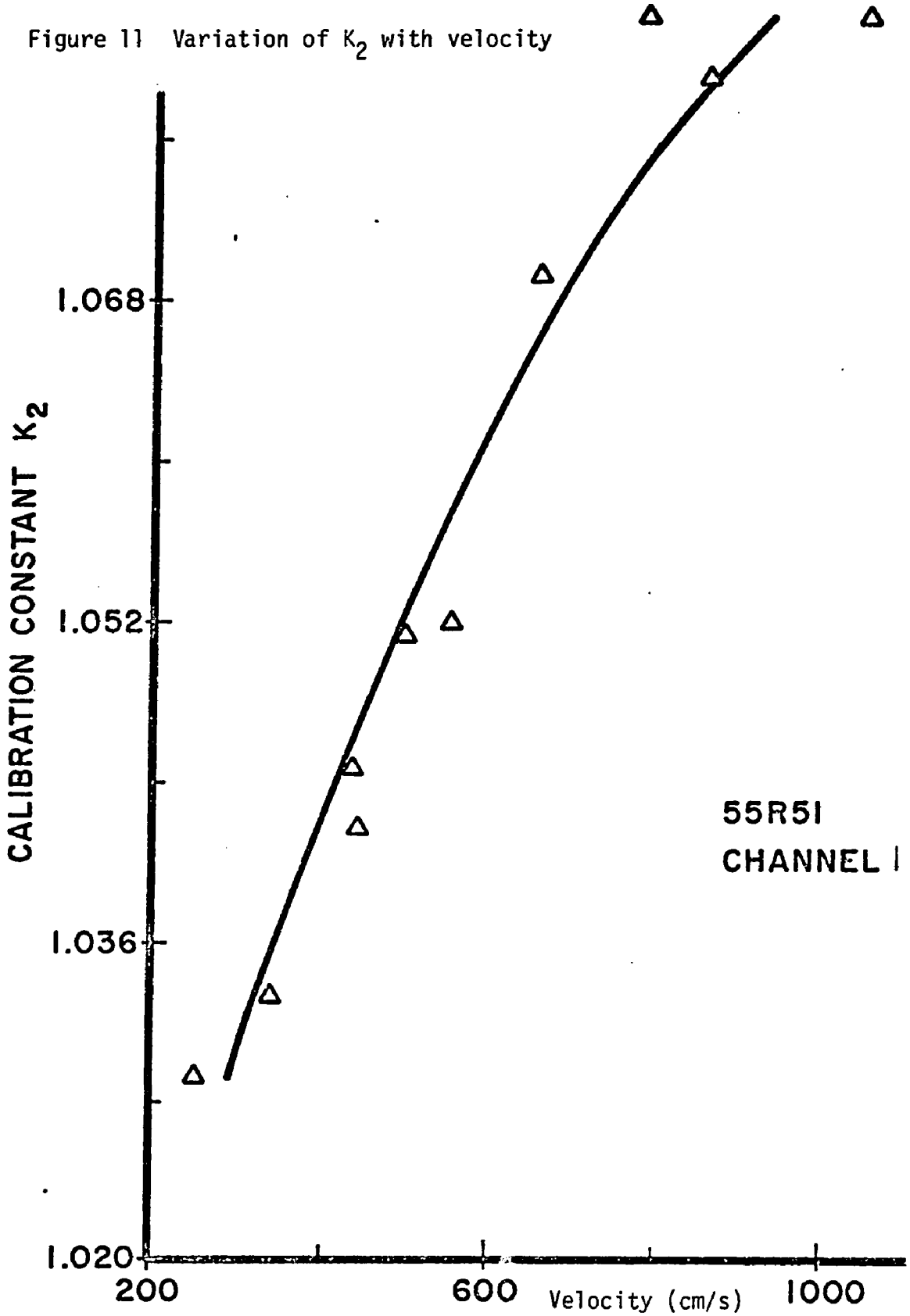

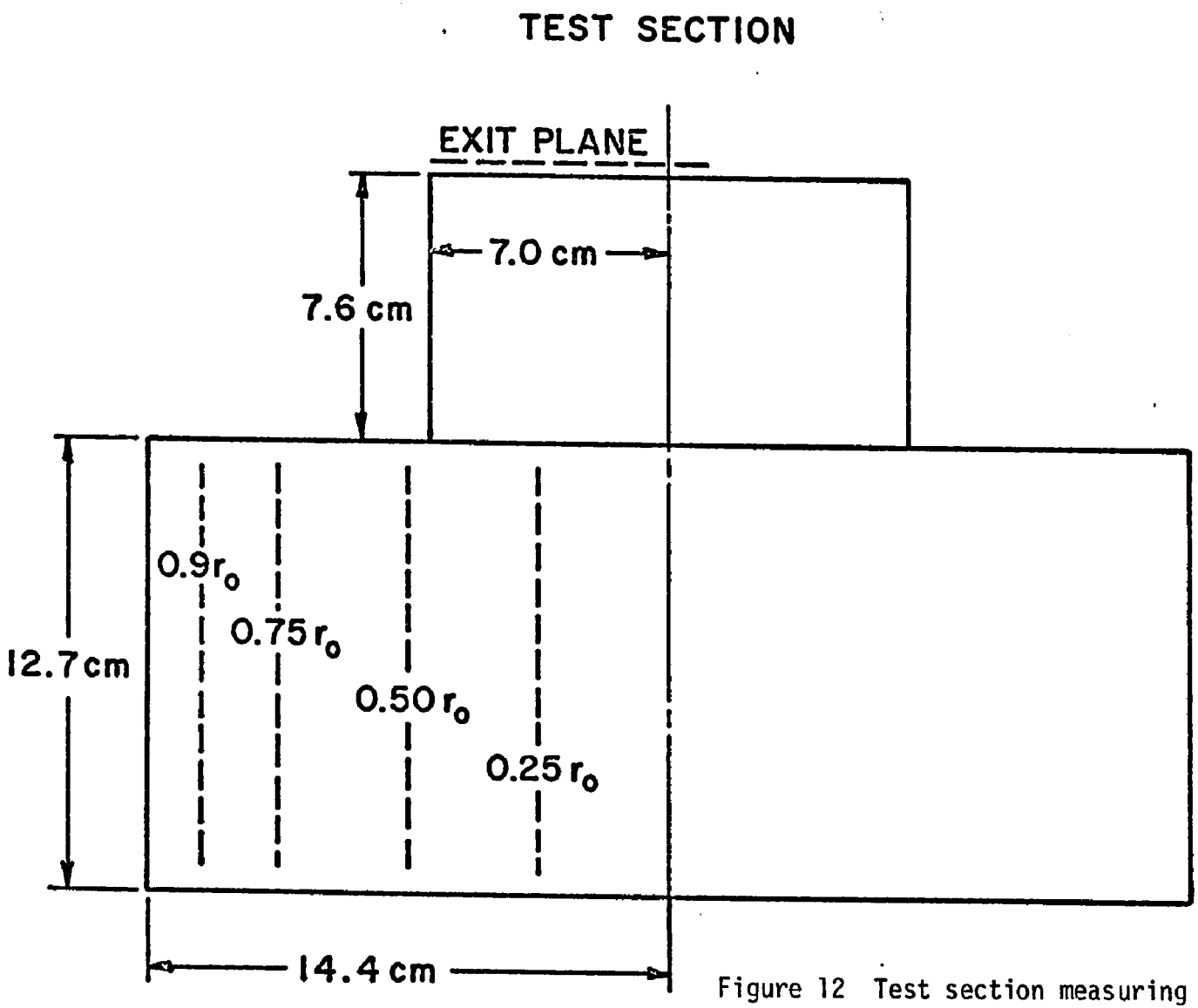

Figure 12 Test section measuring positions

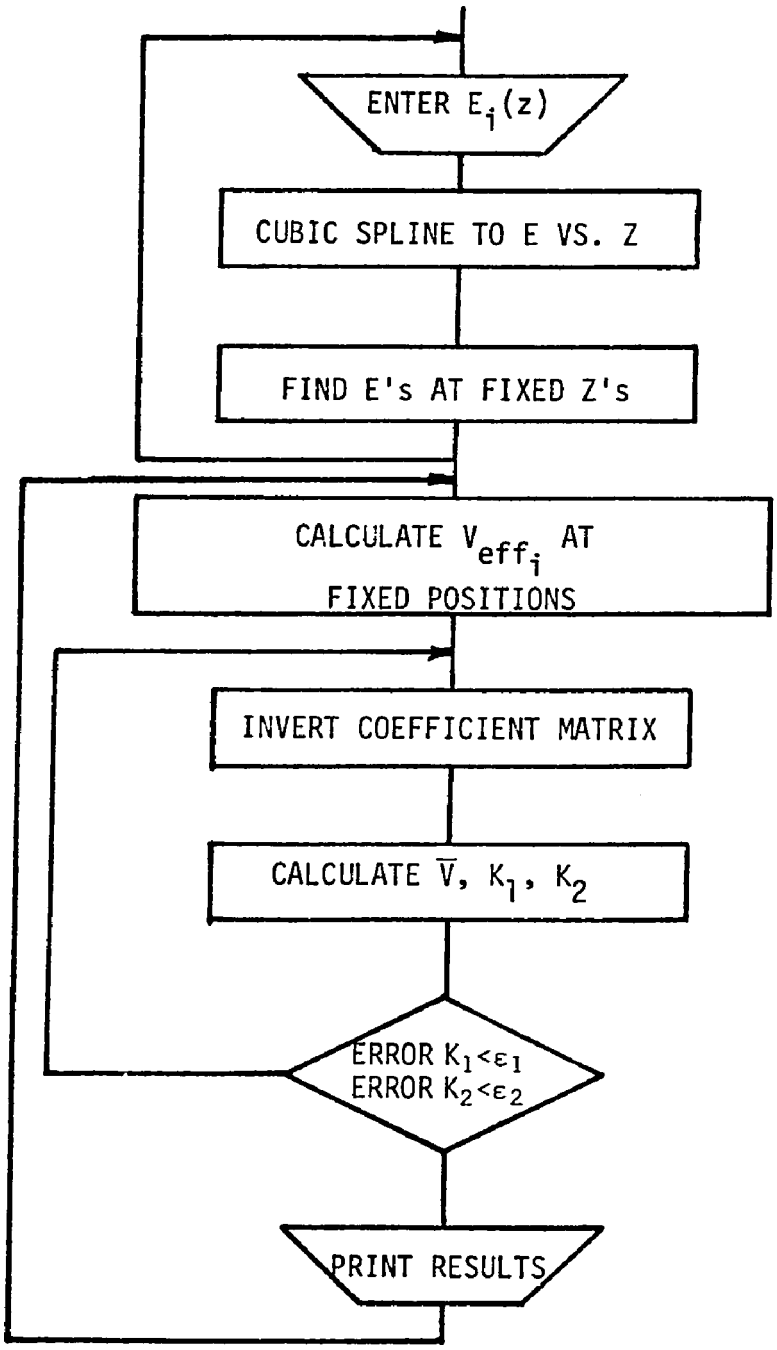

Figure 13 Data reduction flow chart

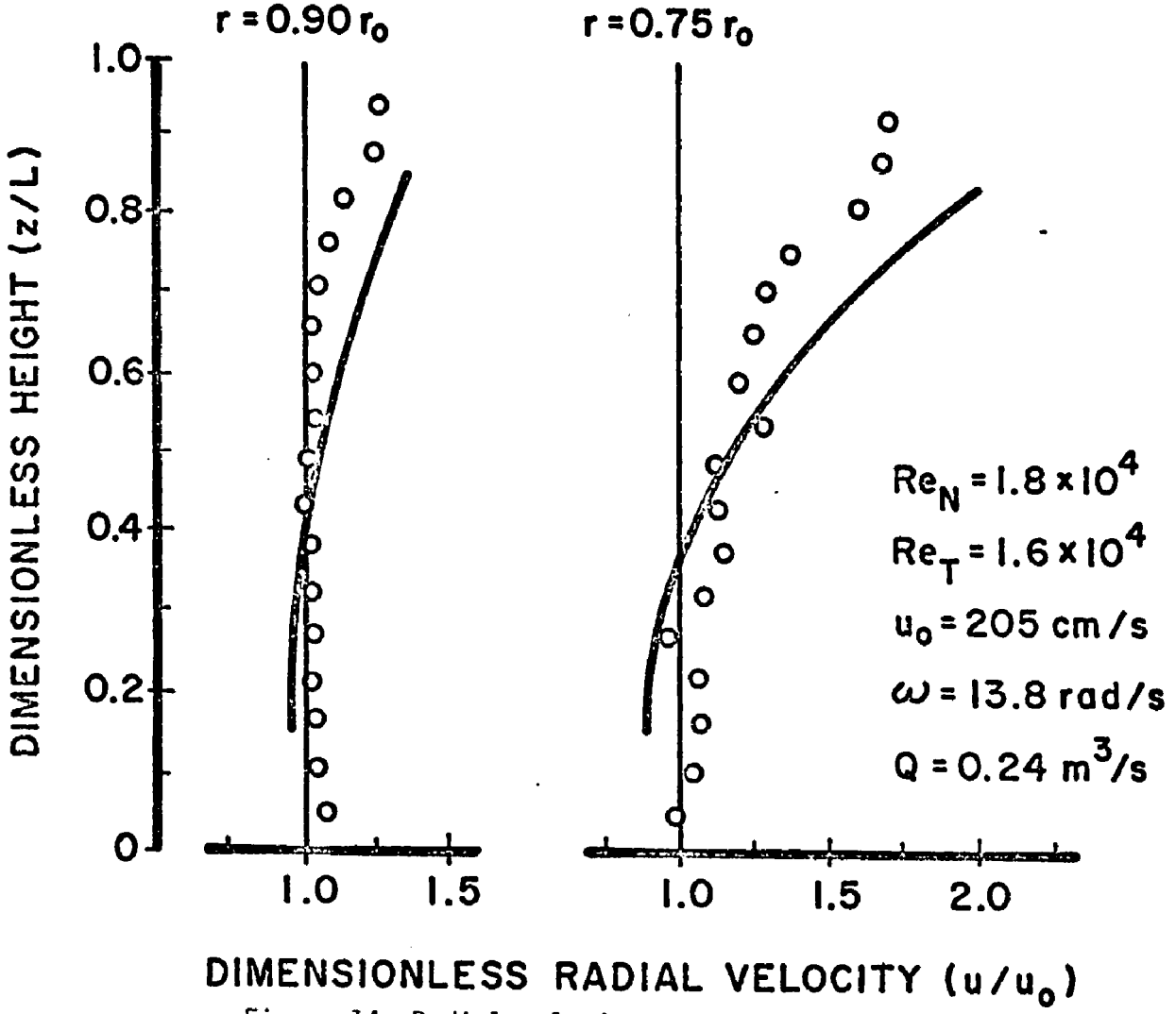

Figure 14a Radial velocity profiles $R_0/L = 1$

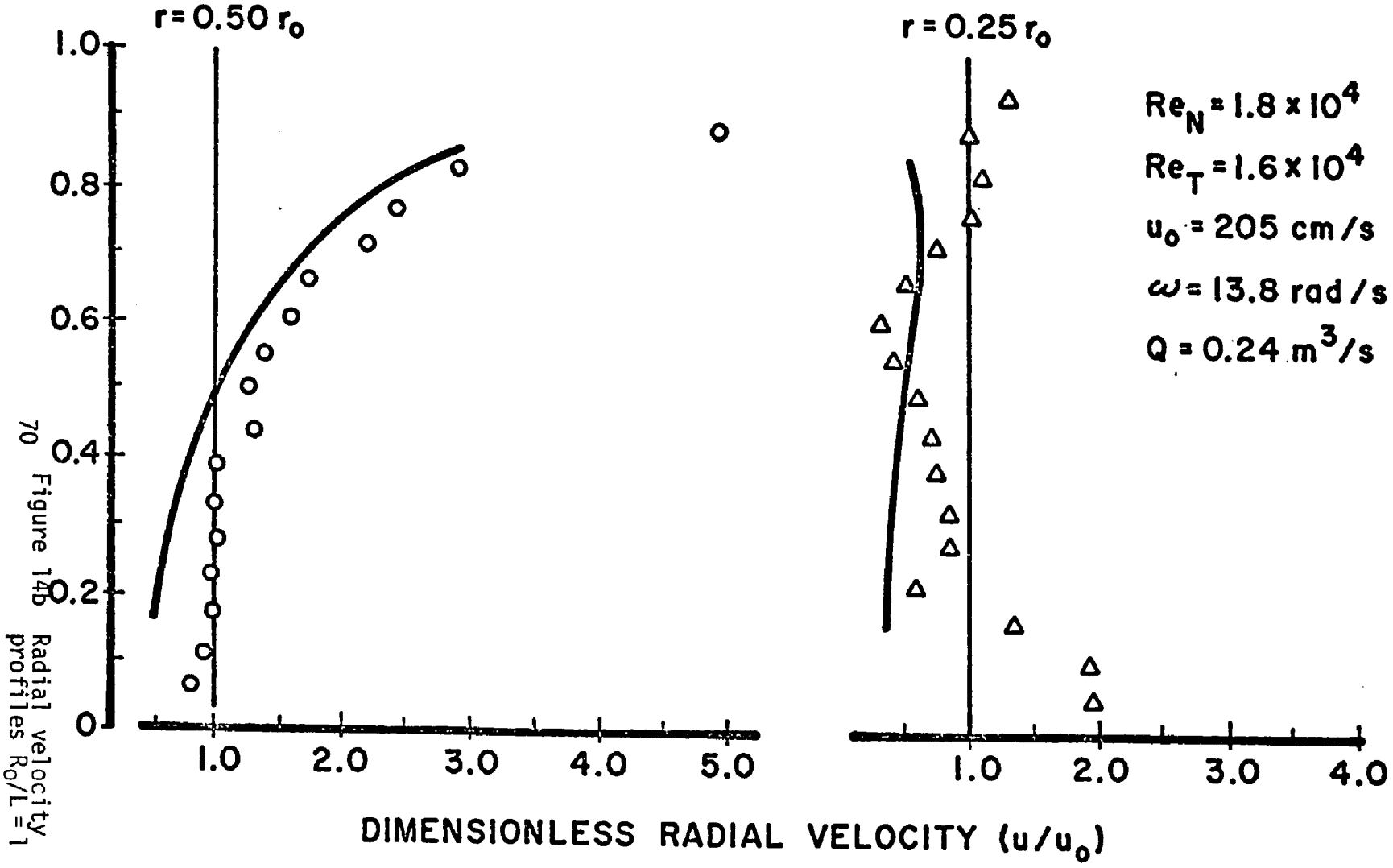

Figure 14b Radial velocity profiles $R_o/L = 1$

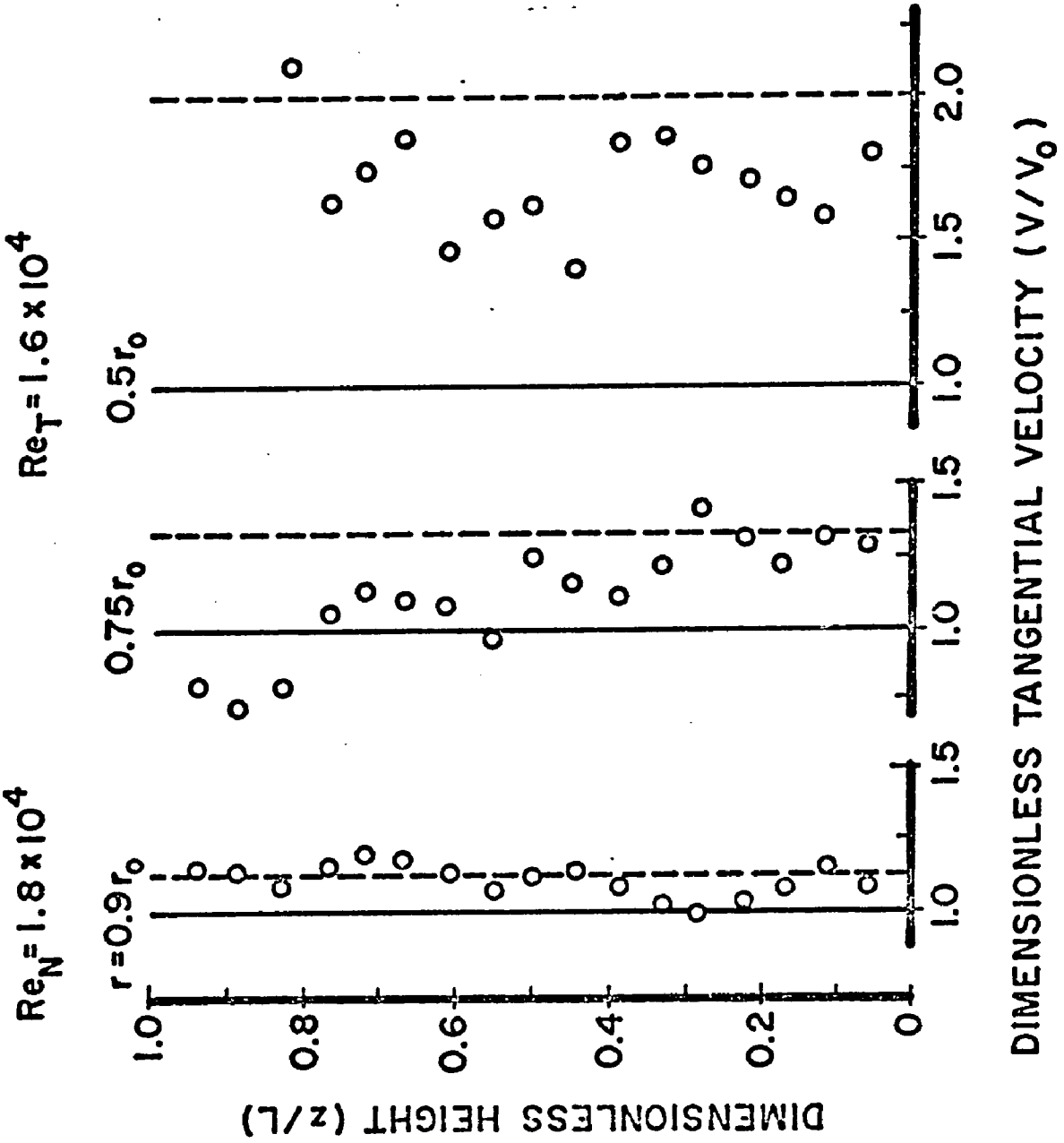

Figure 15 Tangential velocity profiles $R_o/L = 1$

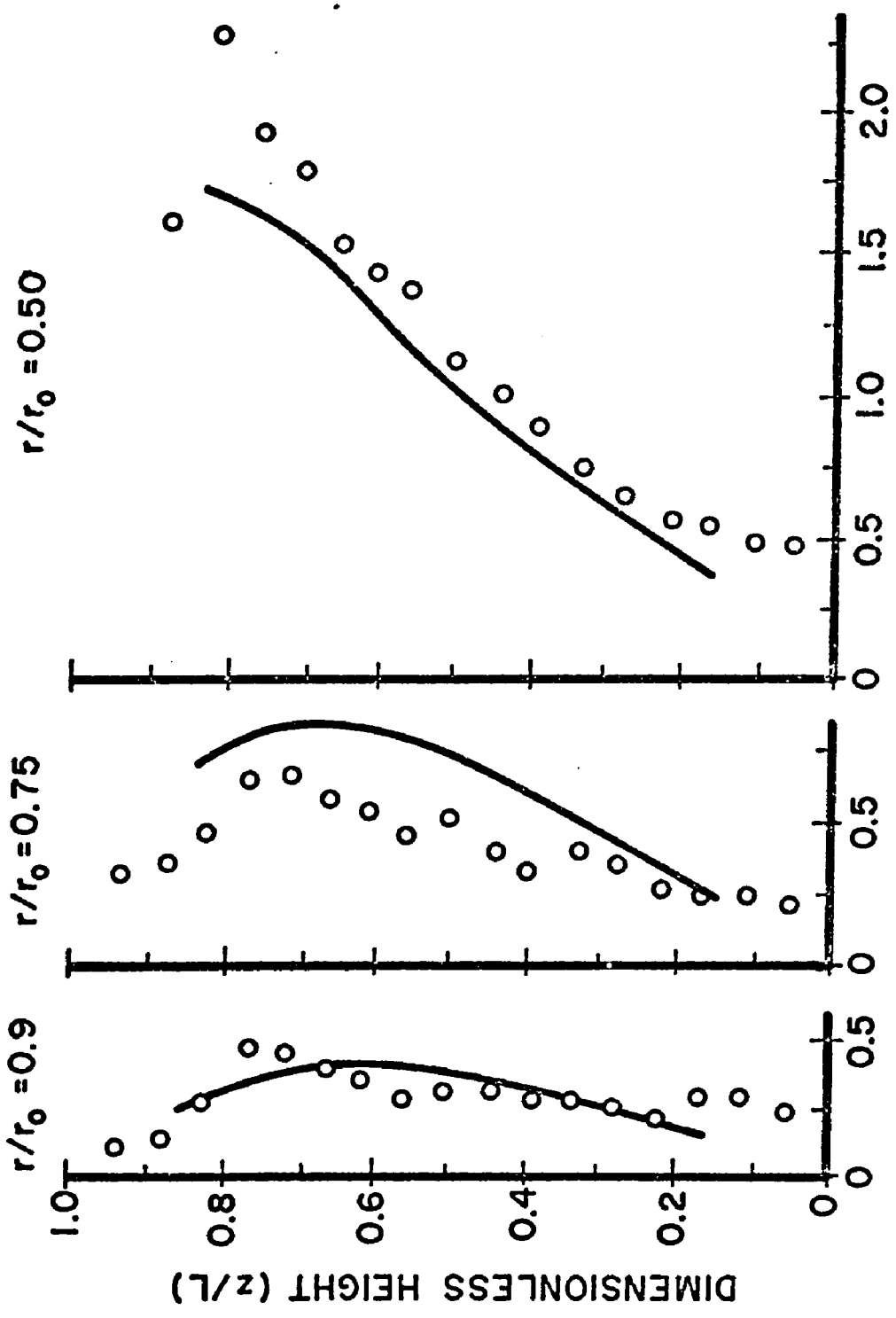

Figure 16 Axial velocity profiles $R_o/L = 1$

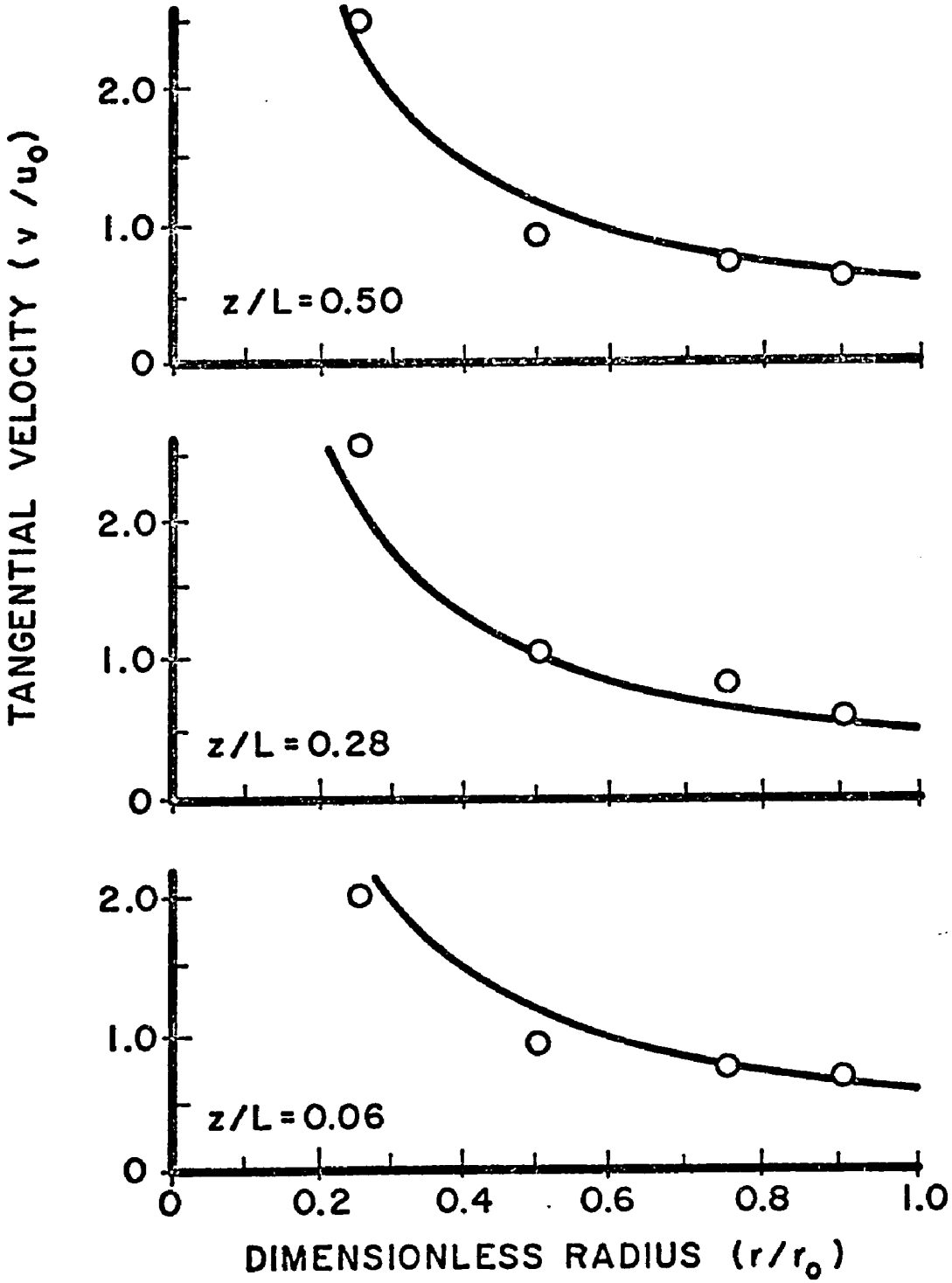

Figure 17 Radial variation of tangential velocity

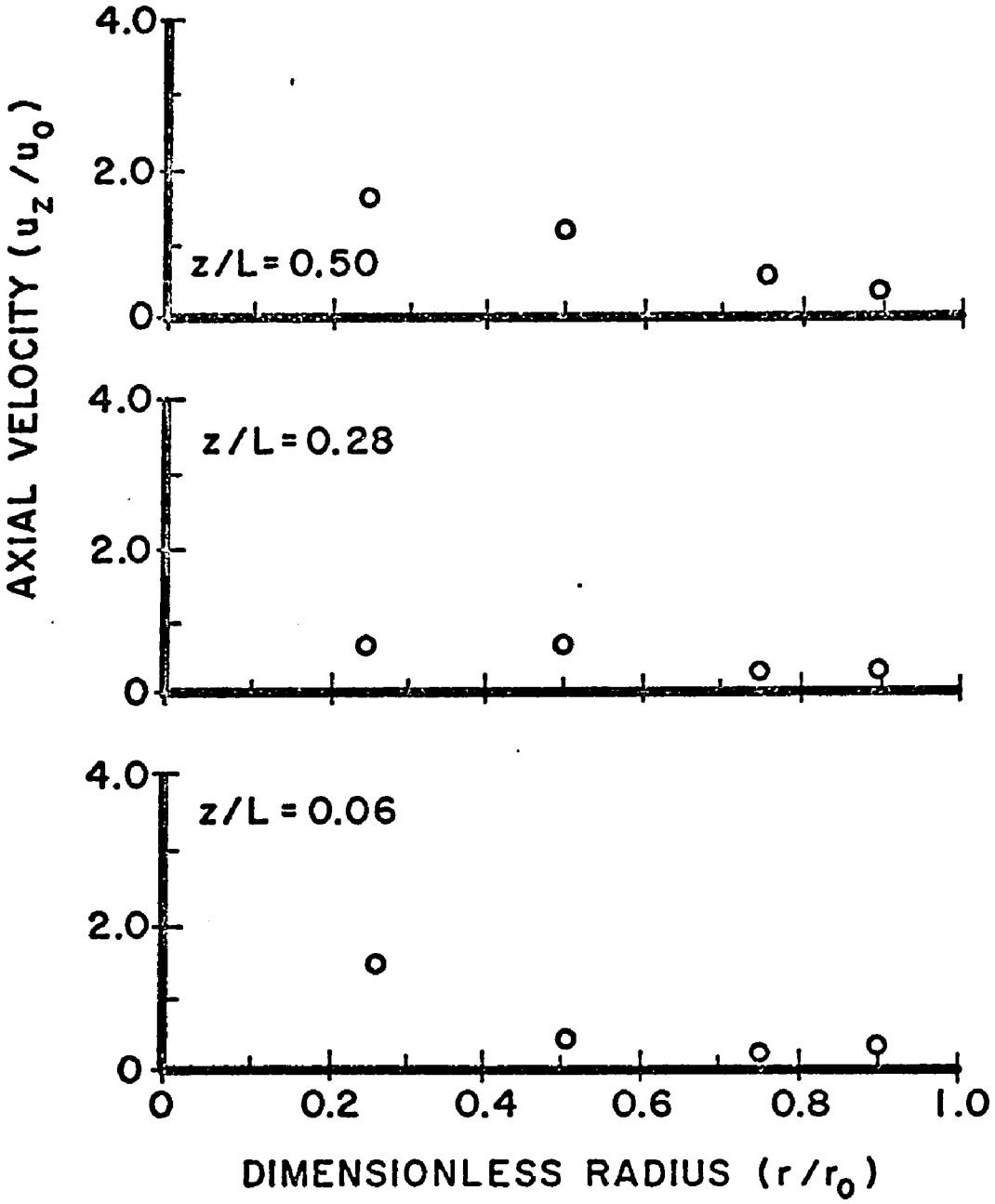

Figure 18 Radial variation of axial velocity

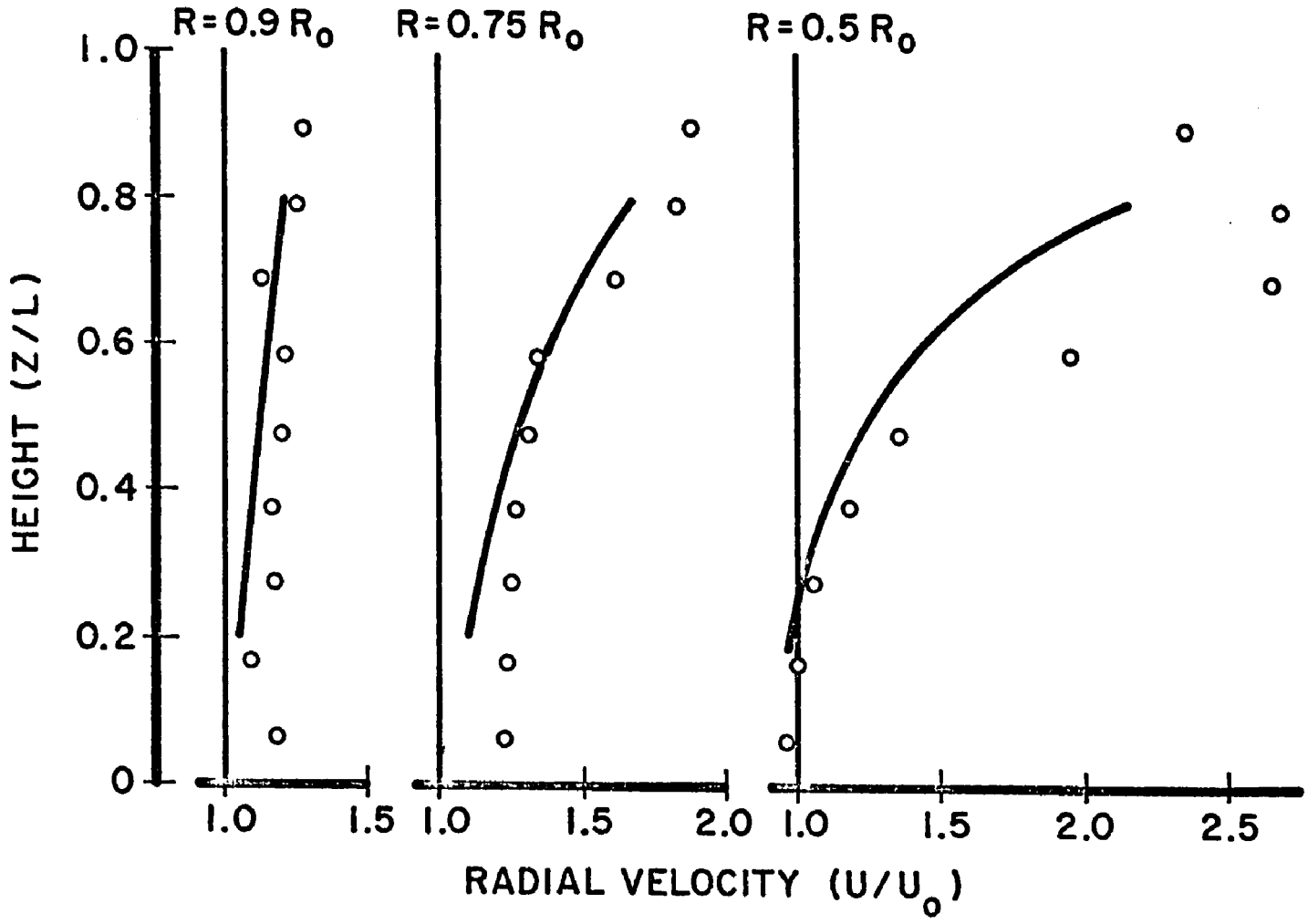

Figure 19 Radial velocity profiles $R_0/L = 2$

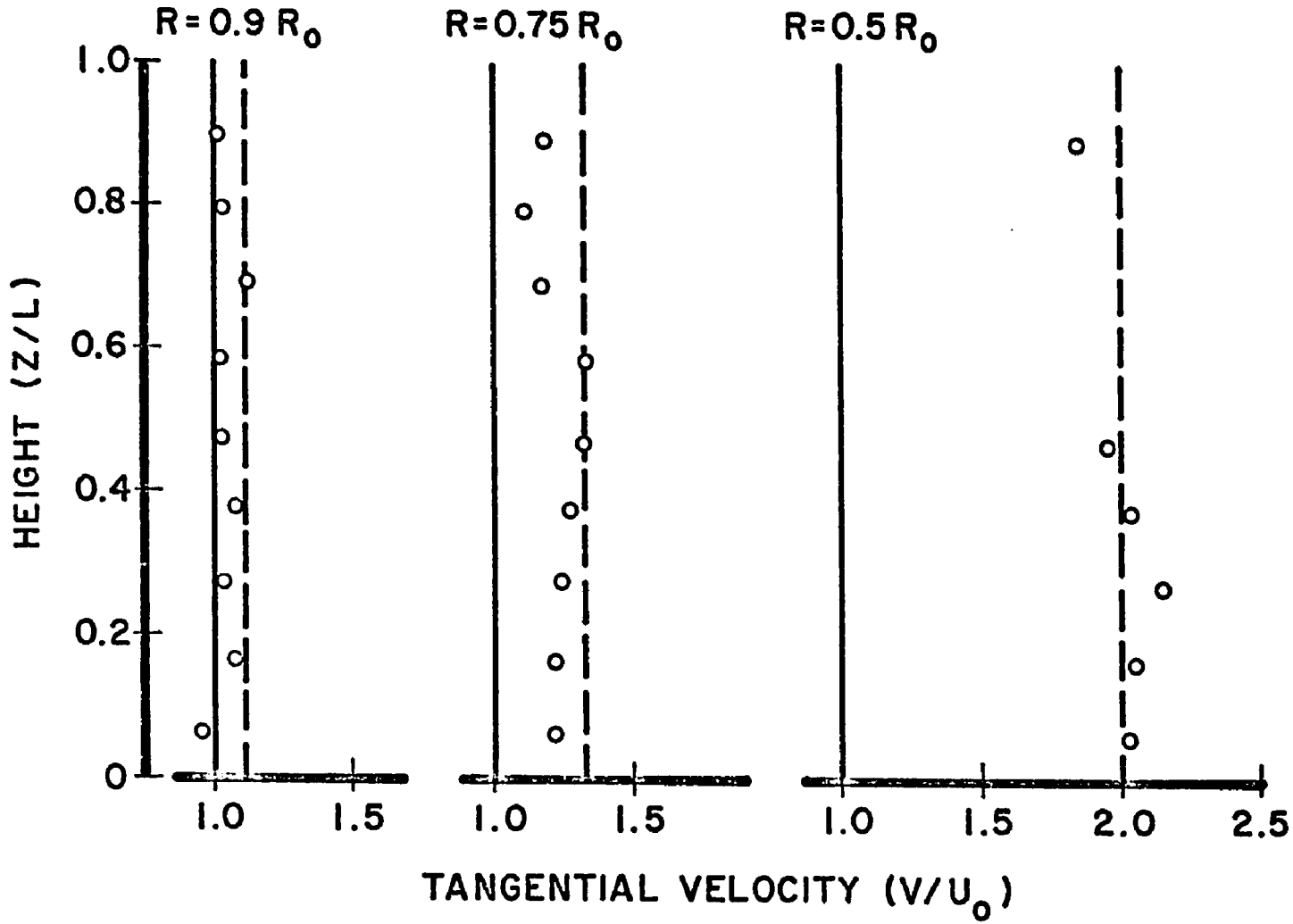

Figure 20 Tangential velocity profiles $R_0/L = 2$

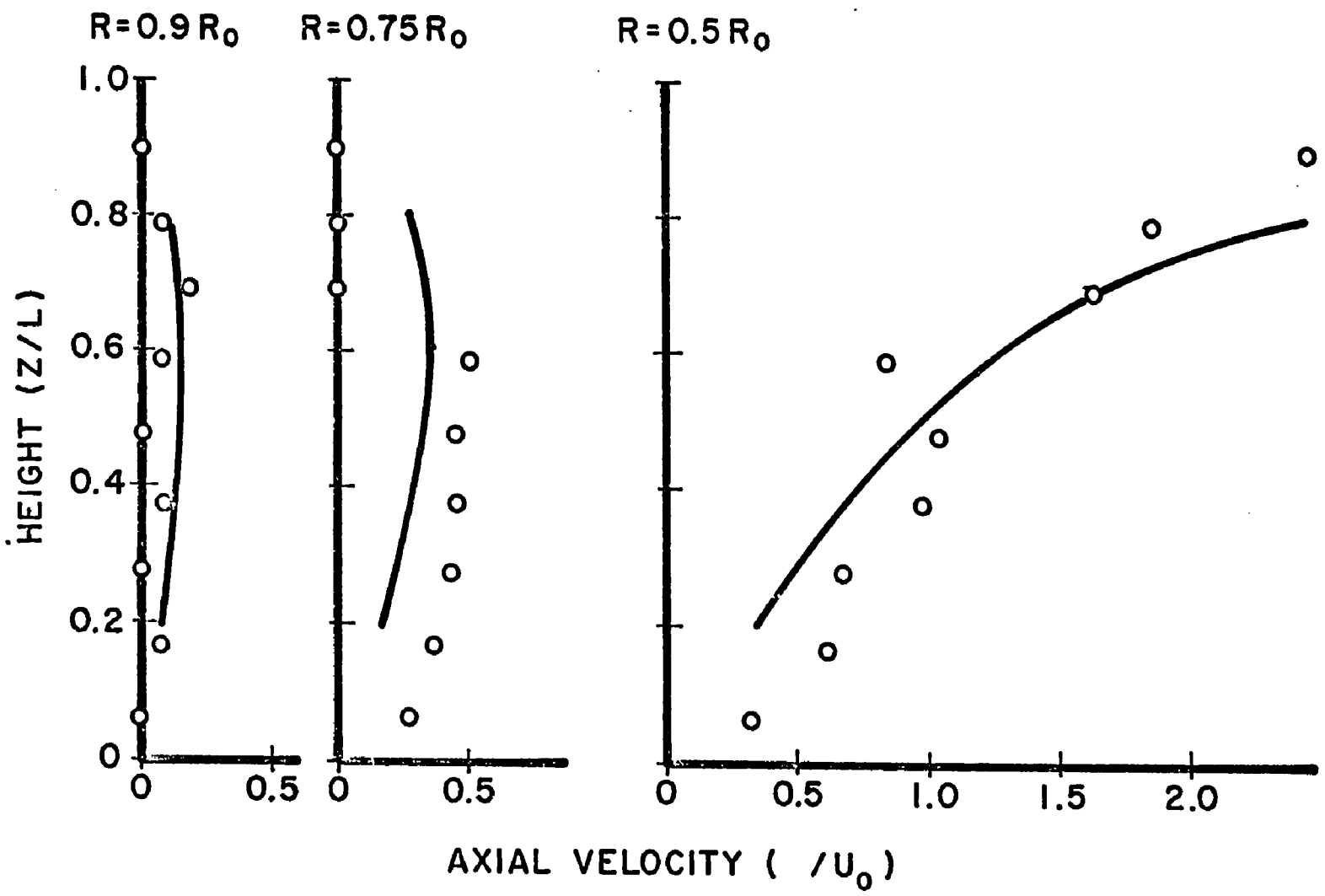

Figure 21 Axial velocity profiles $R_0/L = 2$

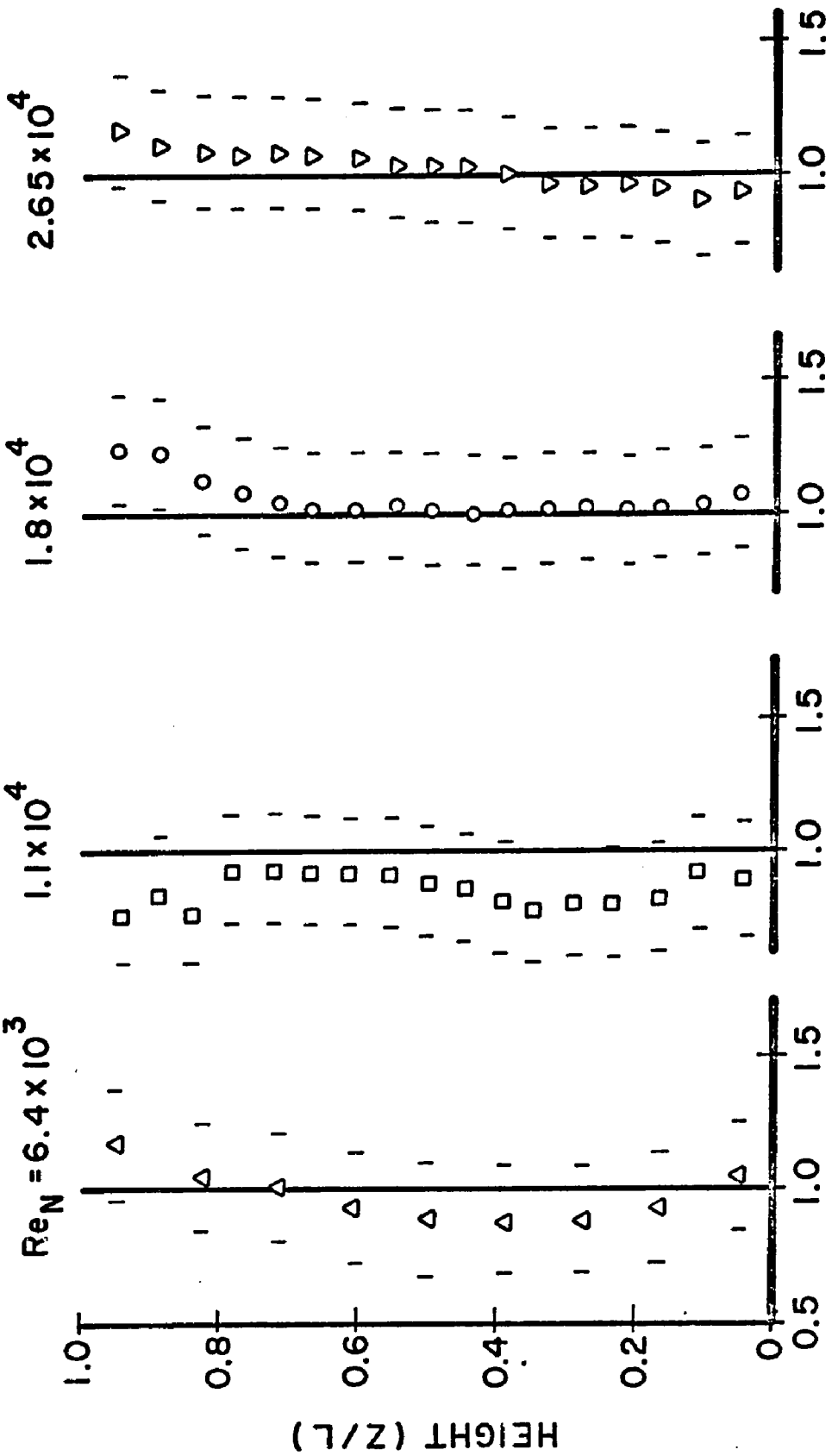

Figure 22a Effect of Re_N on radial velocity, $R = .9\ R_o$

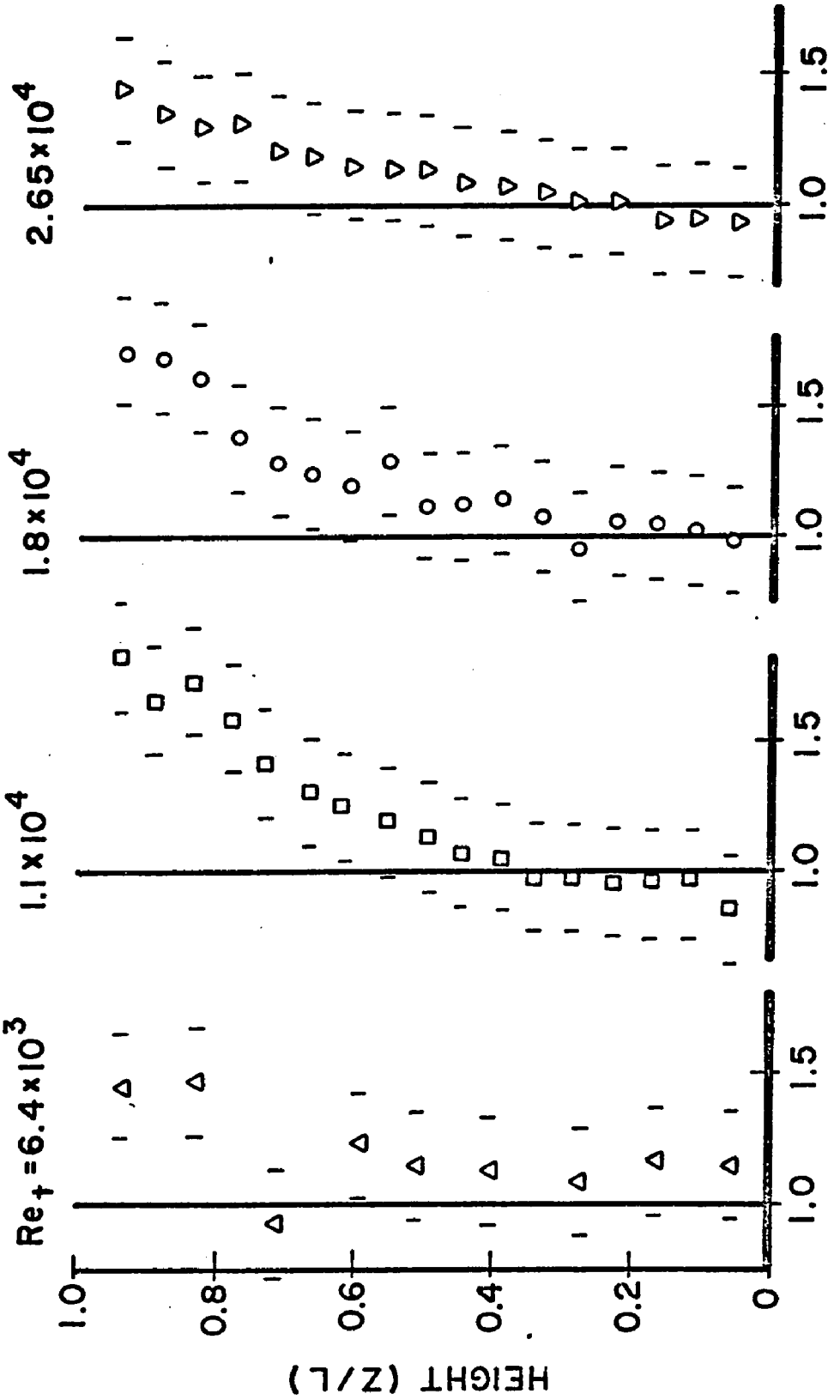

Figure 22b Effect of Re_N on radial velocity, R = .75 R_o

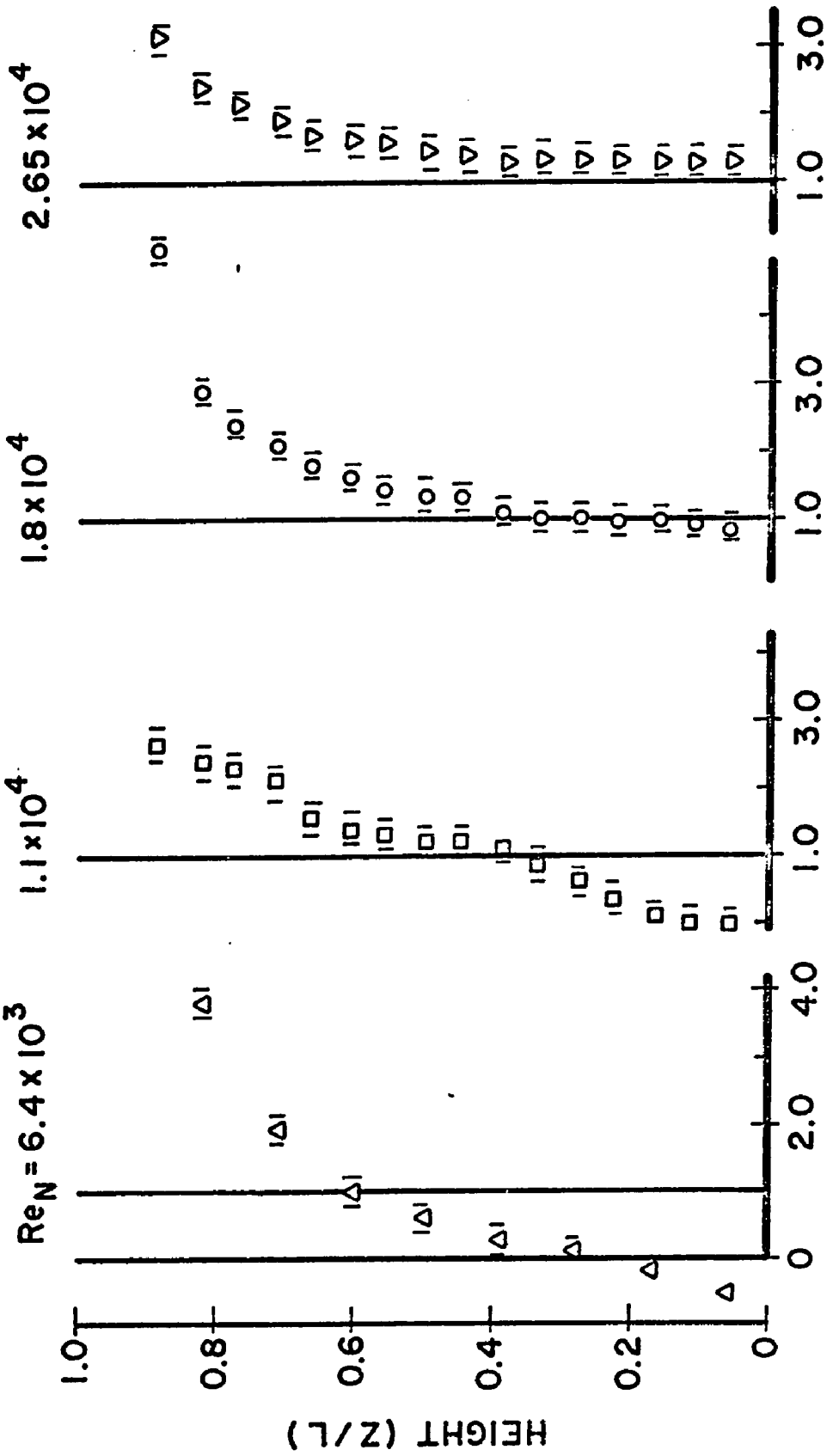

Figure 22c Effect of Re_N on radial velocity, R = .50 R_0

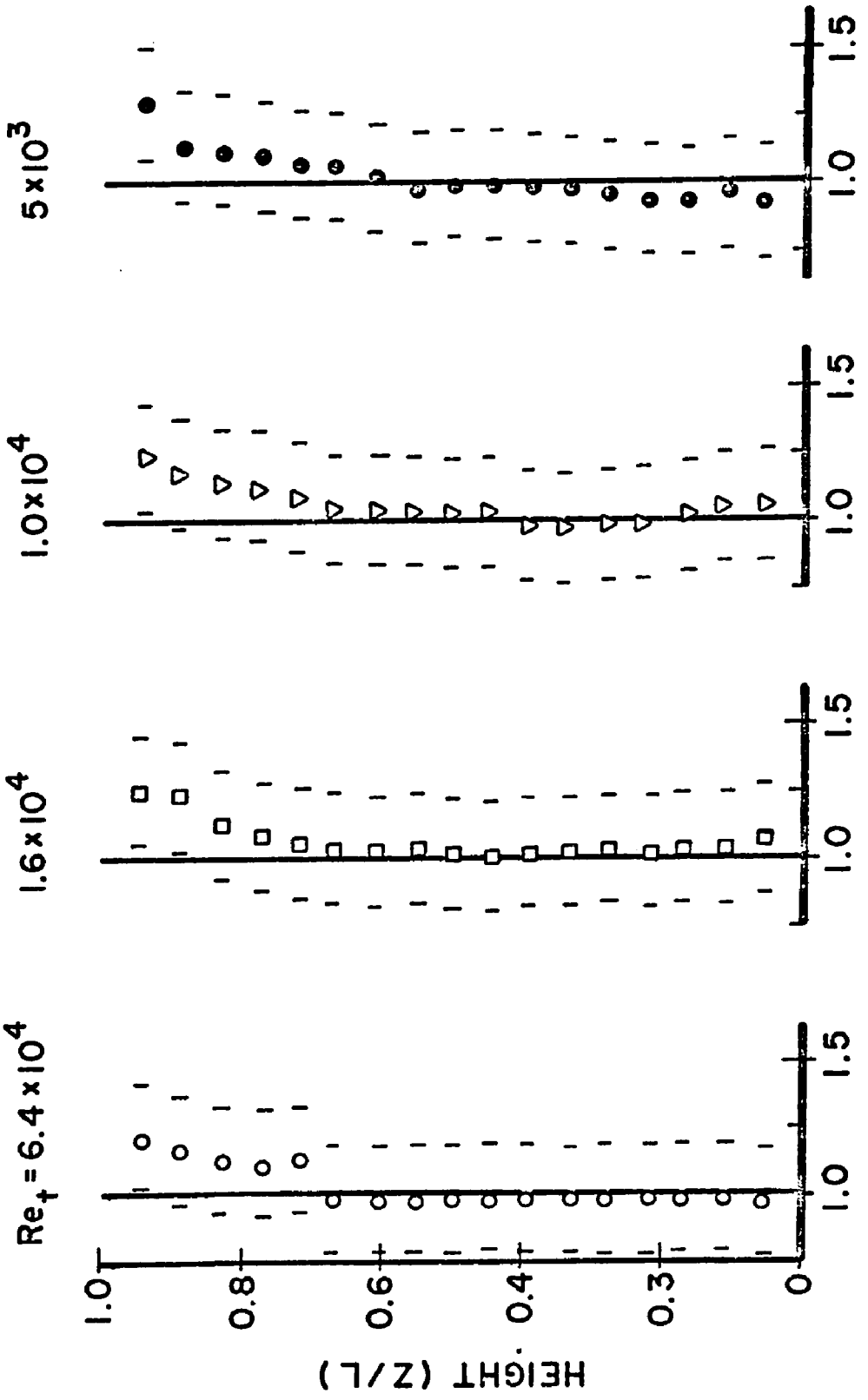

Figure 23a Effect of Re_t on radial velocity, R = .90 R_o

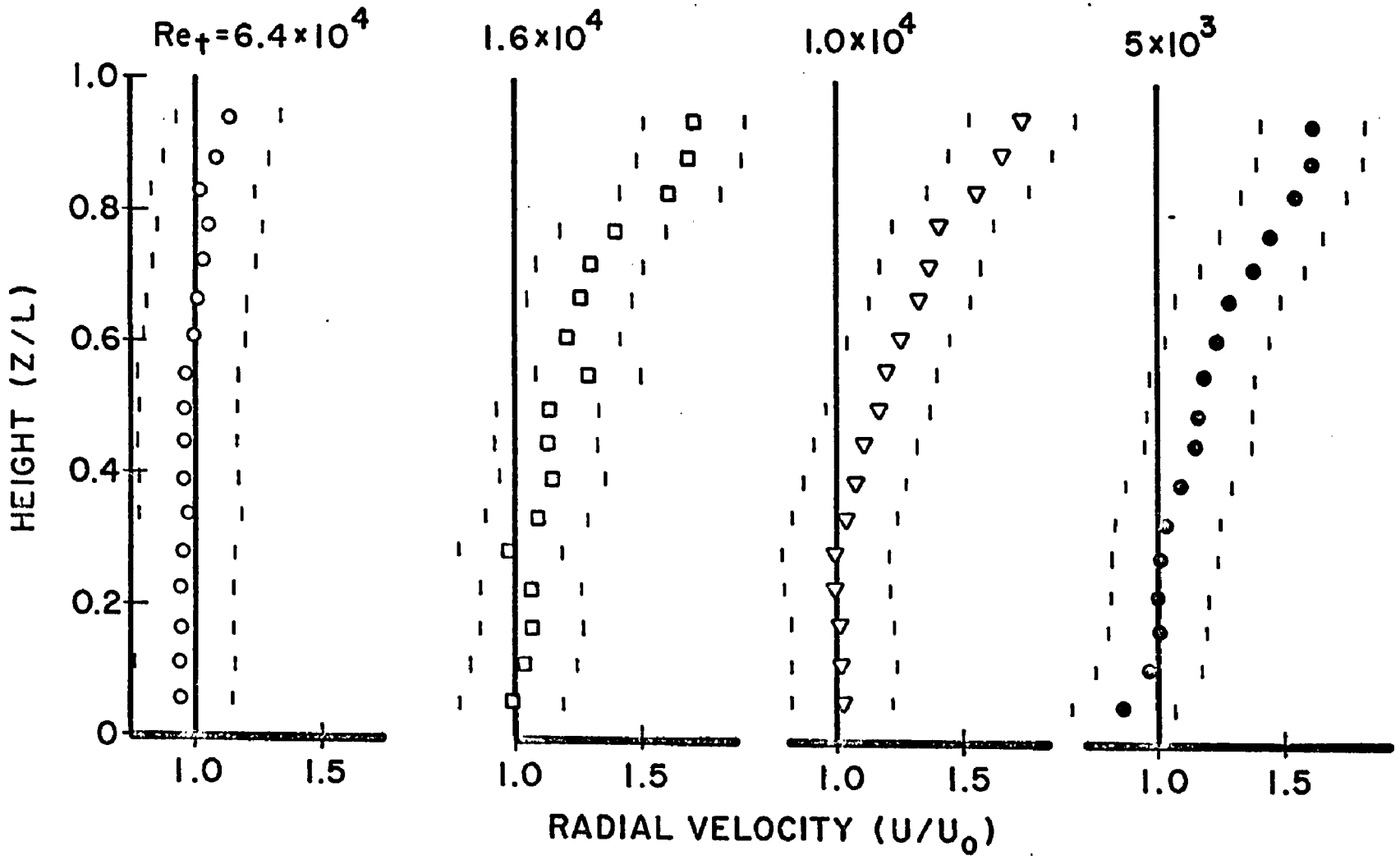

Figure 23b Effect of Re_t on radial velocity, R = .75 R_0

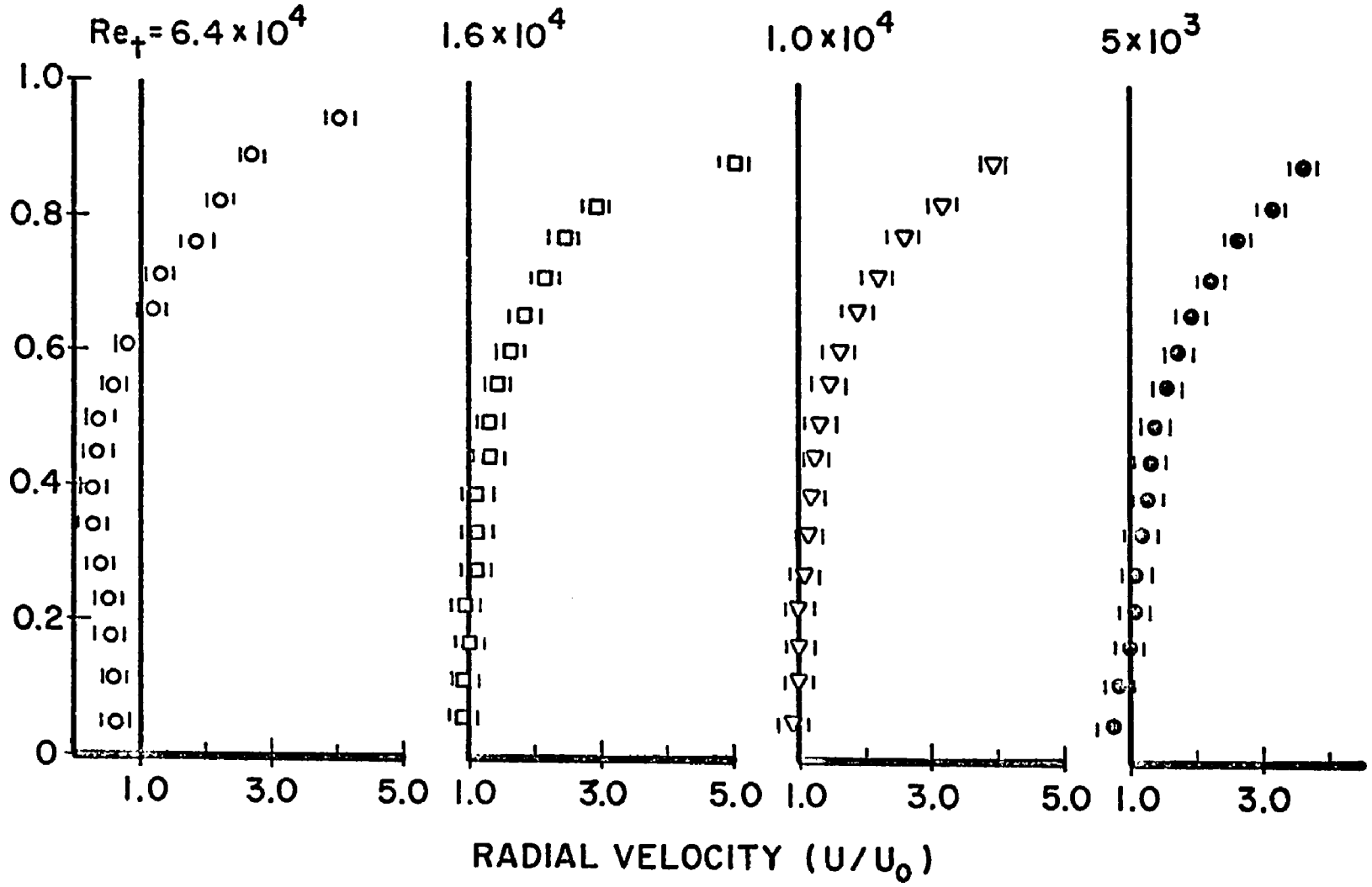

Figure 23c Effect of Re_t on radial velocity, R = .50 R_0

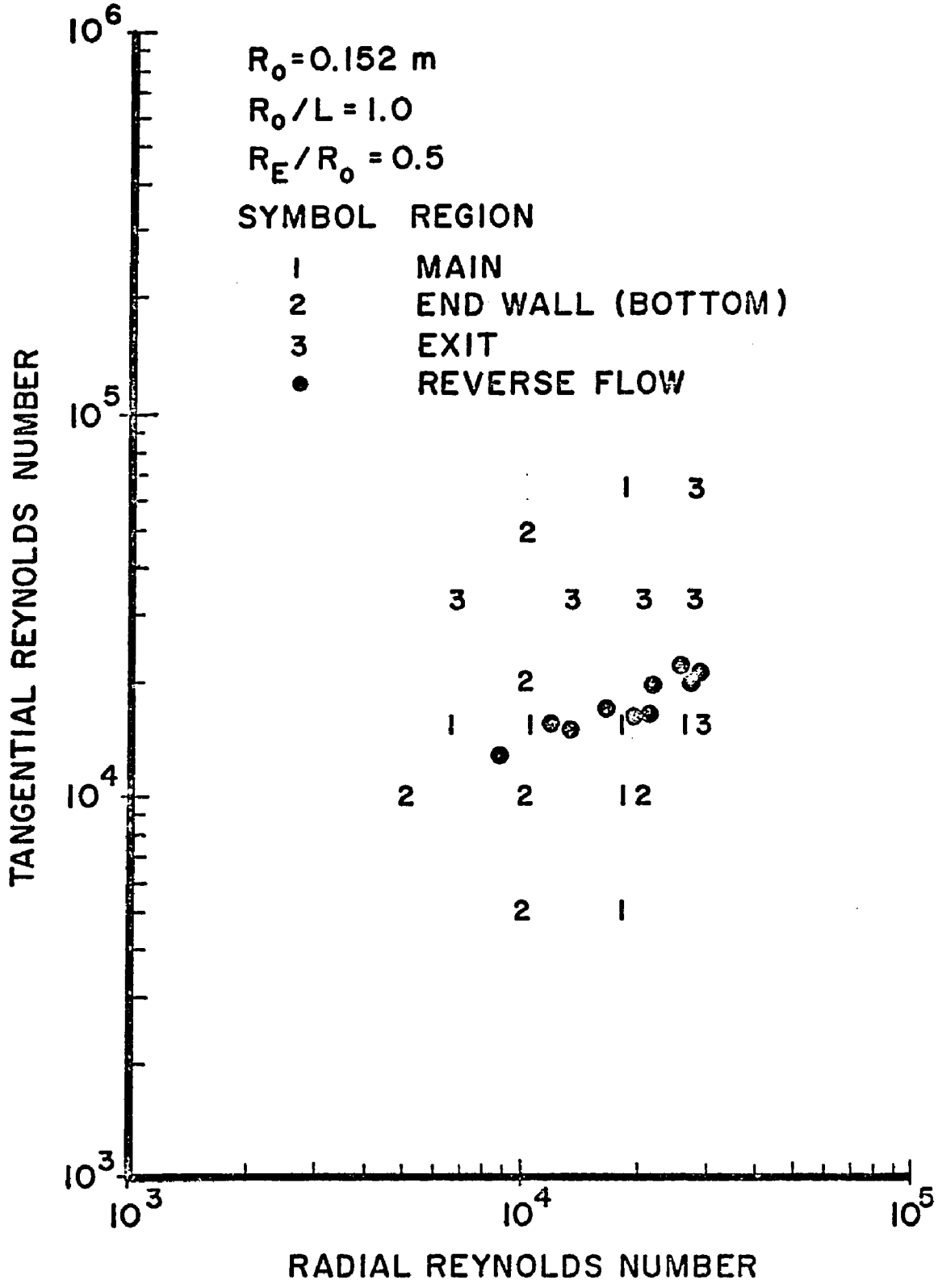

Figure 24 Chamber data map

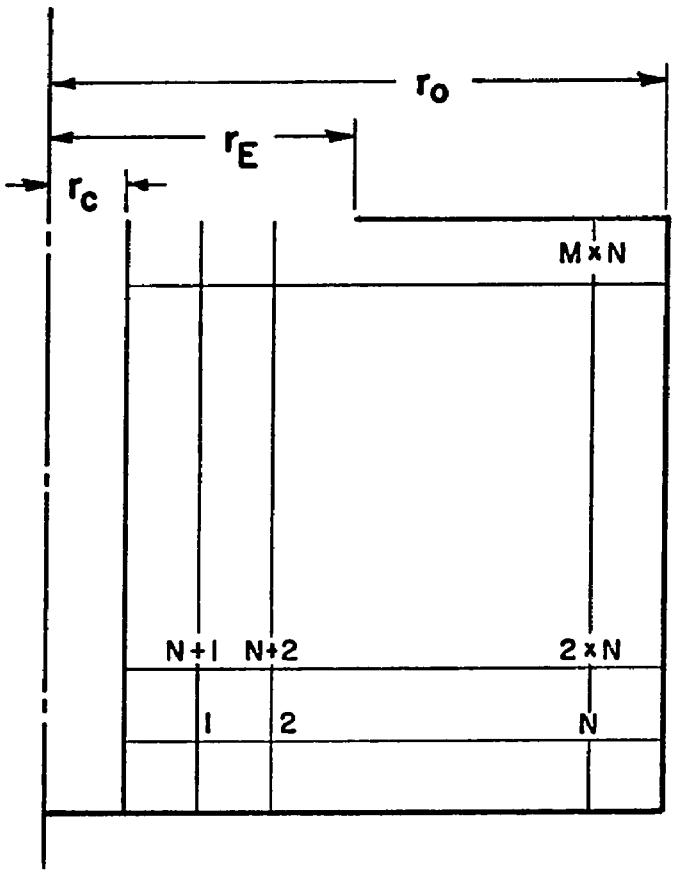

Figure 25 Finite difference grid for potential flow calculation

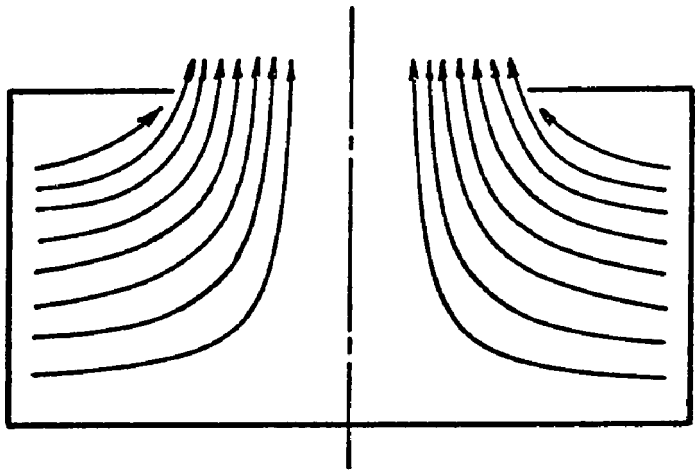

Figure 26 Streamlines in the r-z plane

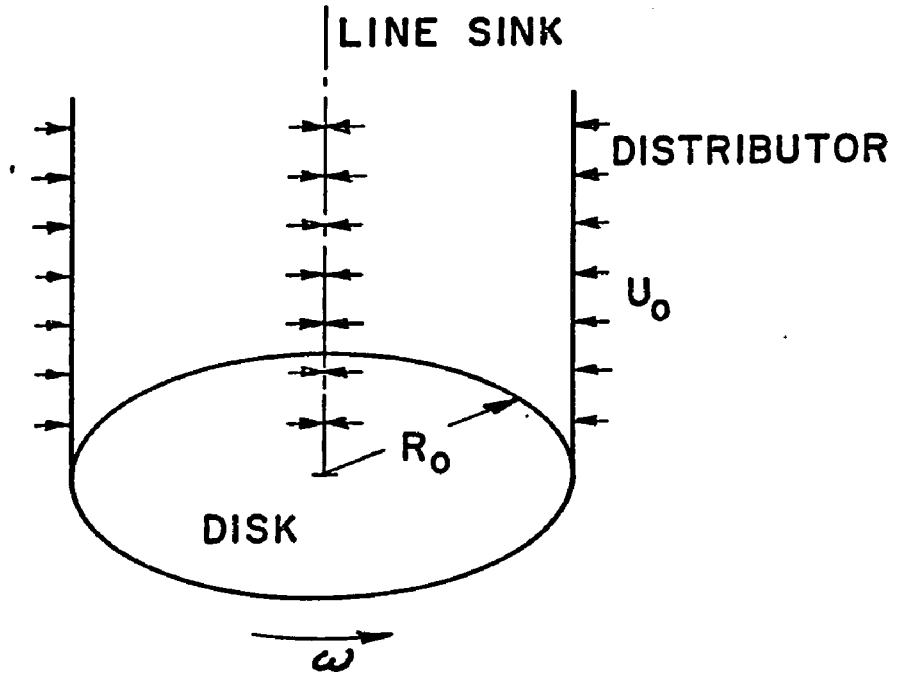

Figure 27 Idealized boundary layer problem

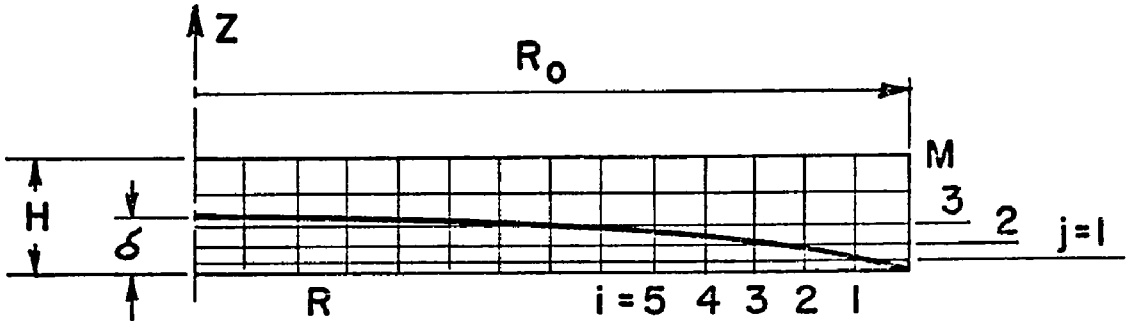

Figure 28 Finite difference grid for boundary layer

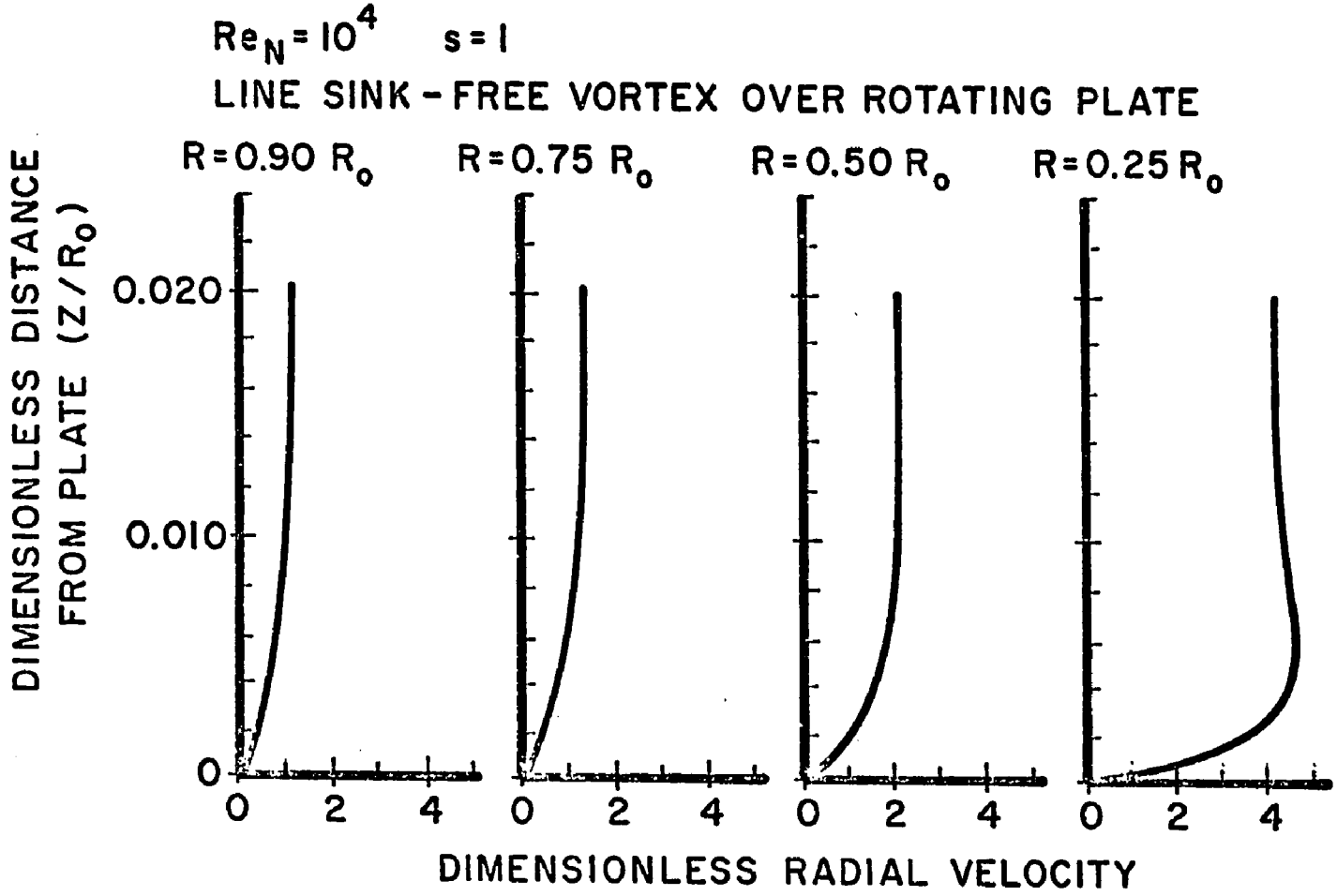

Figure 29 Radial boundary layer development-idealized flow

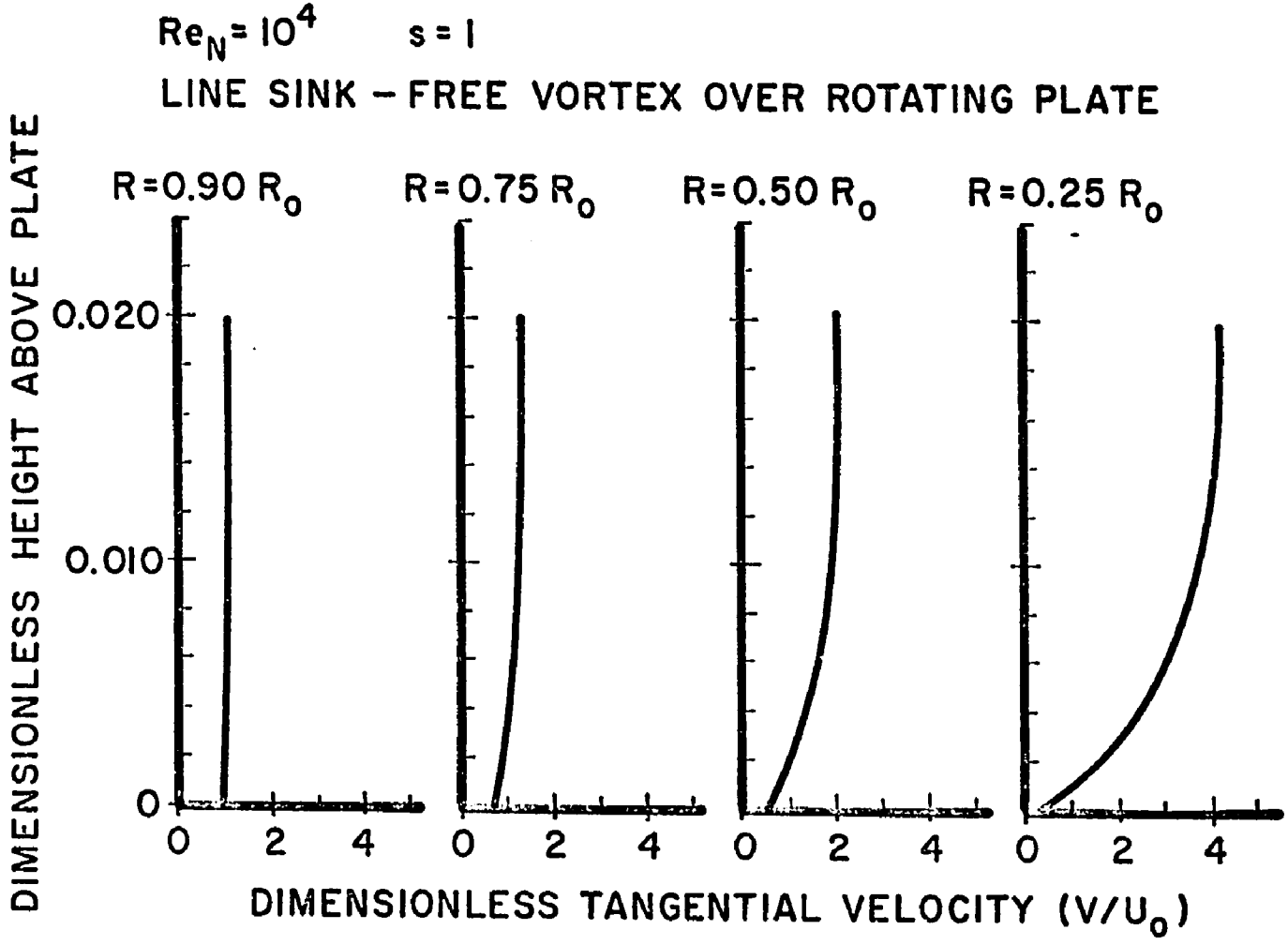

Figure 30 Tangential boundary layer development-idealized flow

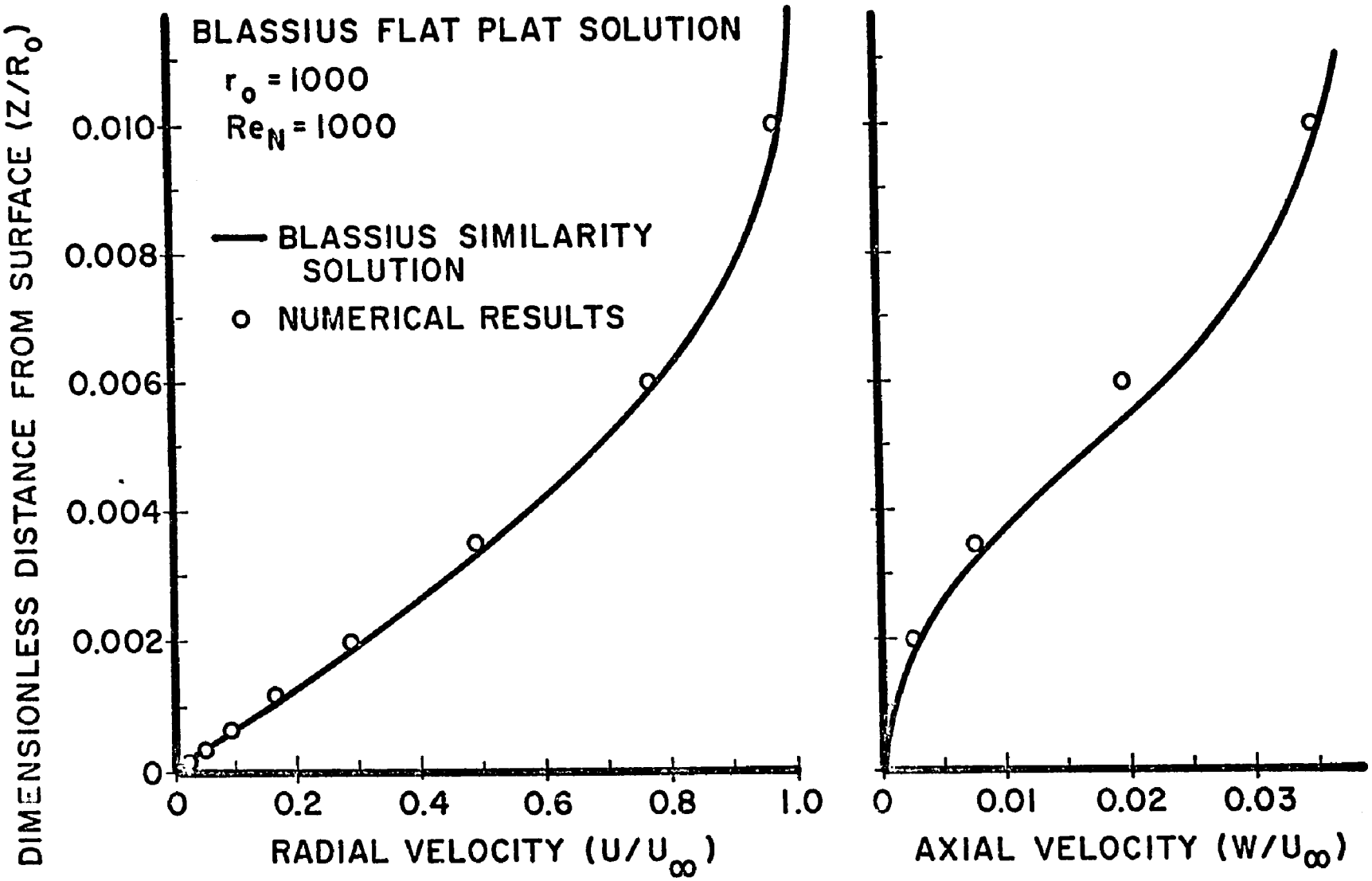

Figure 31 Comparison of numerical and Blassius solutions

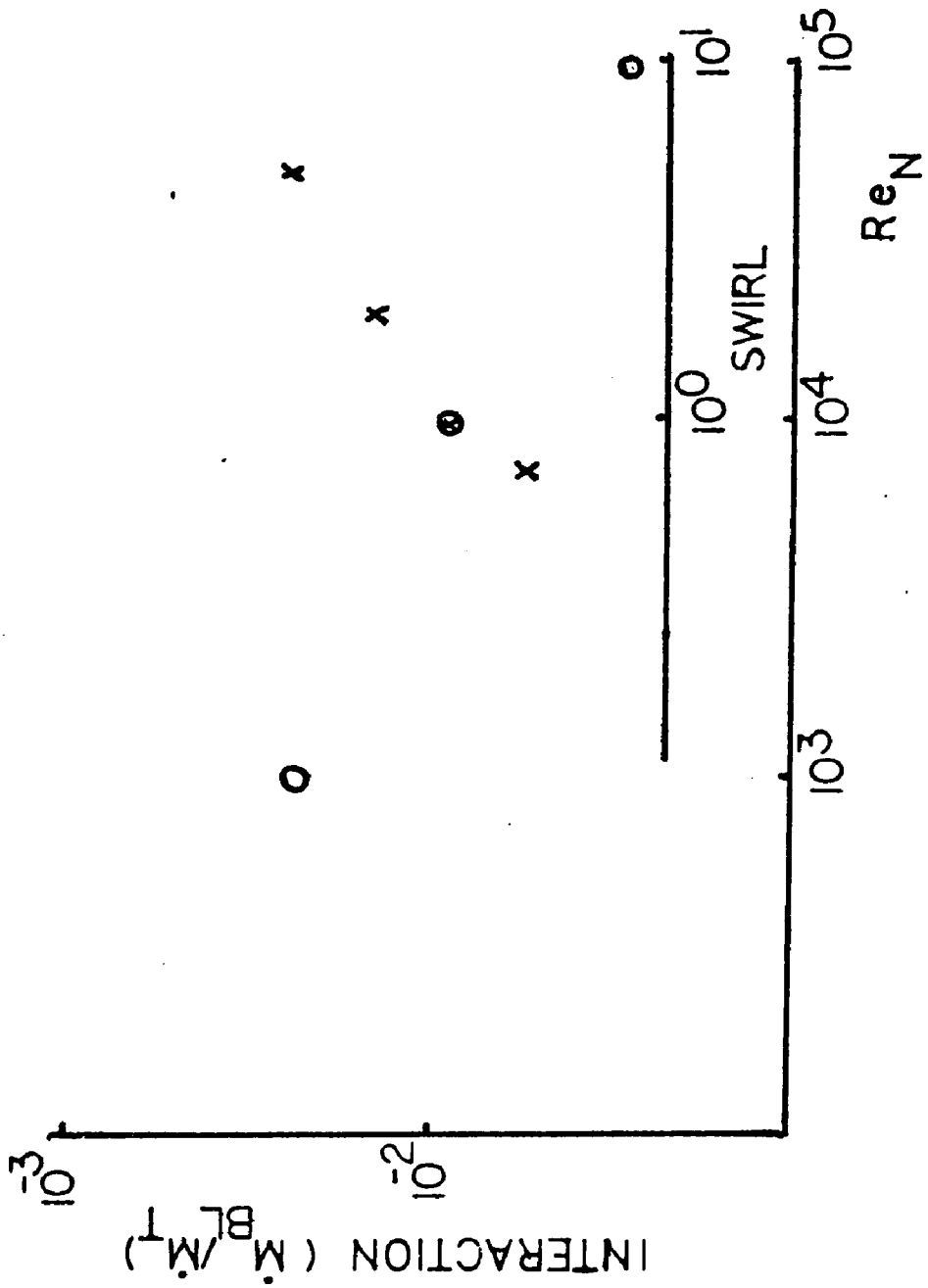

Figure 32 Boundary layer interaction

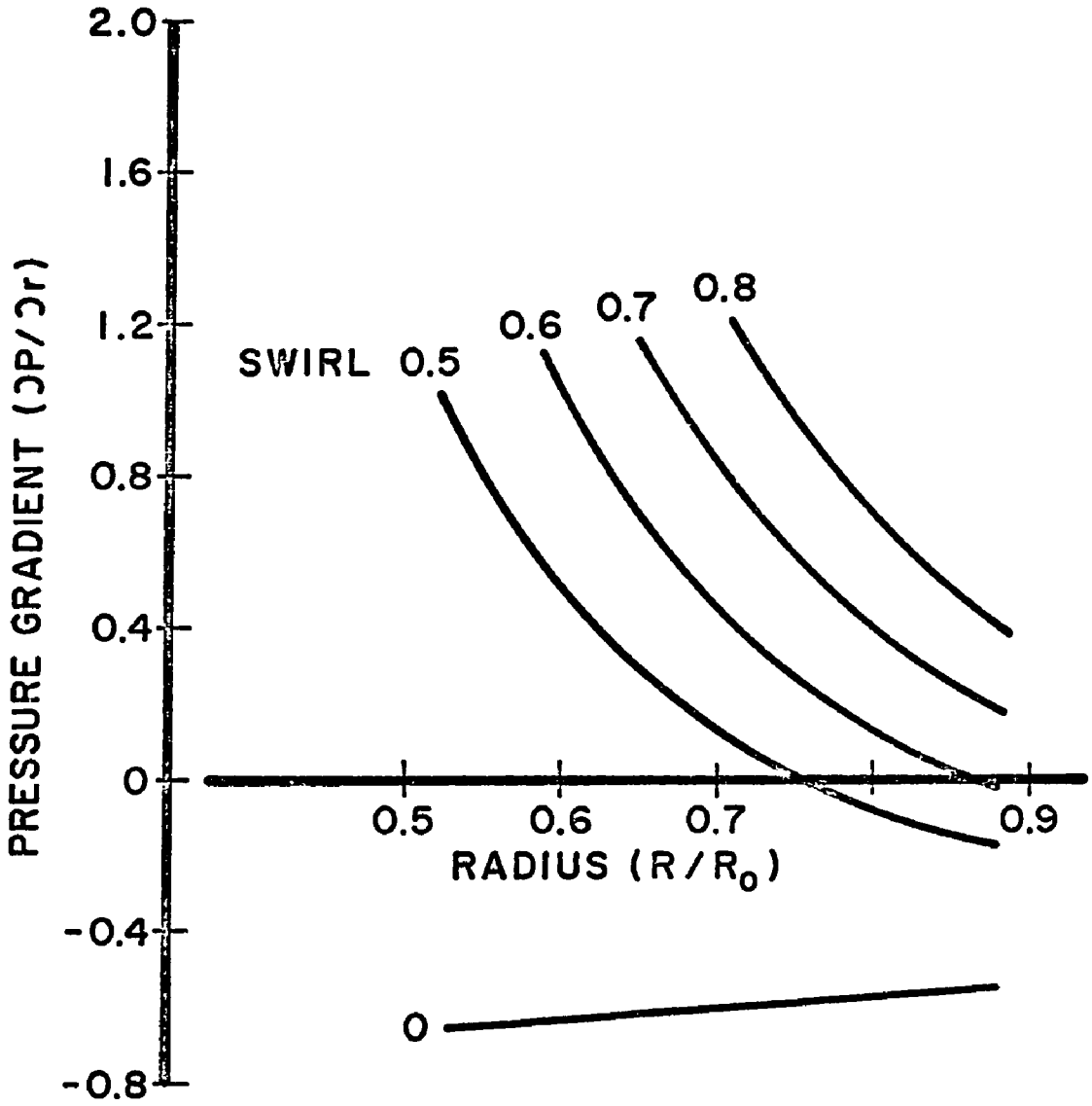

Figure 33 Theoretical radial pressure gardient

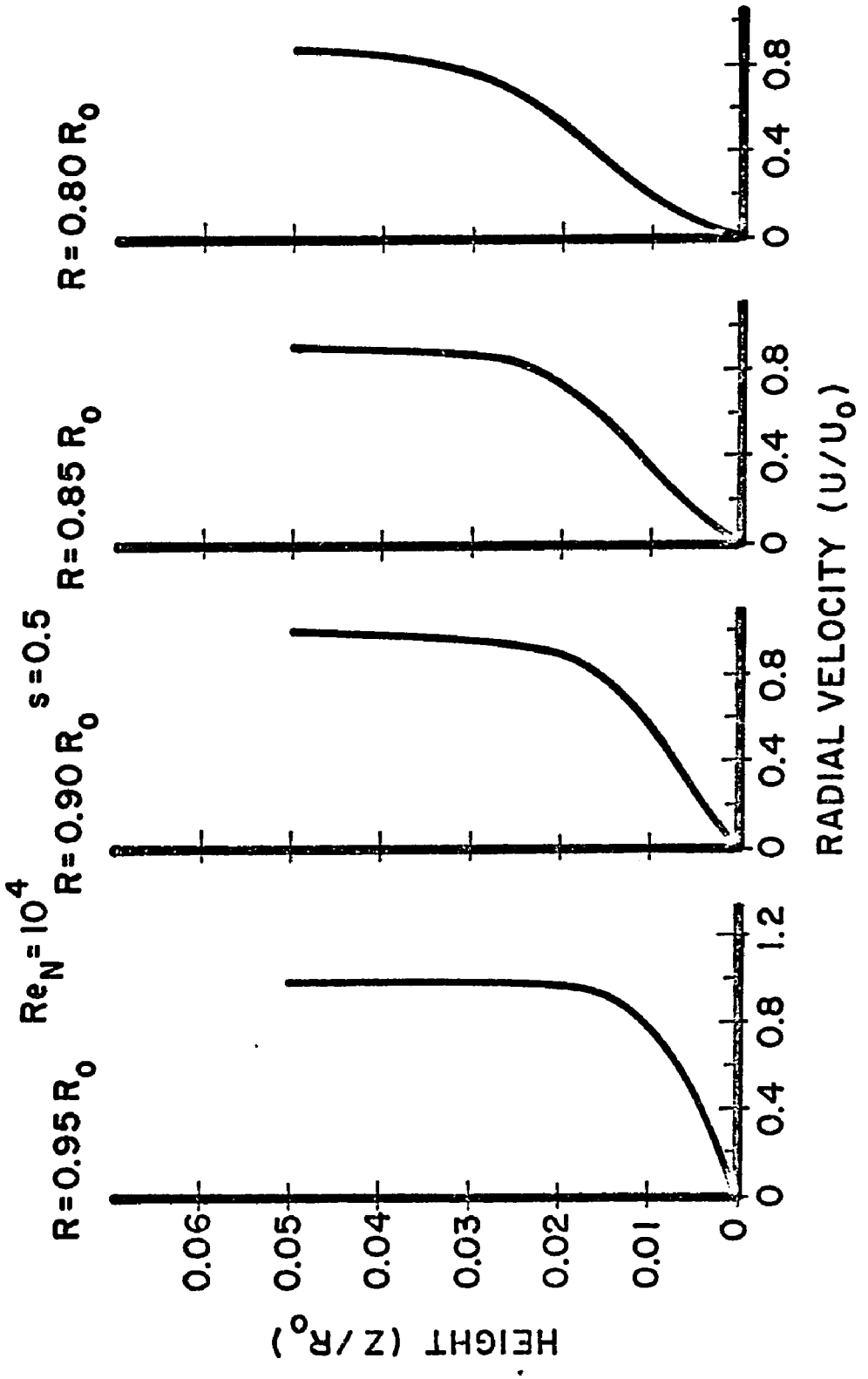

Figure 34 Development of bottom end wall boundary layer before separation

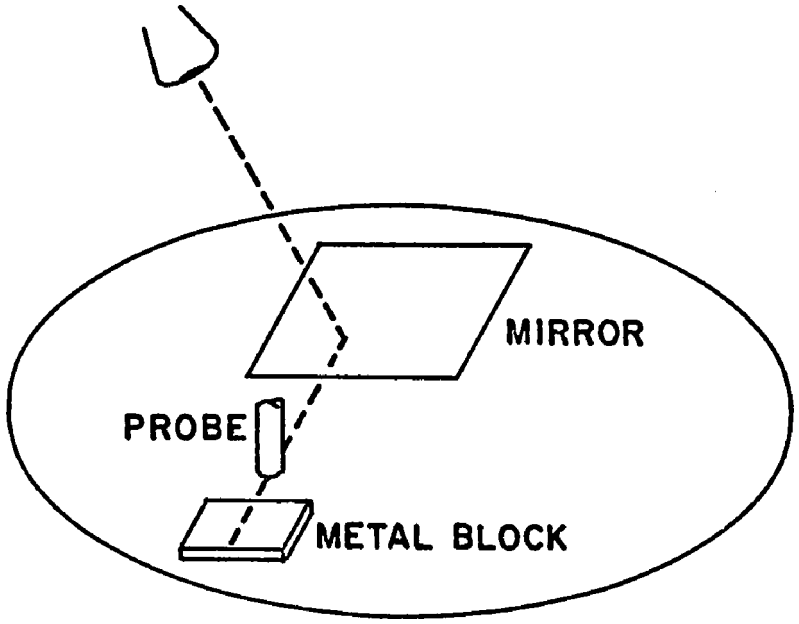

Figure 35 Probe alignment technique near bottom end wall

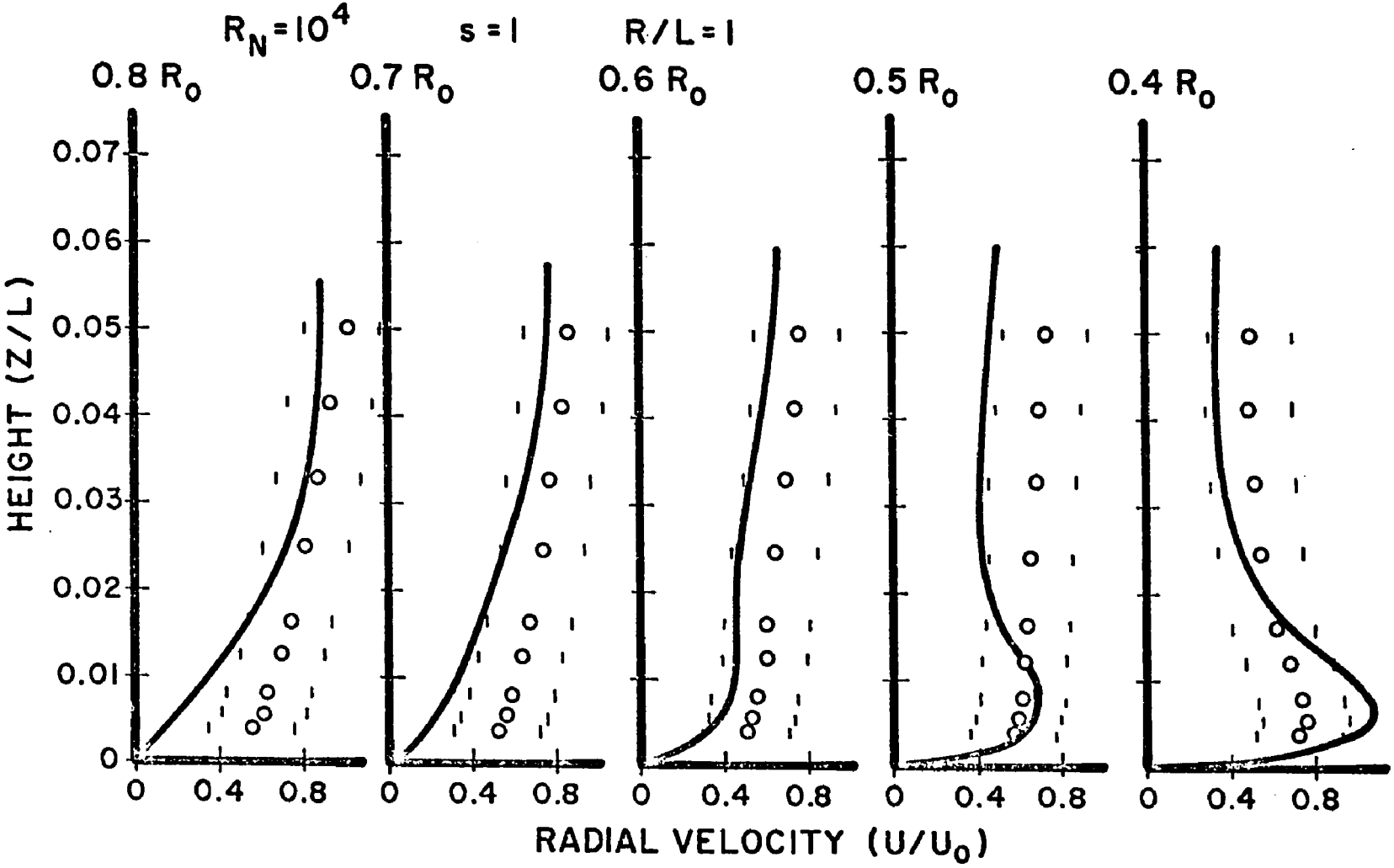

Figure 36a Bottom end wall boundary layer

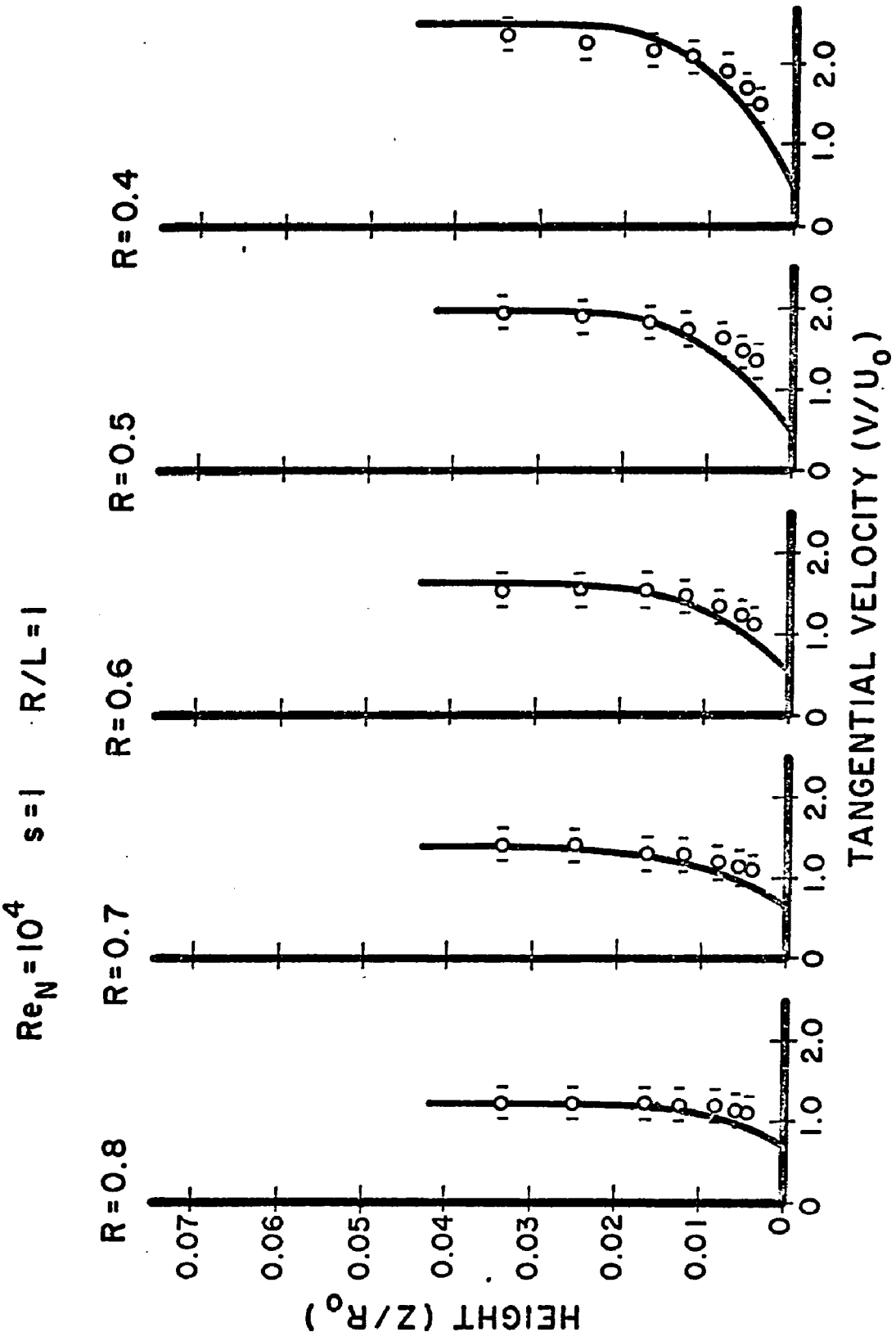

Figure 36b Bottom end wall boundary layer

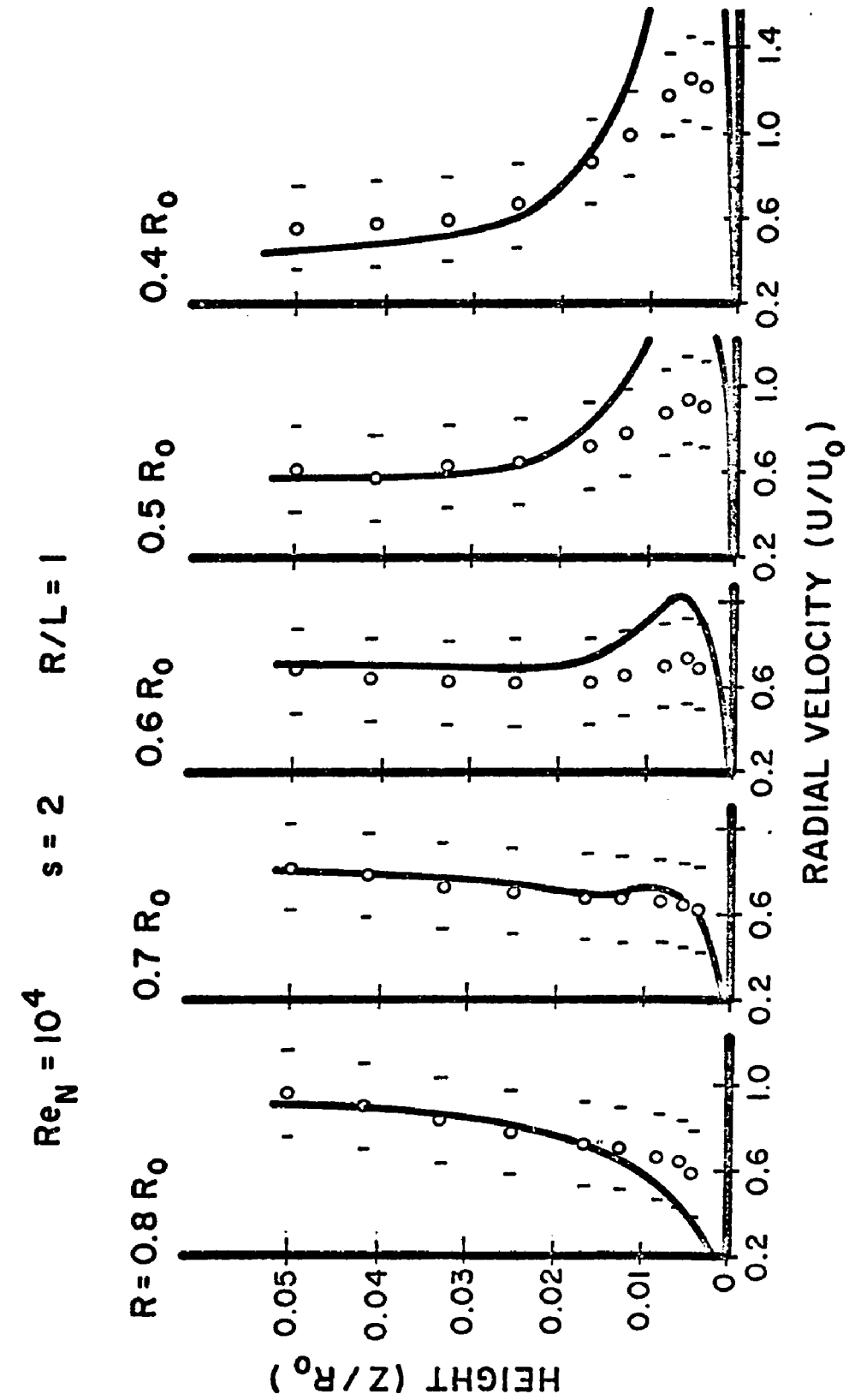

Figure 36c Bottom end wall boundary layer

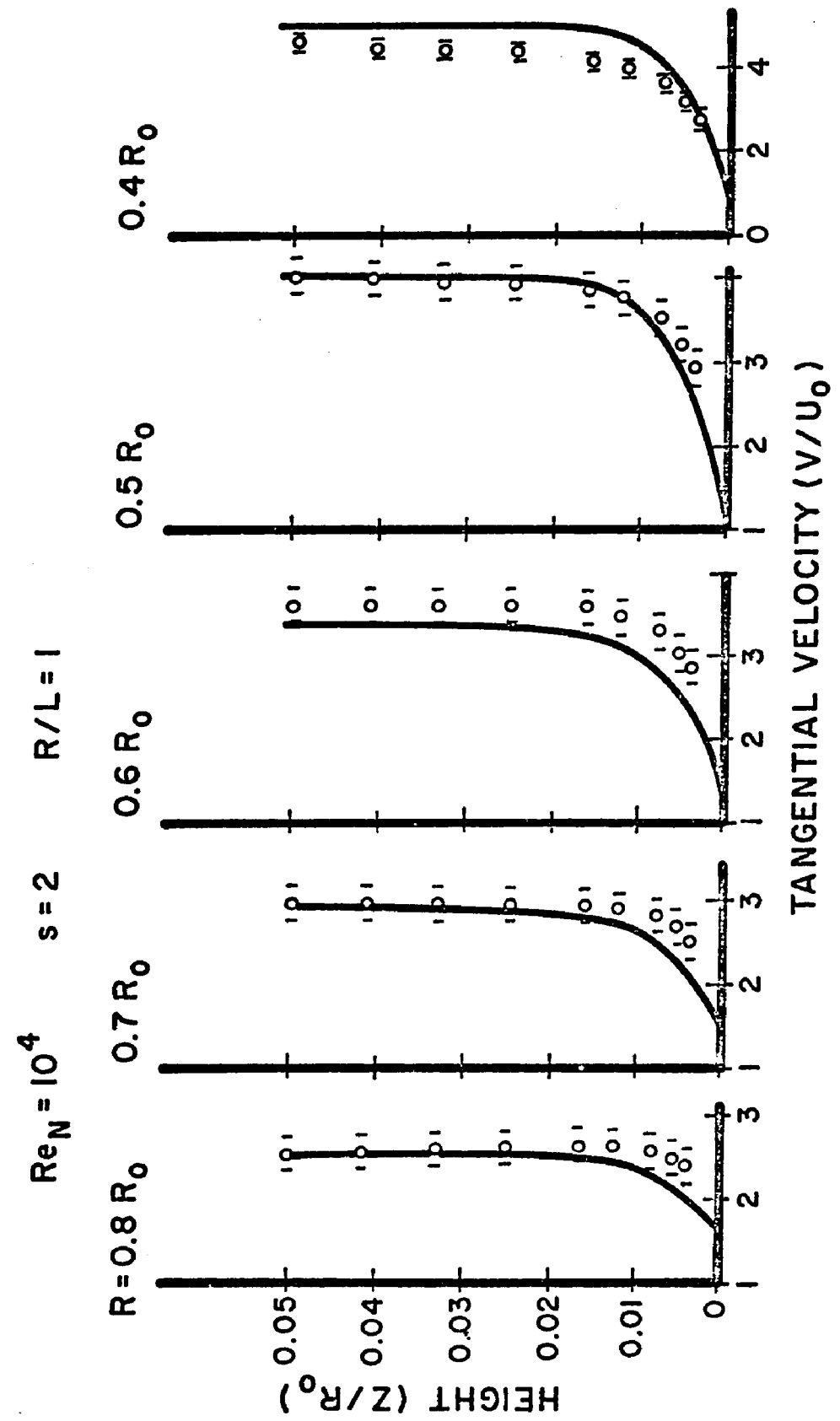

Figure 36d Bottom end wall boundary layer

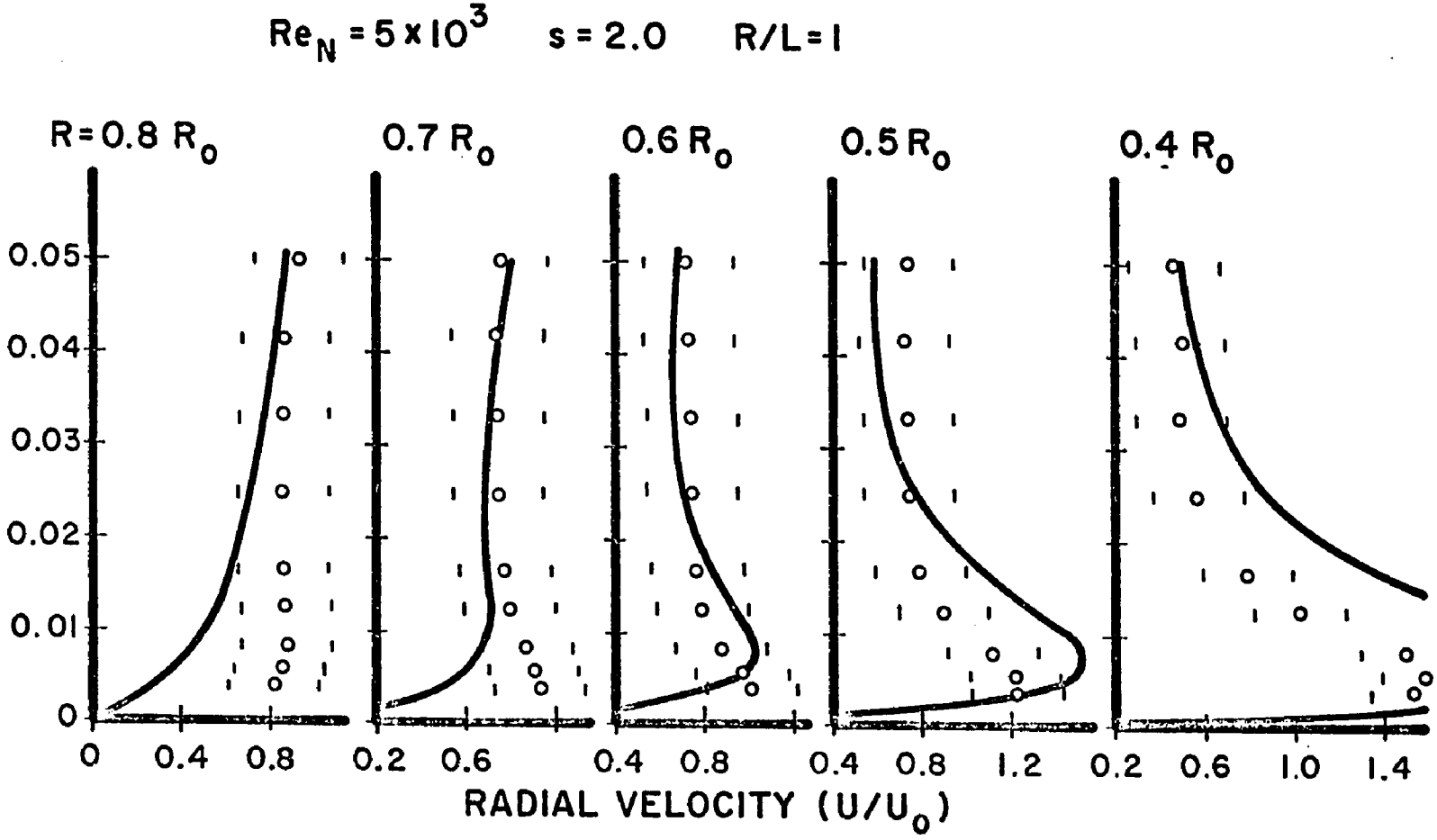

Figure 36e Bottom end wall boundary layer

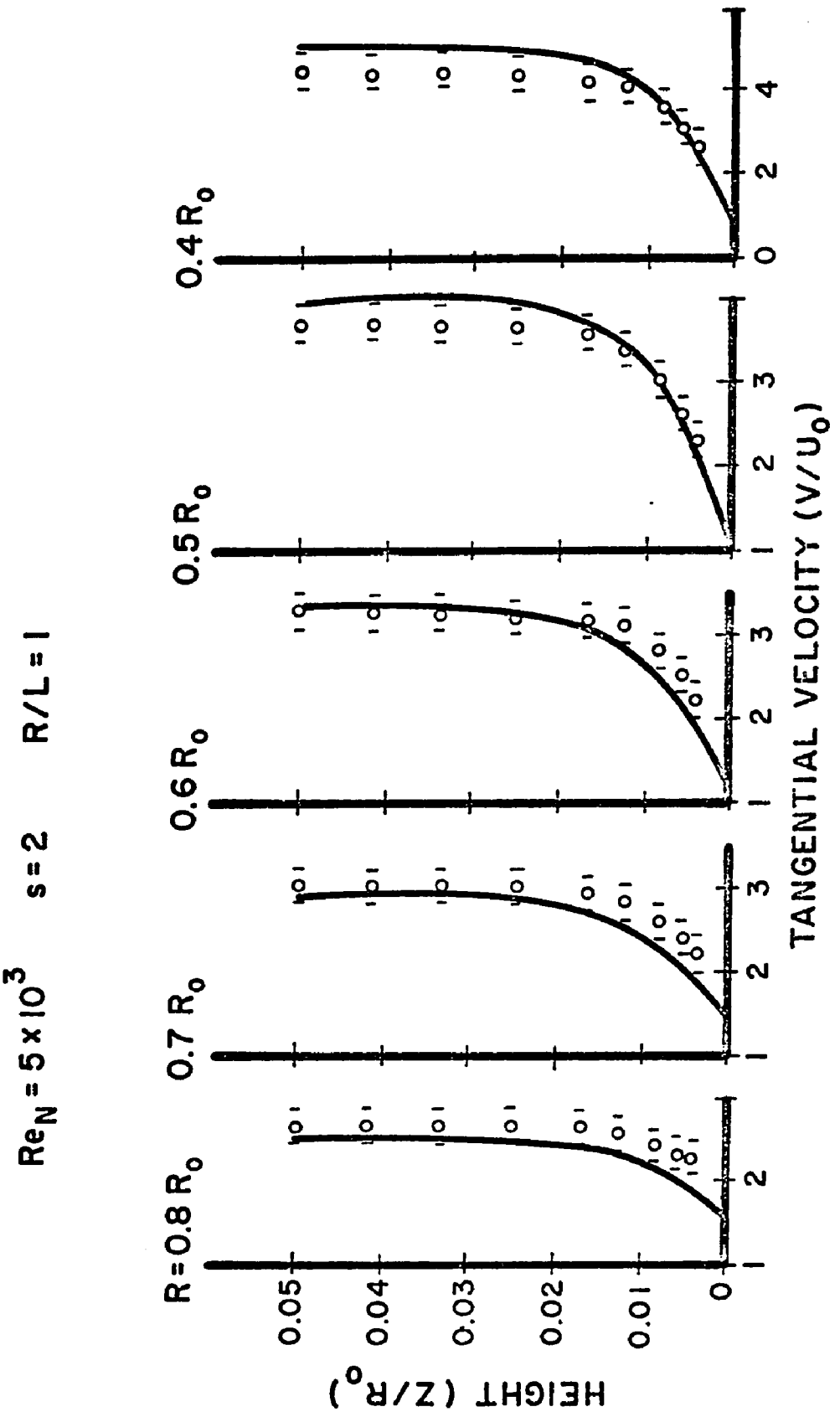

Figure 36f Bottom end wall boundary layer

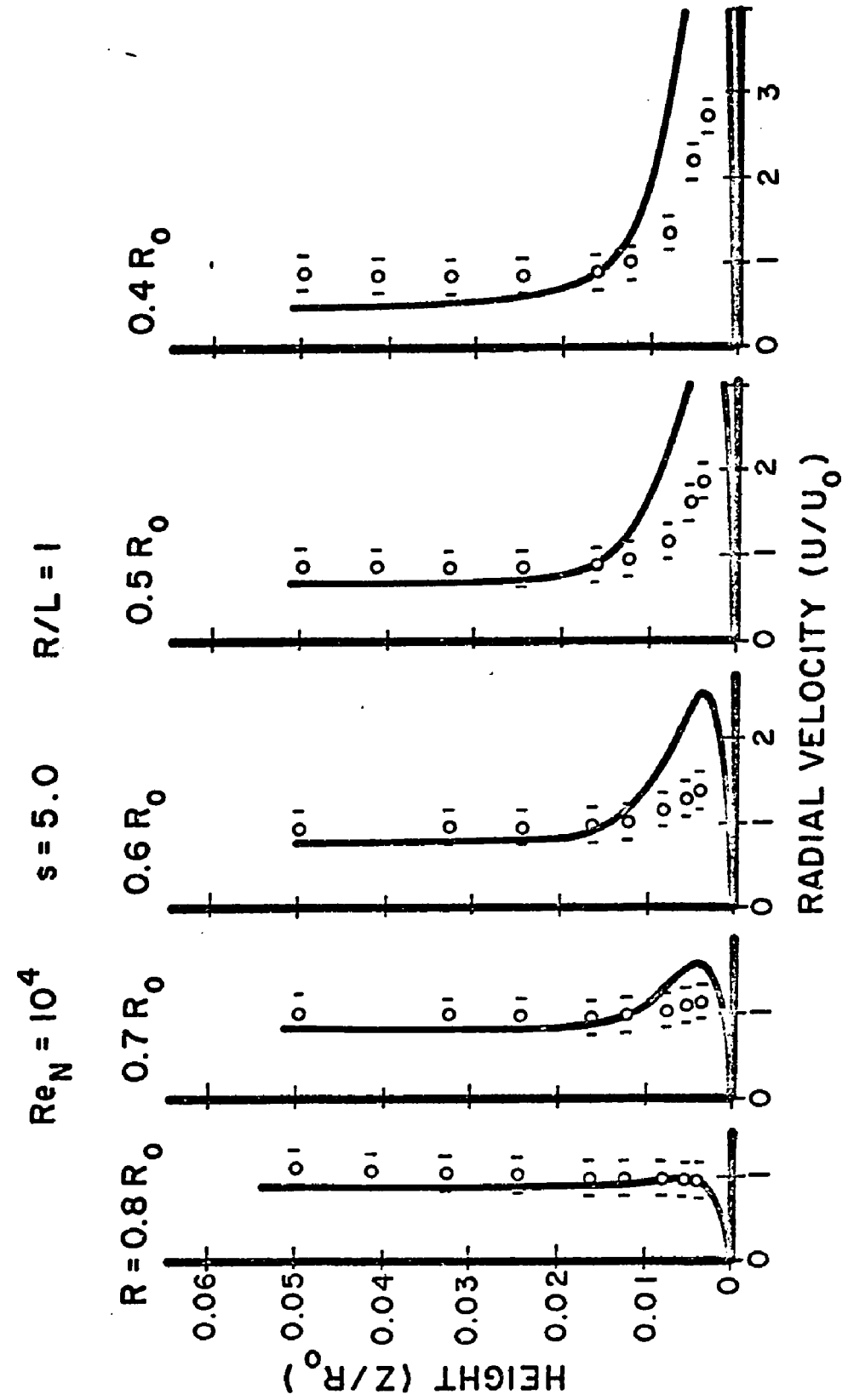

Figure 36g Bottom end wall boundary layer

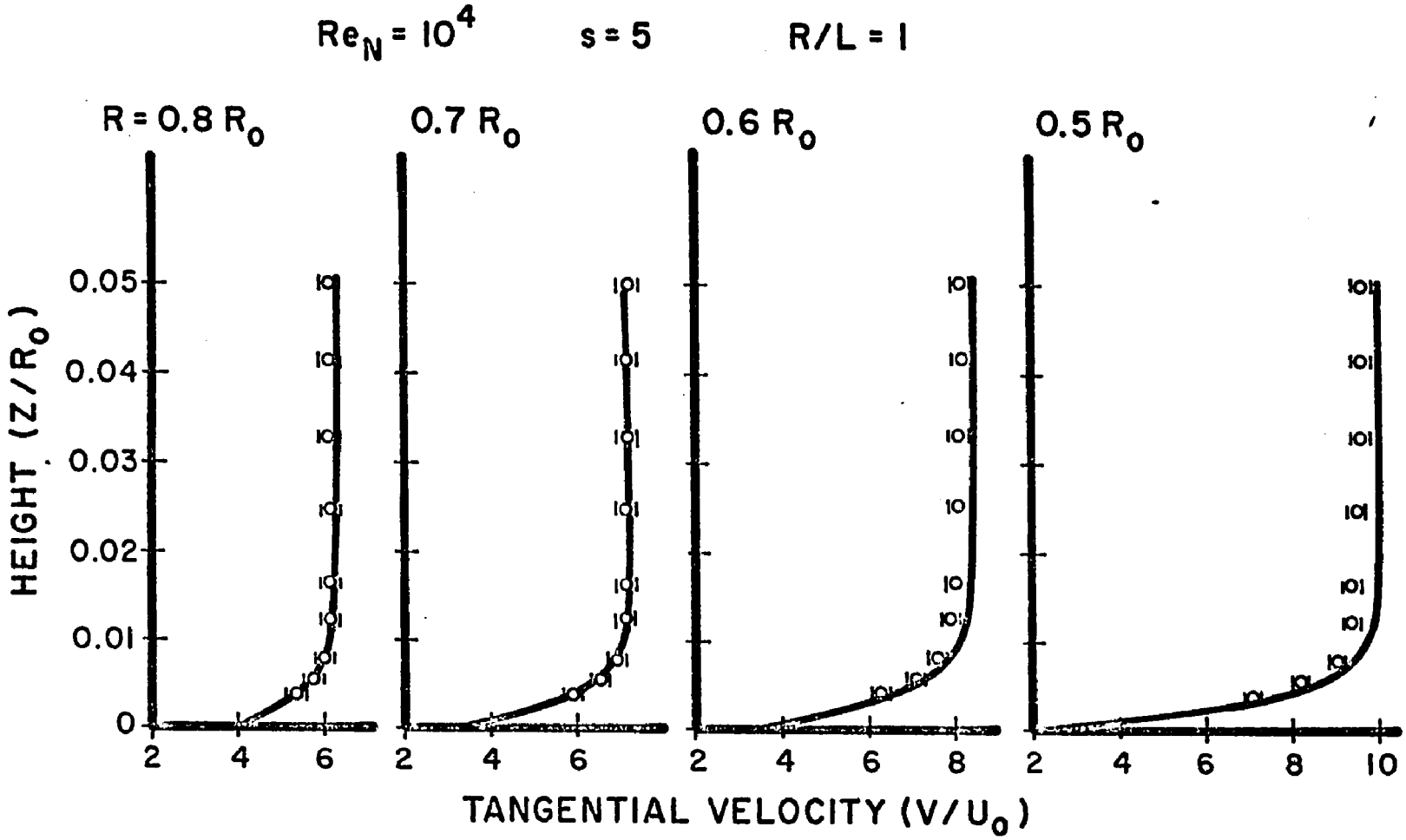

Figure 36h Bottom end wall boundary layer

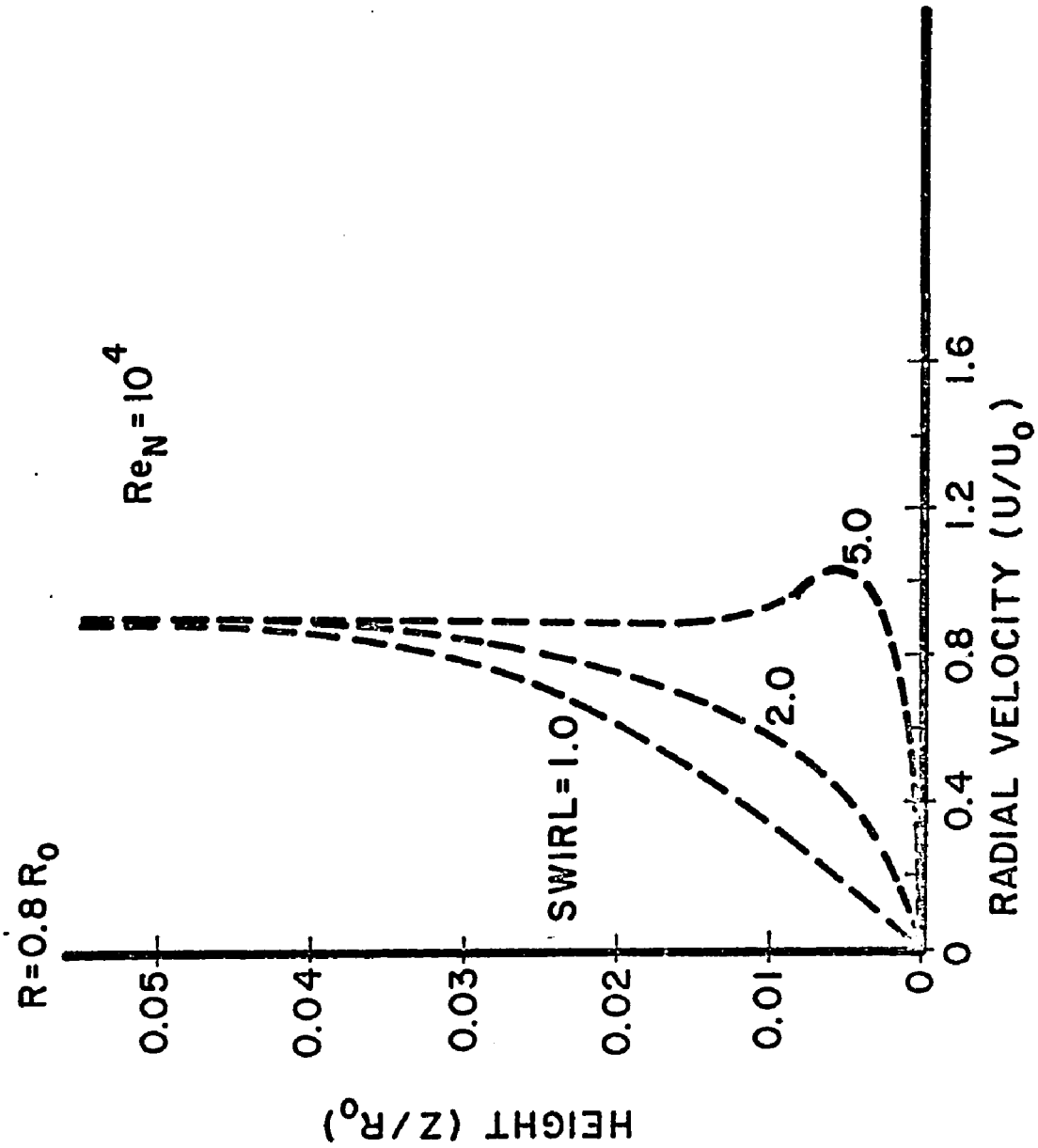

Figure 37 Theoretical radial velocity profile comparison r = 0.8

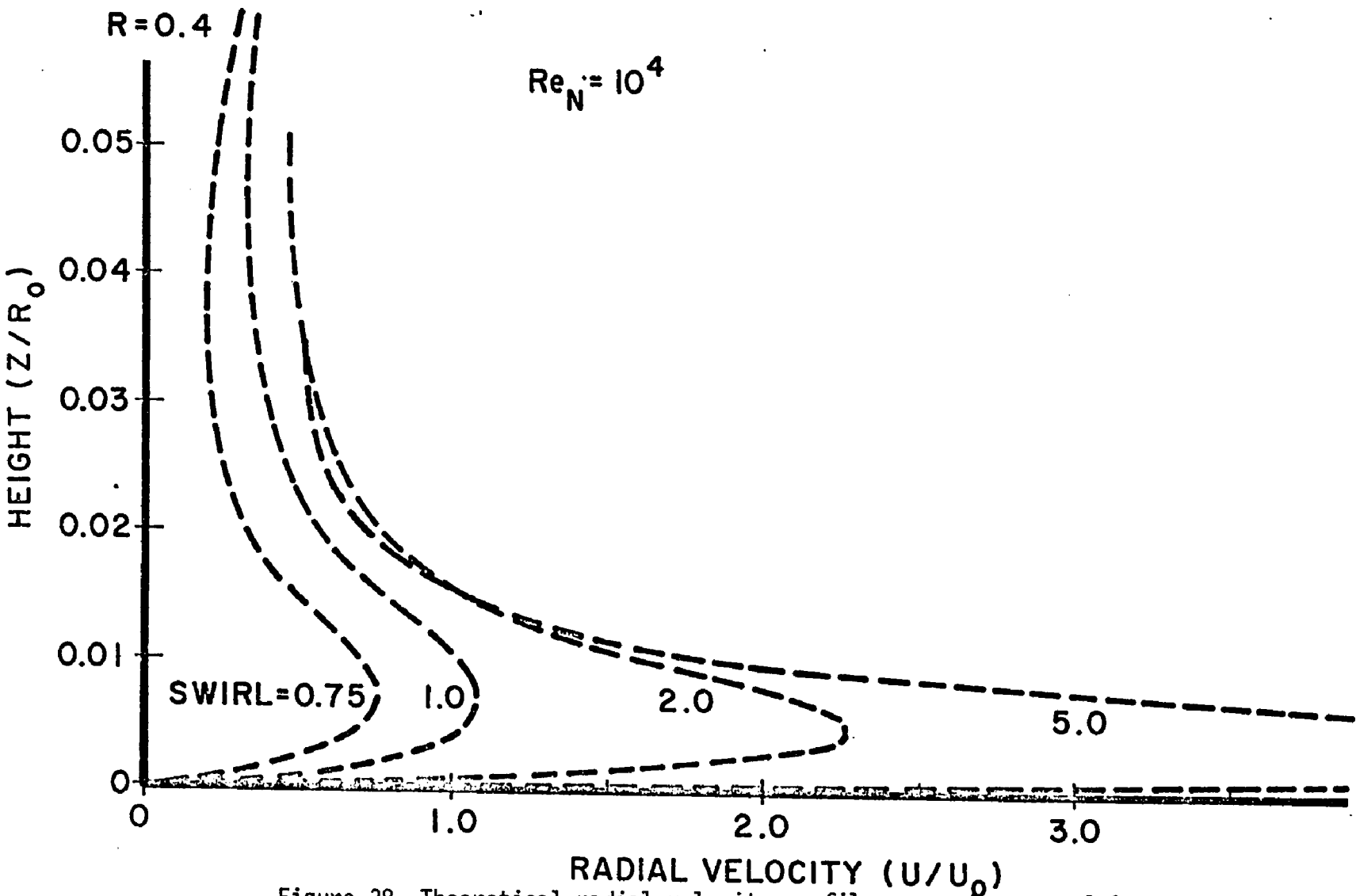

Figure 38 Theoretical radial velocity profile comparison r = 0.4

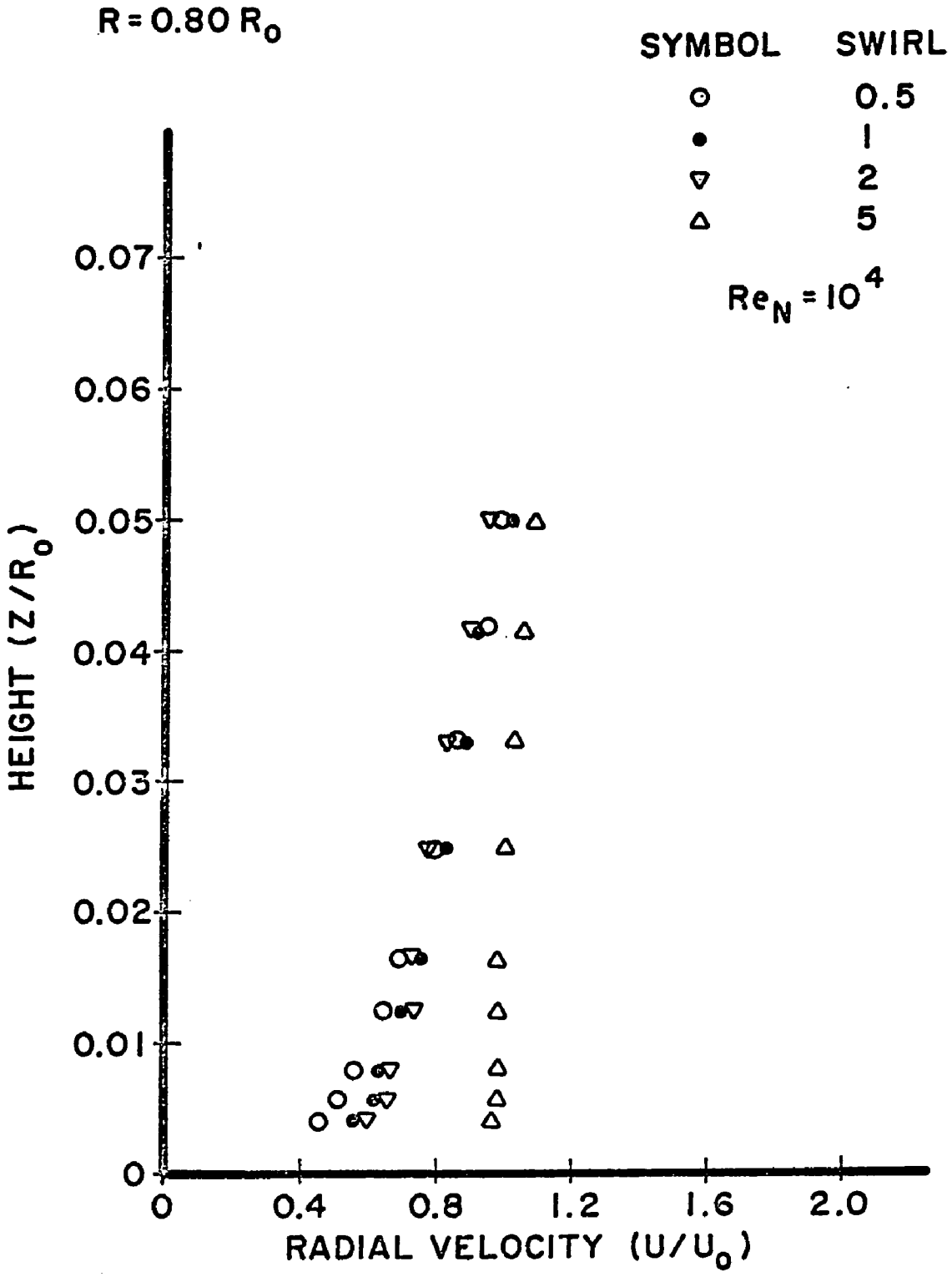

Figure 39 Experimental radial velocity profile comparison r=0.8

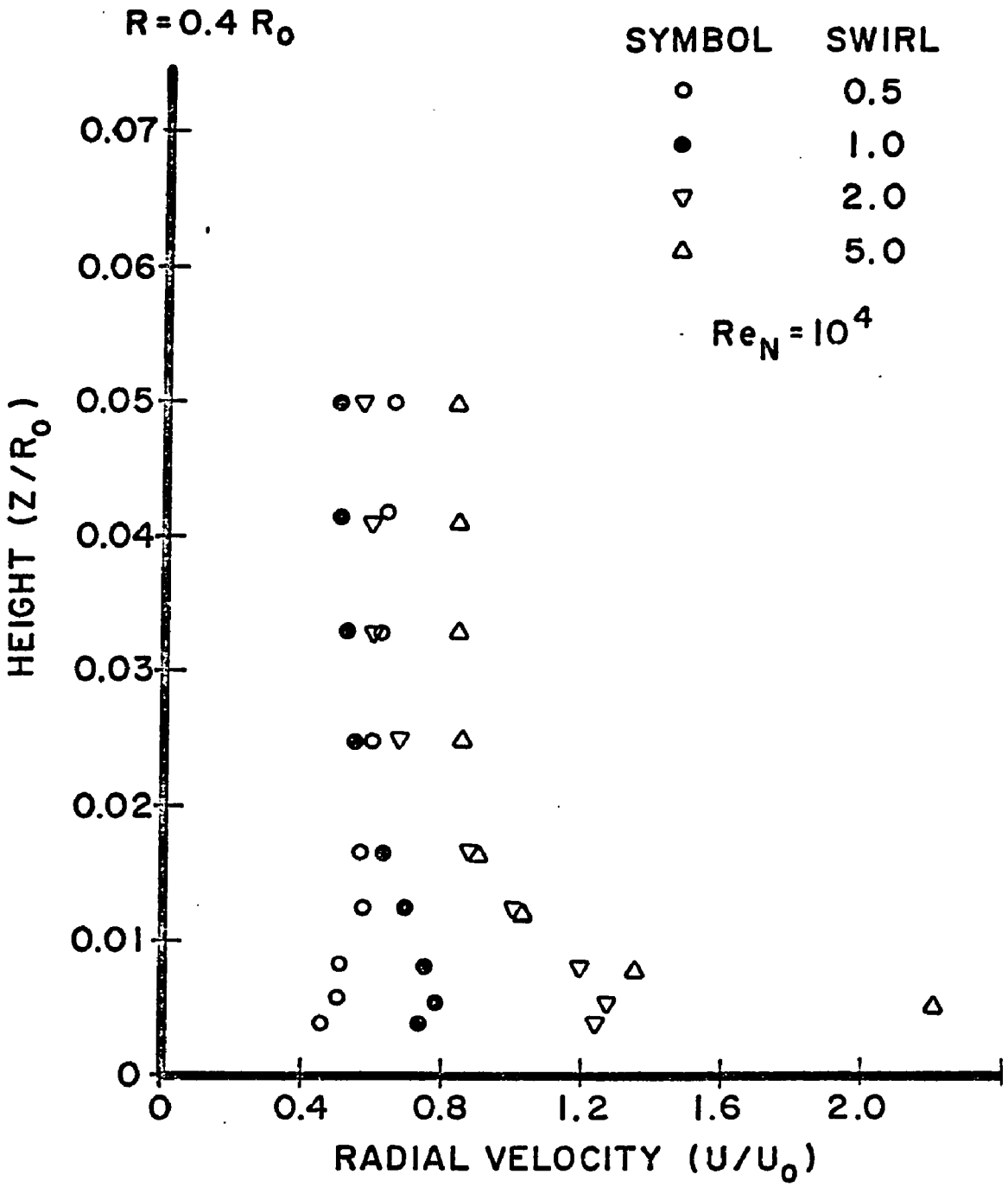

Figure 40 Experimental radial velocity profile comparison r = 0.4

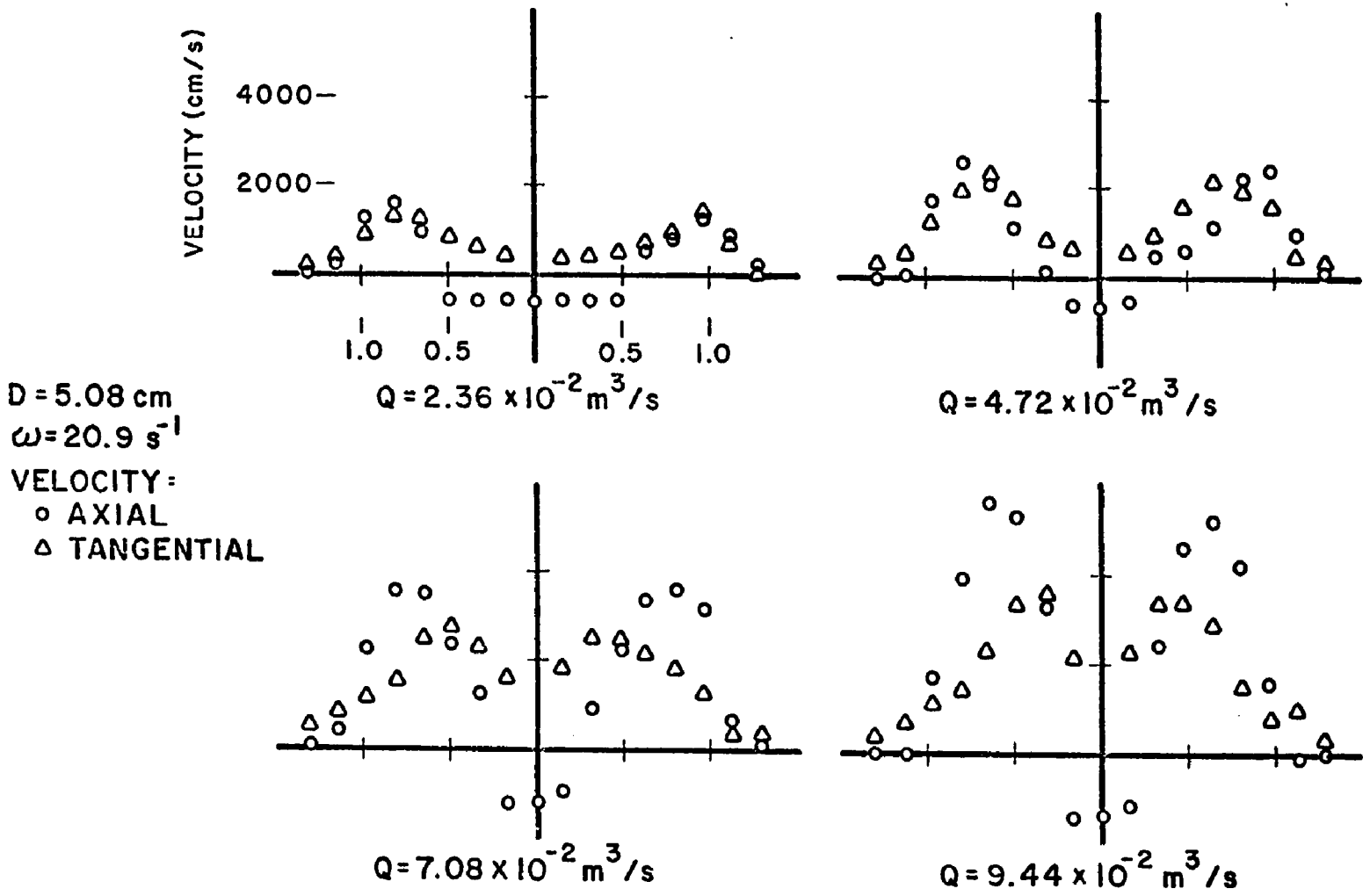

Figure 41a Exit plane velocity profiles

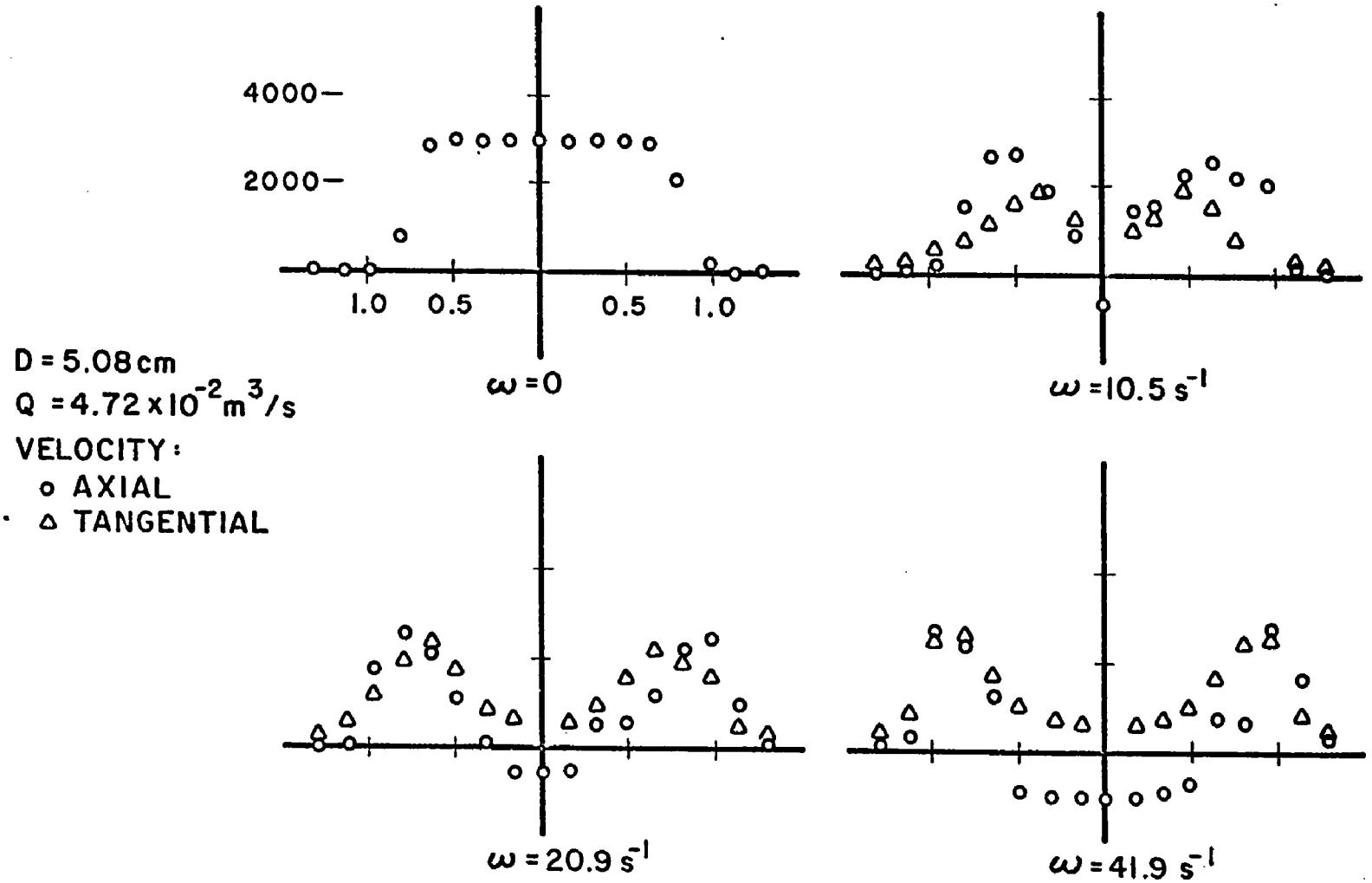

Figure 41b Exit plane velocity profiles

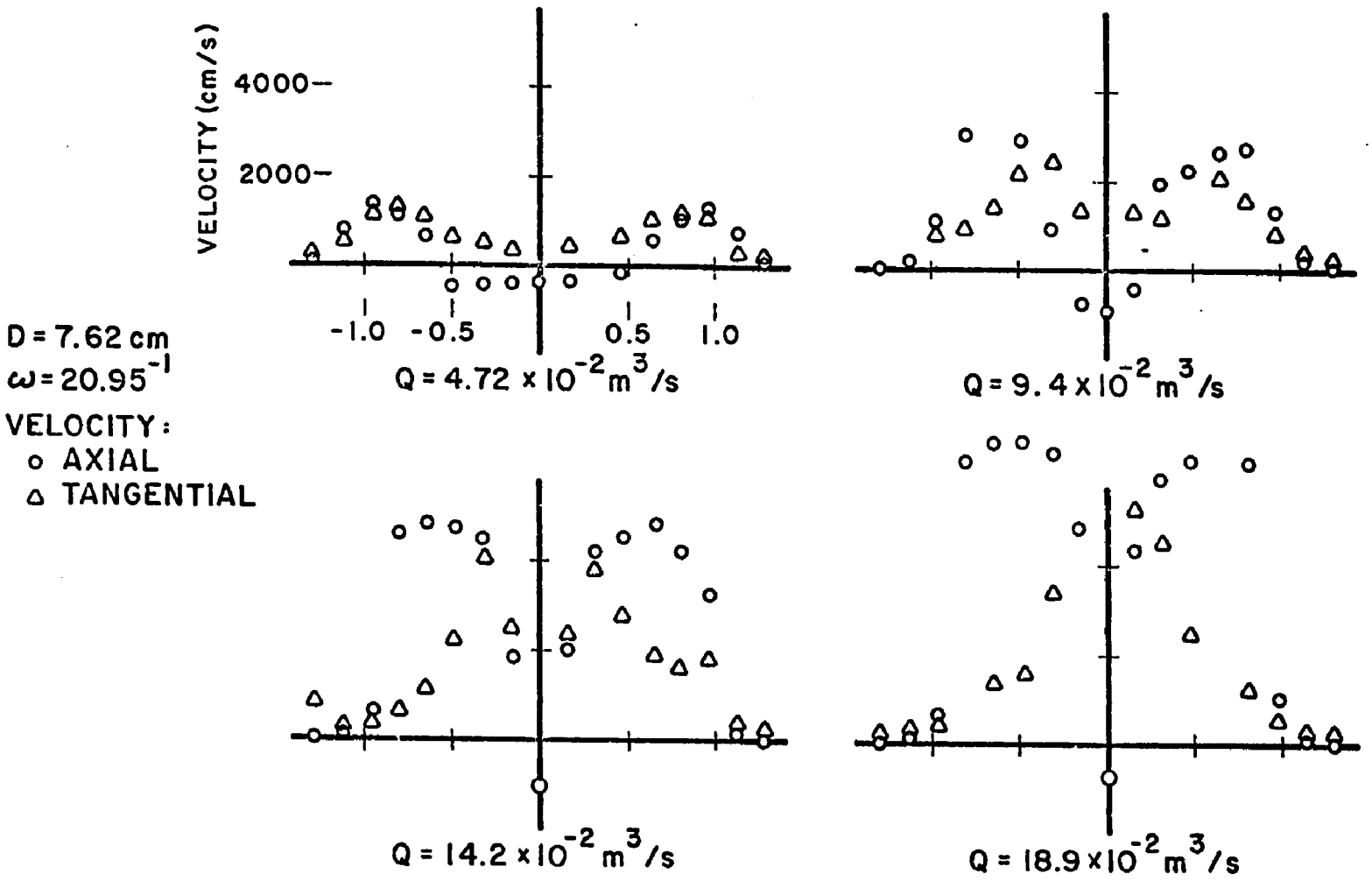

Figure 41c Exit plane velocity profiles

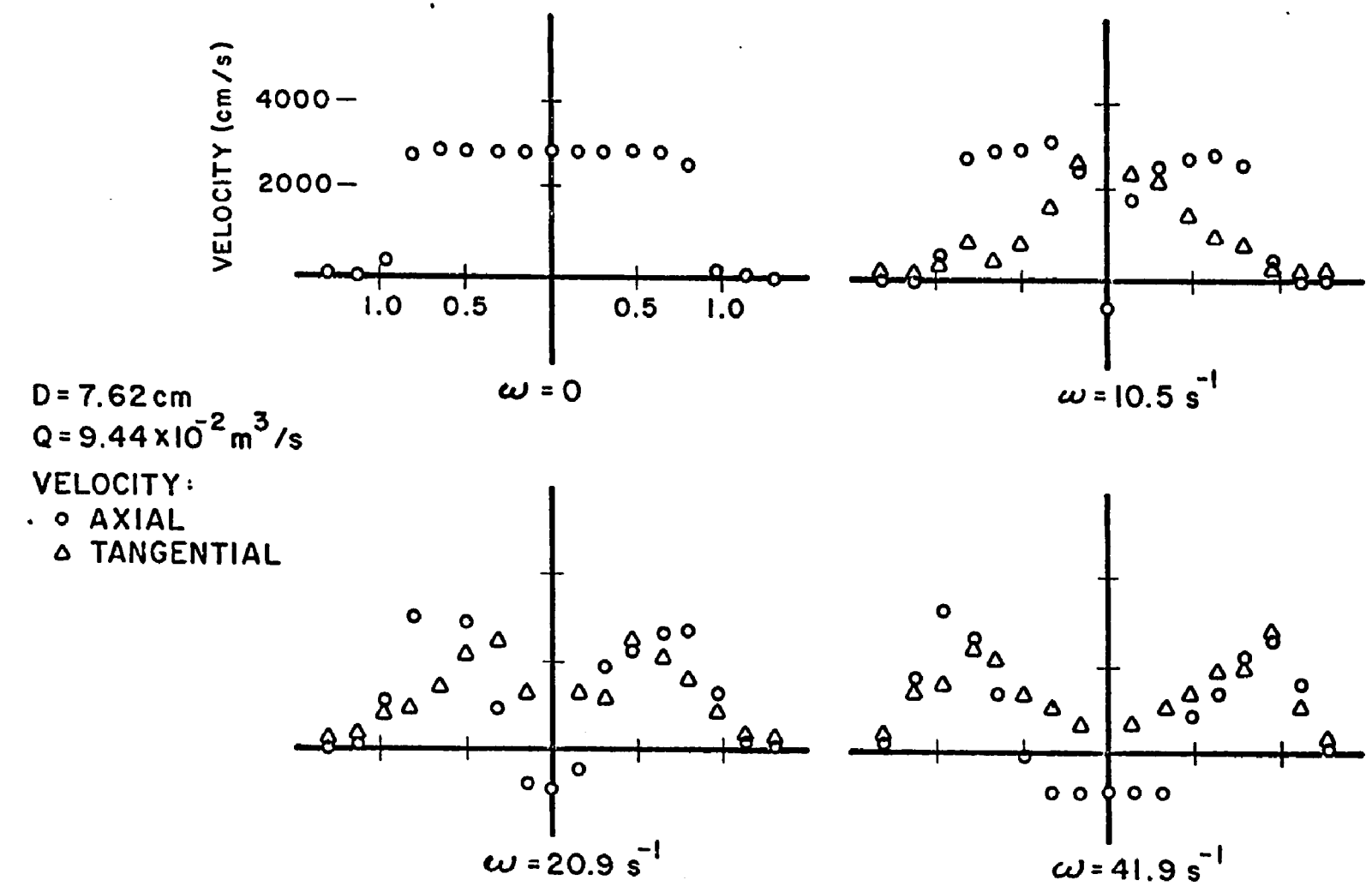

Figure 41d Exit plane velocity profiles

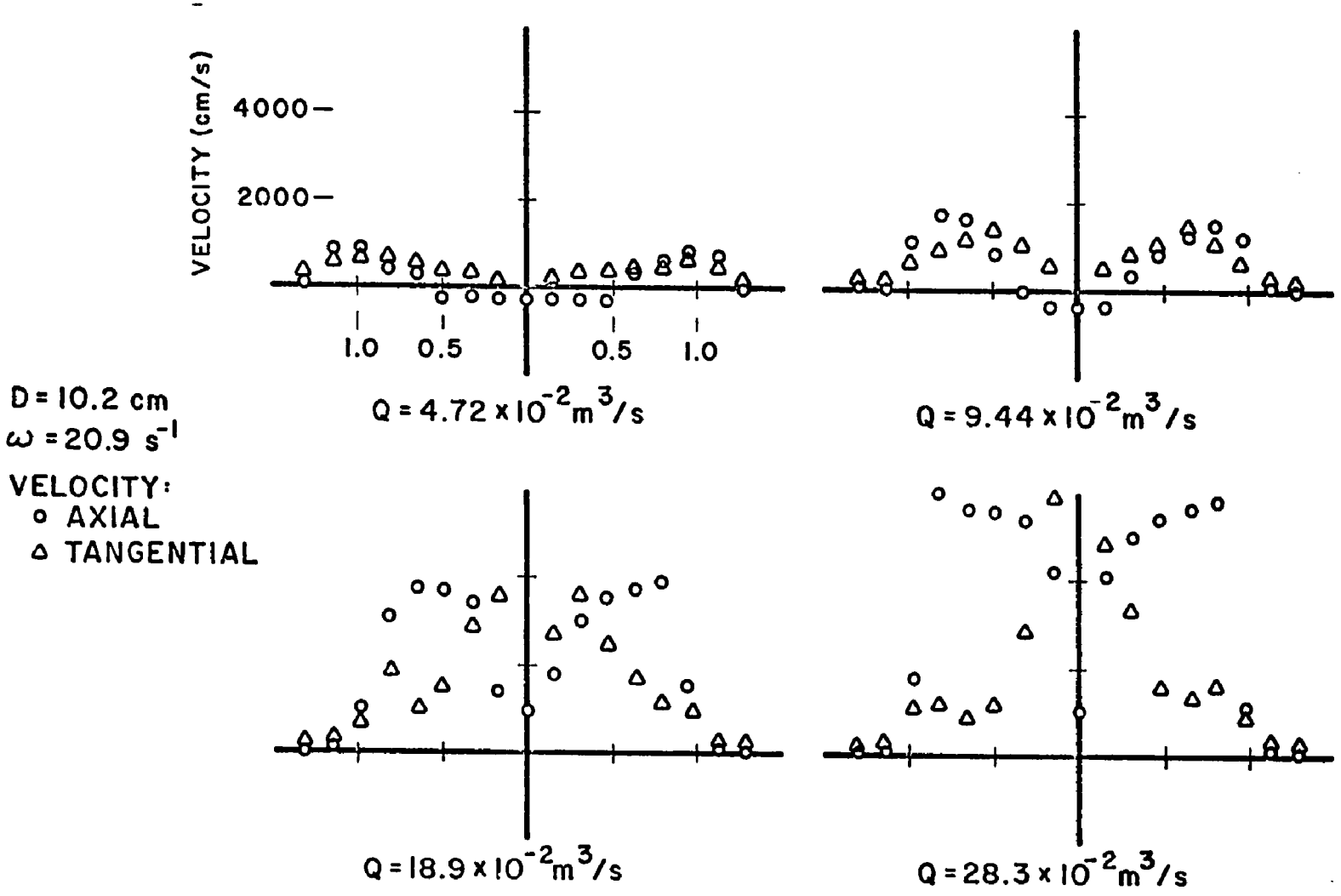

Figure 41e Exit plane velocity profiles

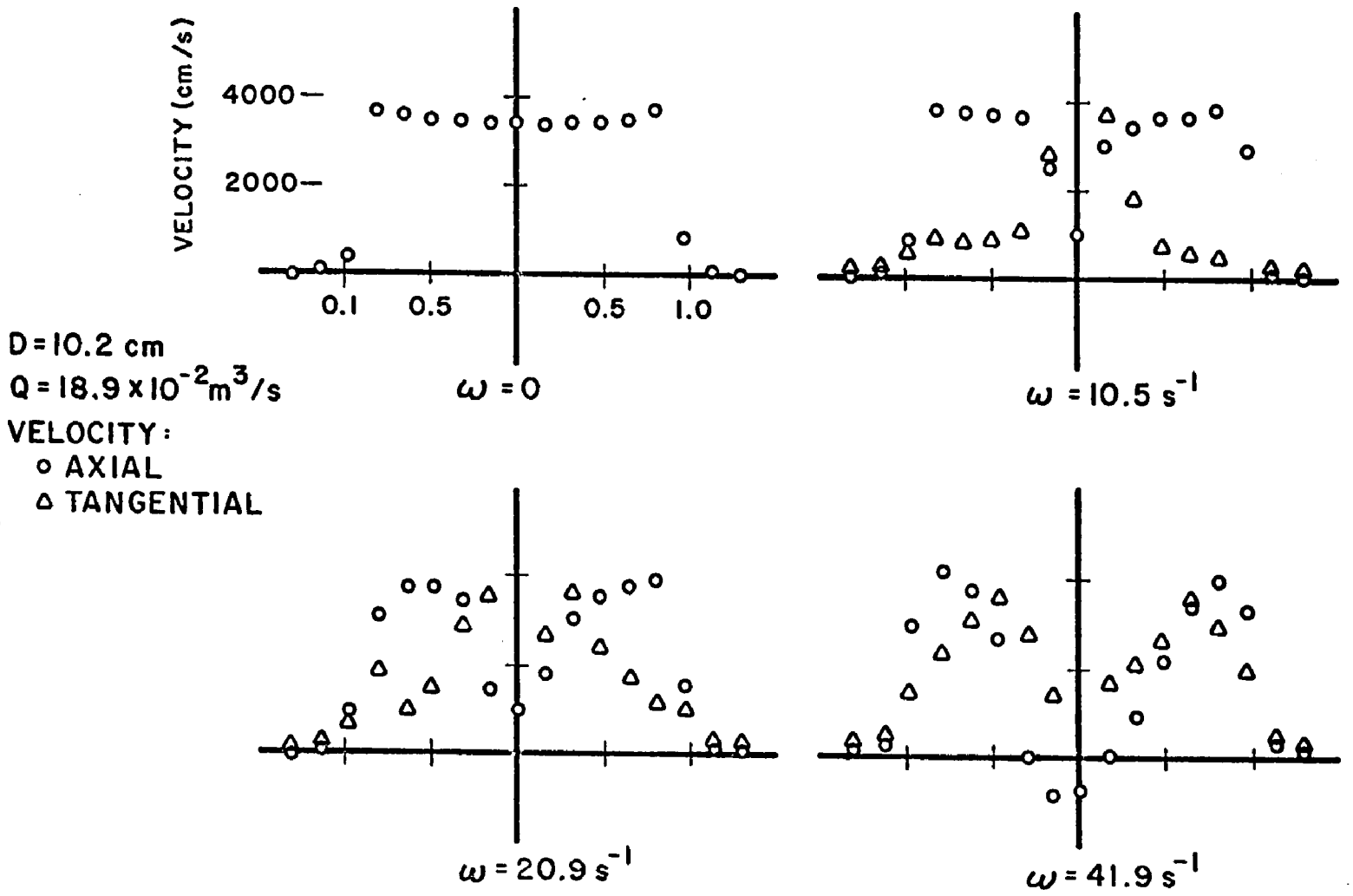

Figure 41f Exit plane velocity profiles

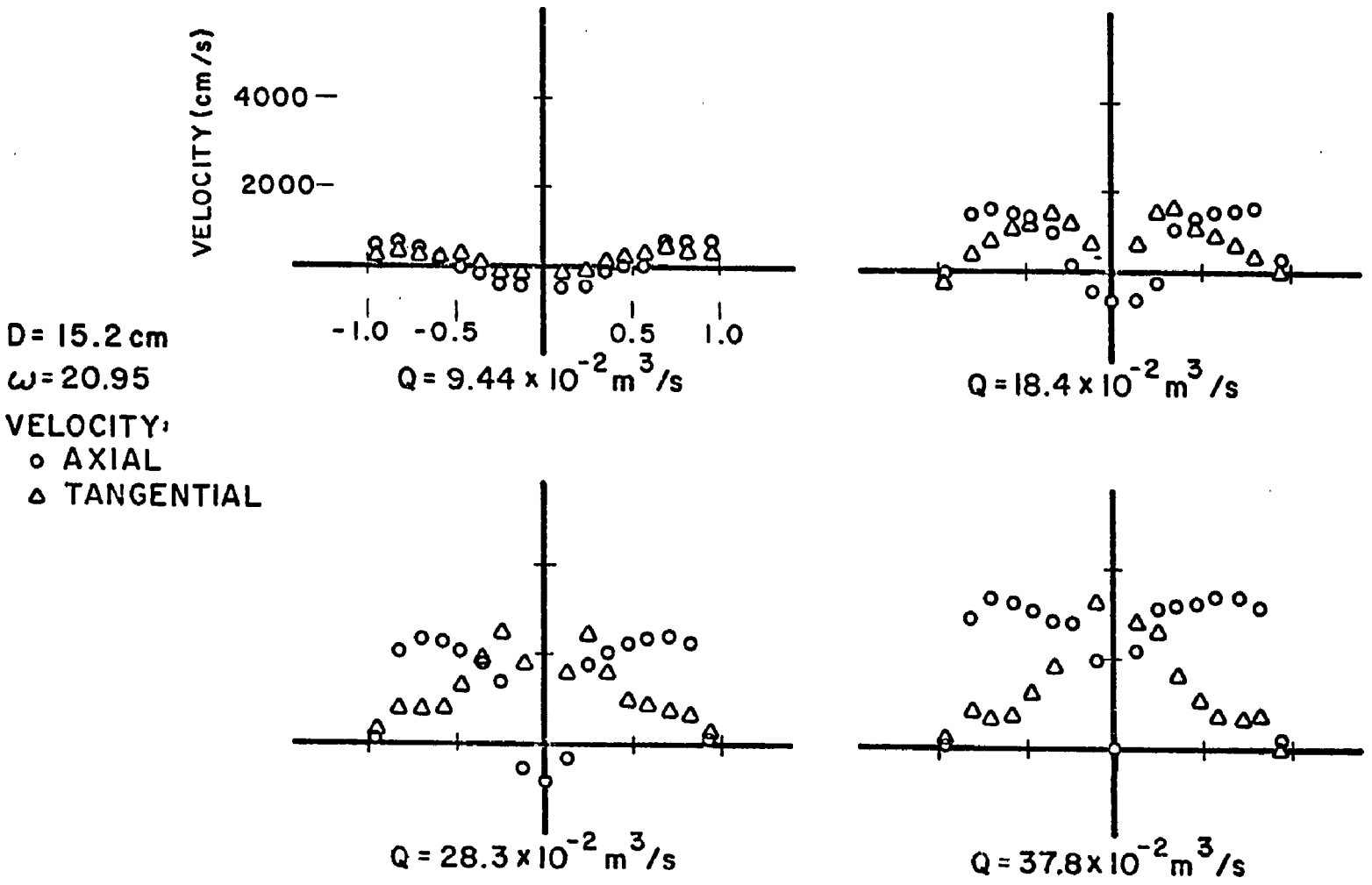

Figure 41g Exit plane velocity profiles

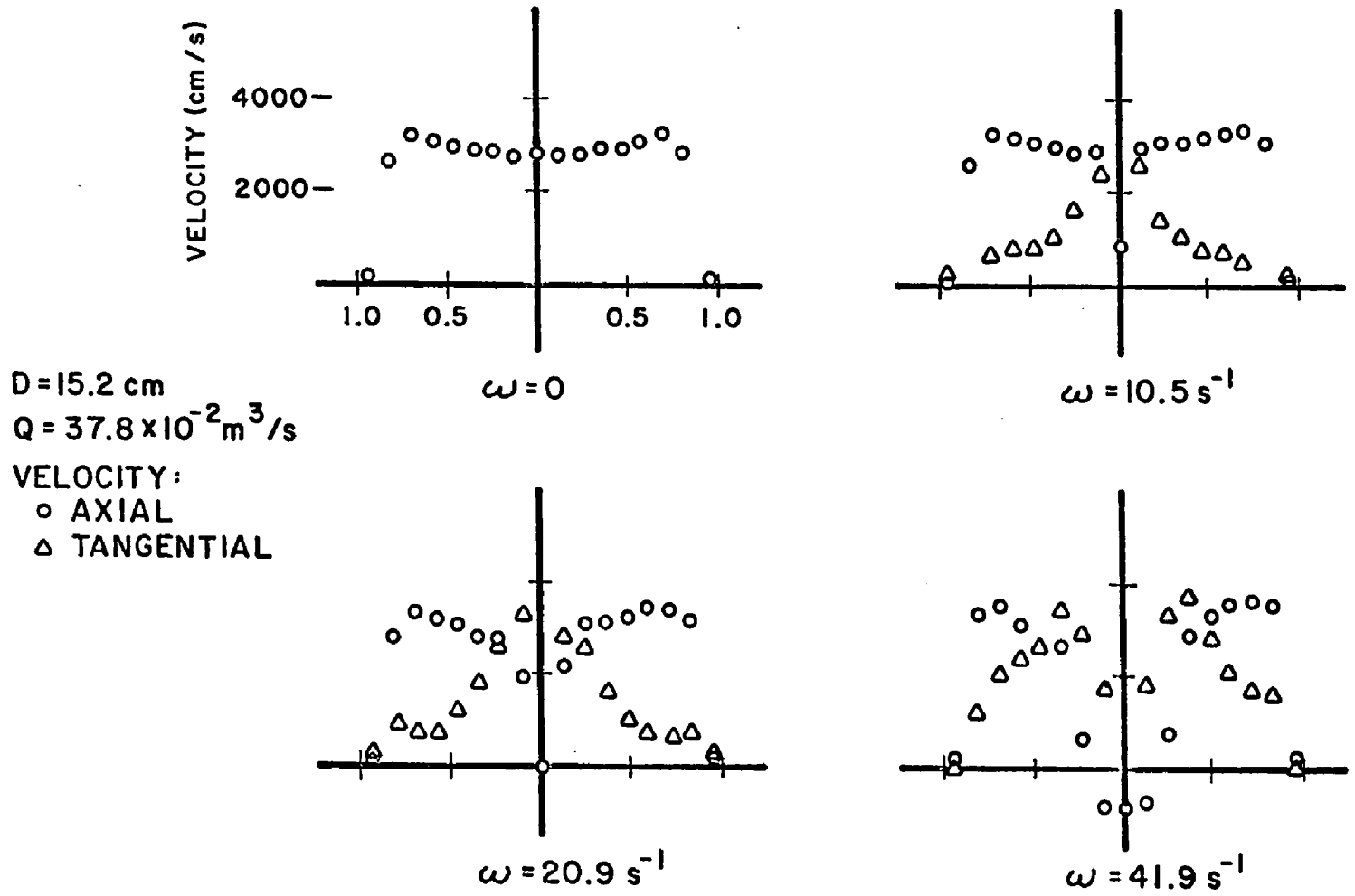

Figure 41h Exit plane velocity profiles

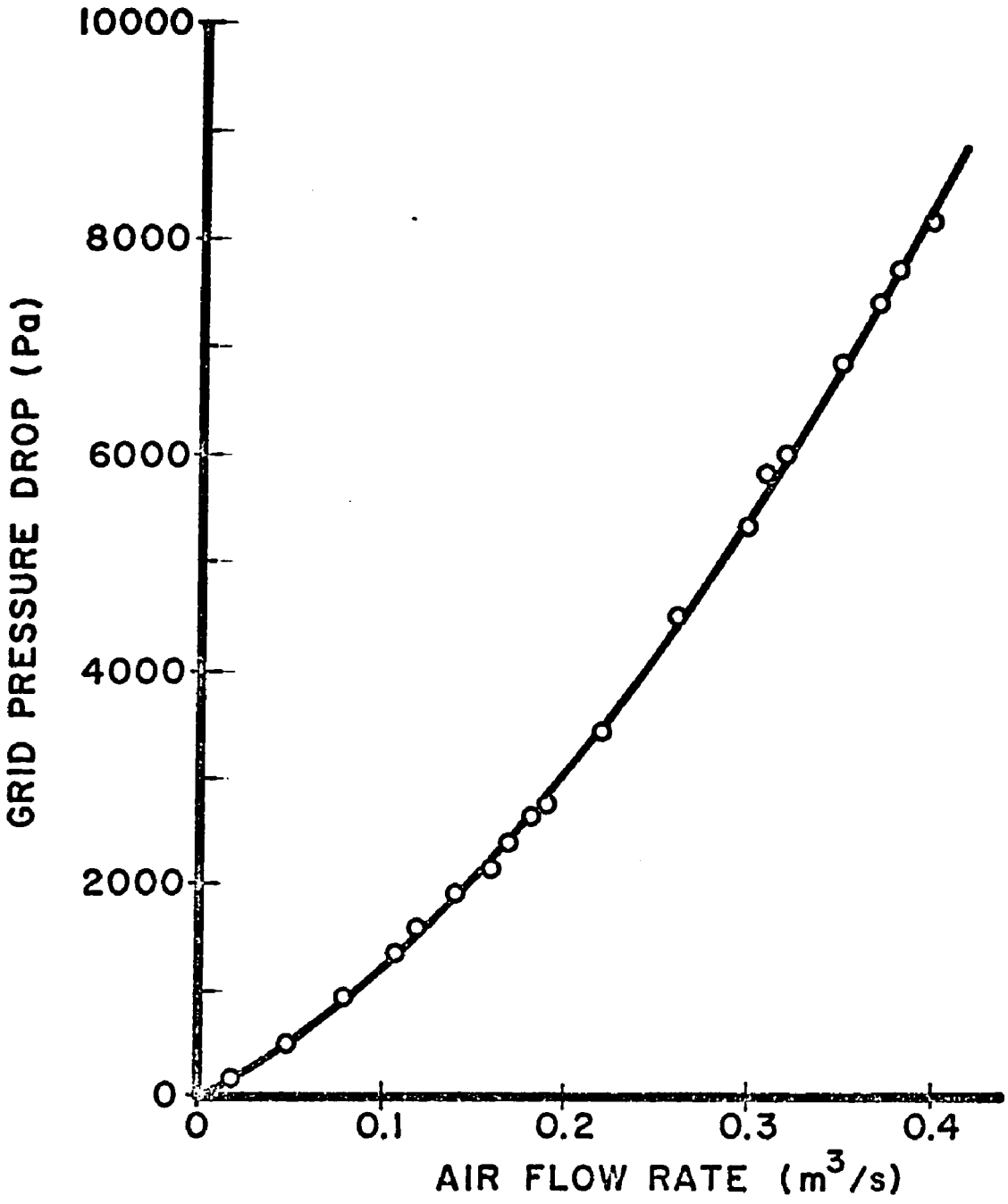

Figure 42 Grid pressure drop

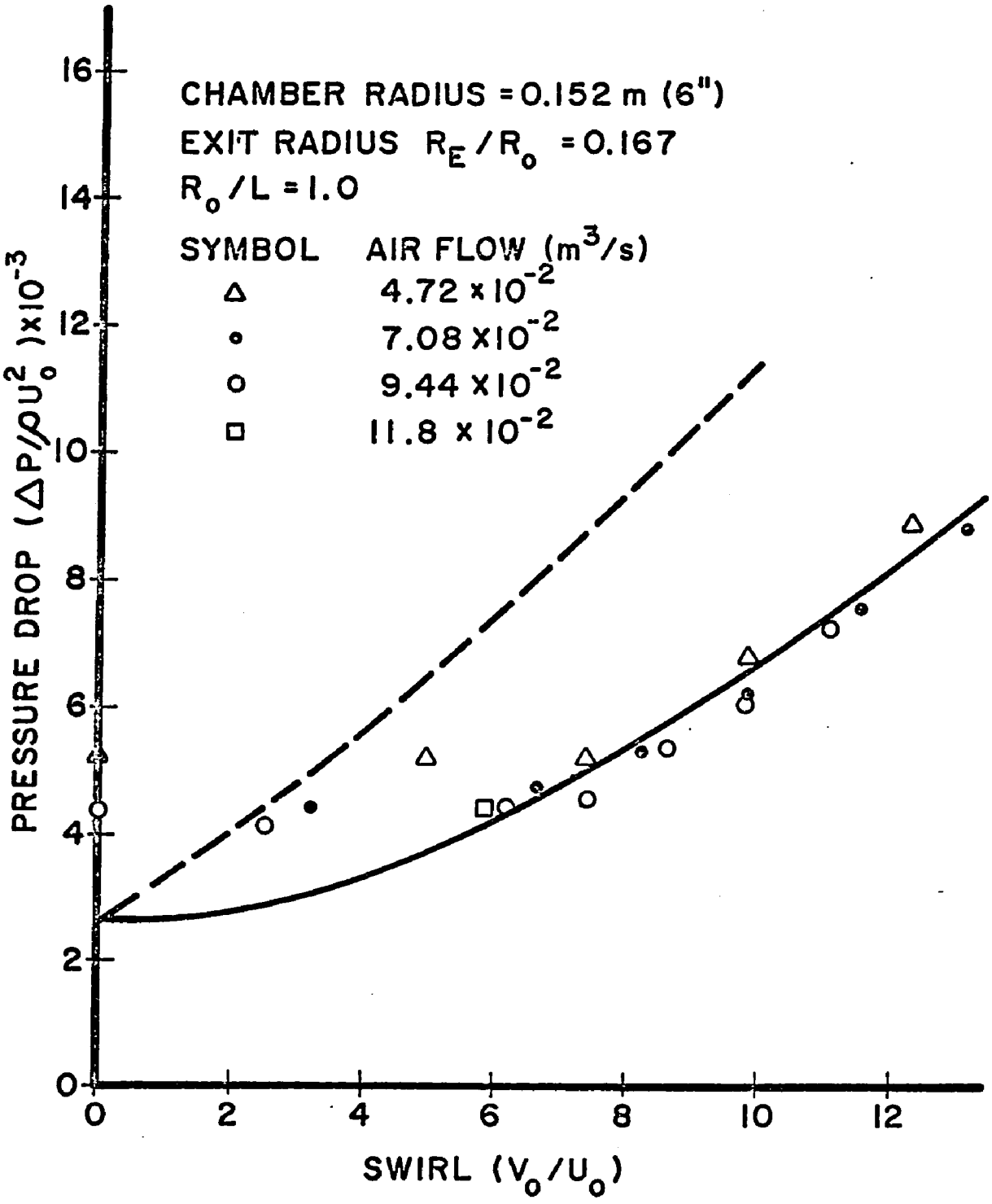

Figure 43a Chamber pressure drop

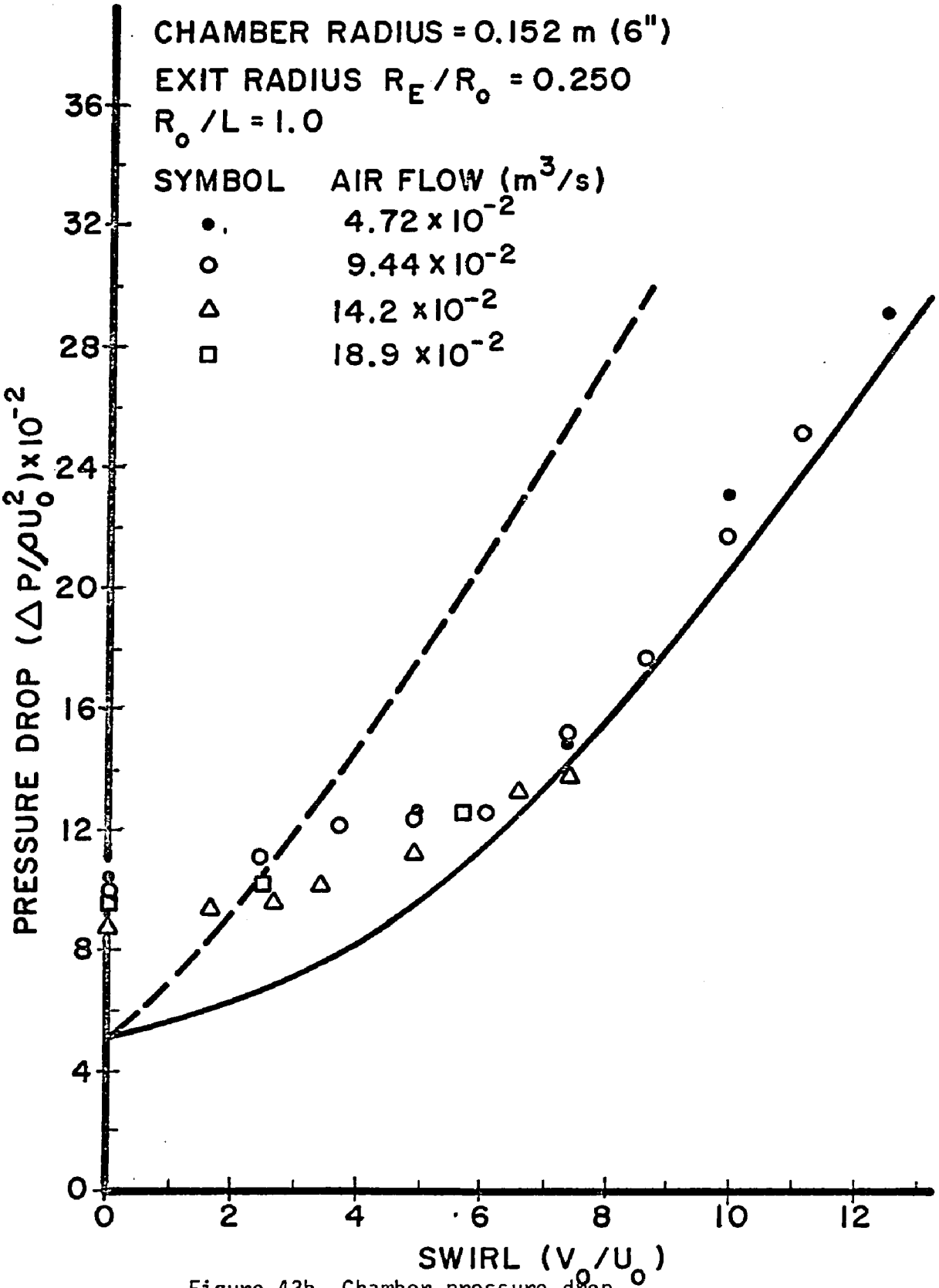

Figure 43b Chamber pressure drop

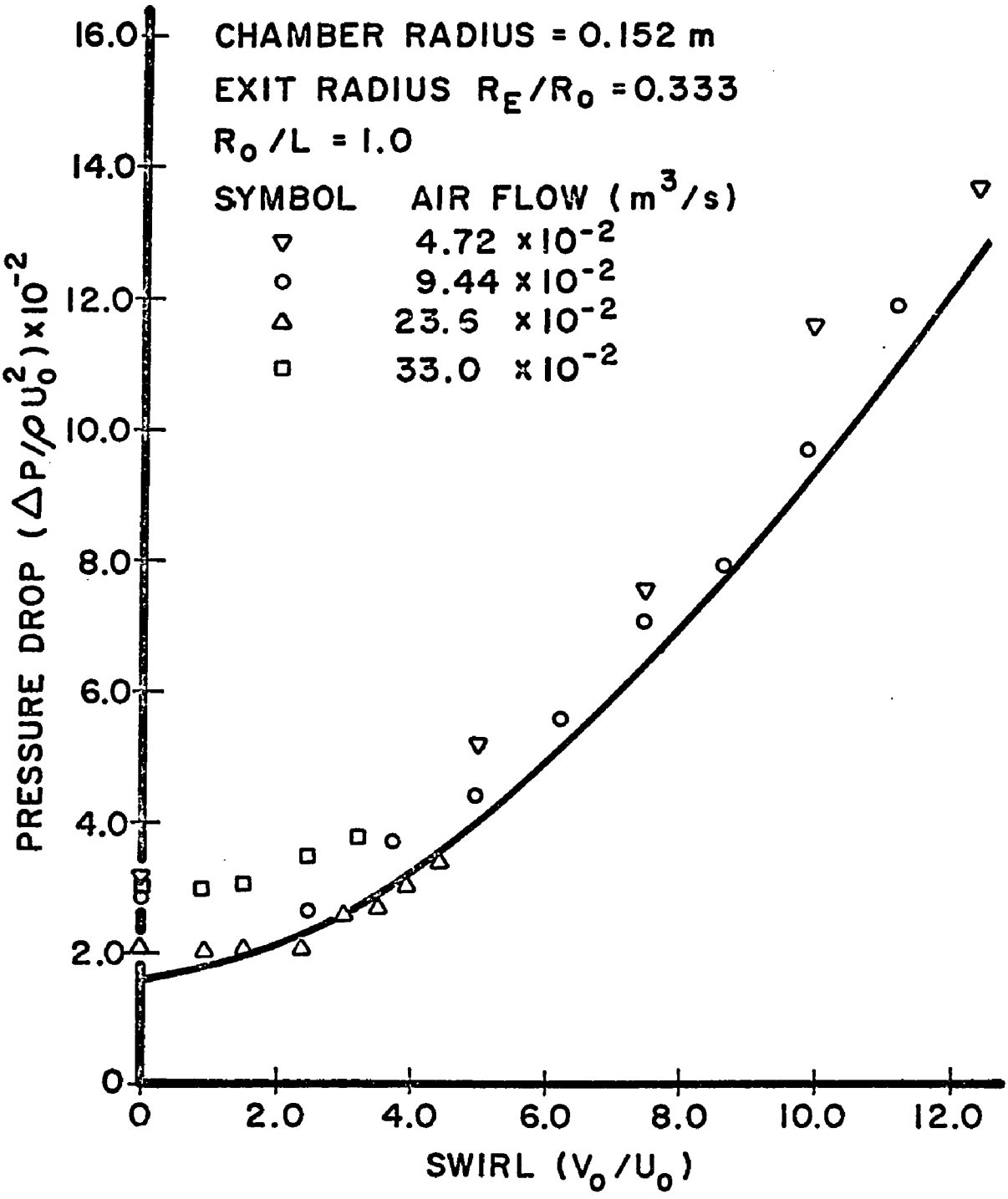

Figure 43c Chamber pressure drop

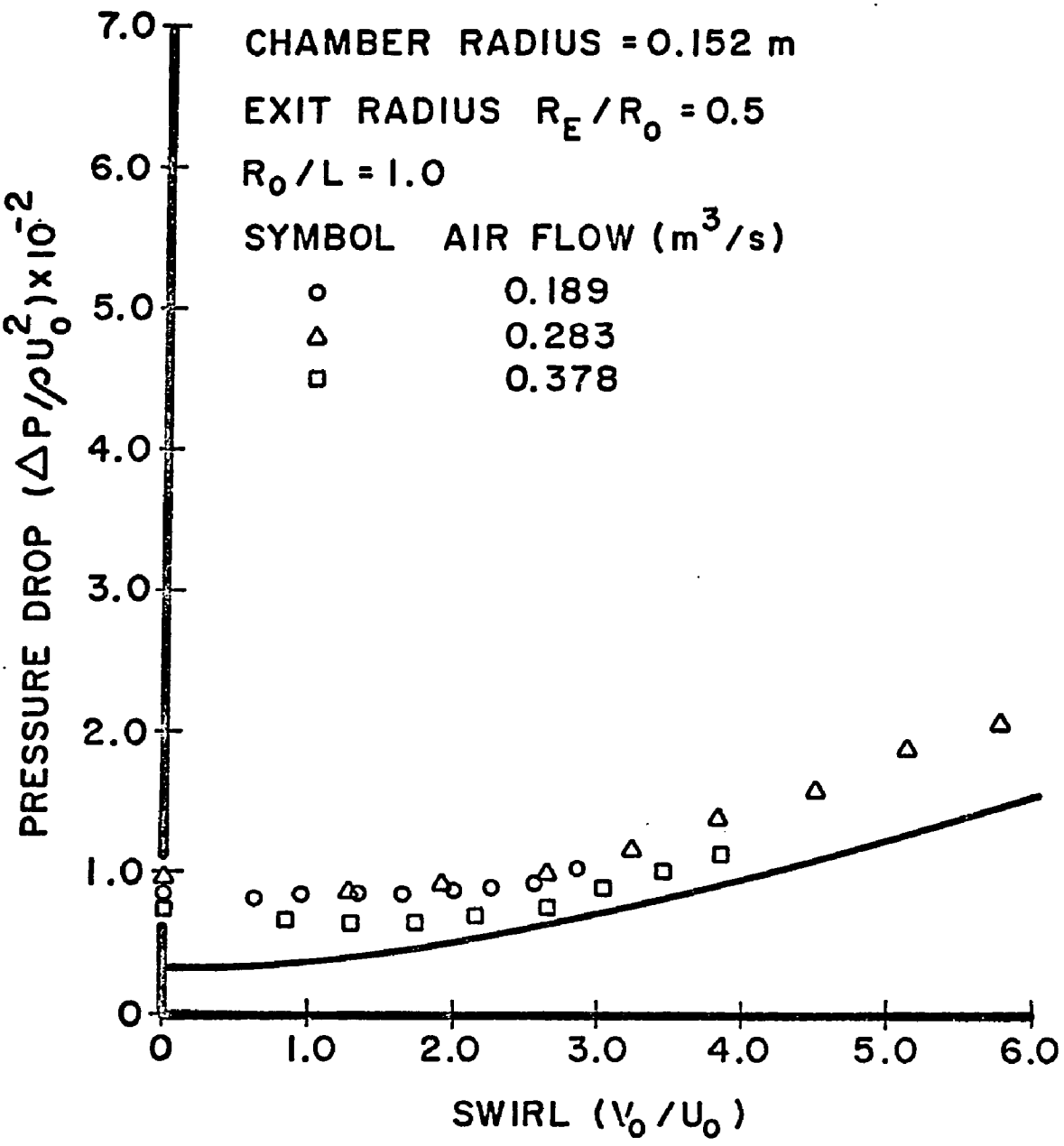

Figure 43d Chamber pressure drop

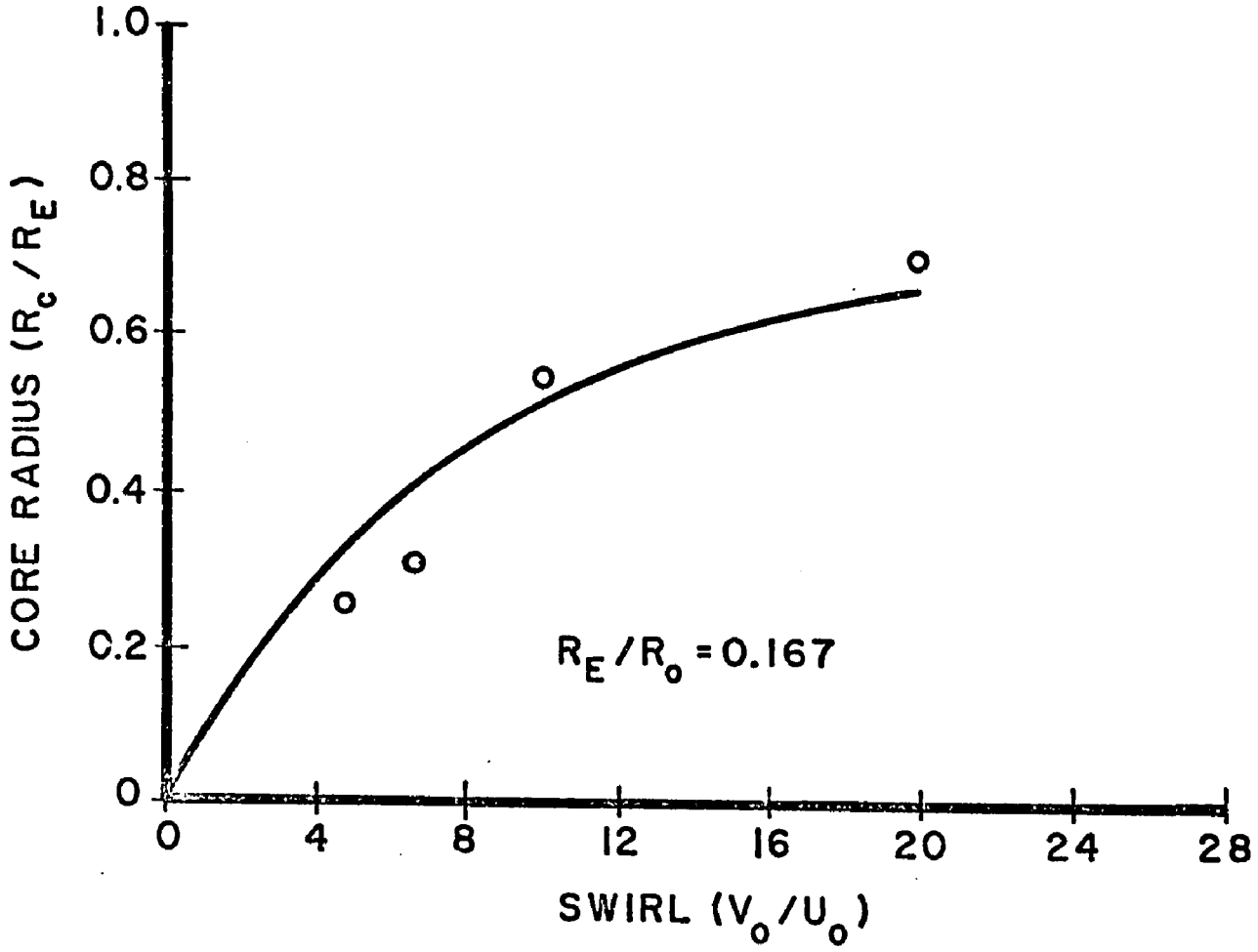

Figure 44a Core size variation with swirl

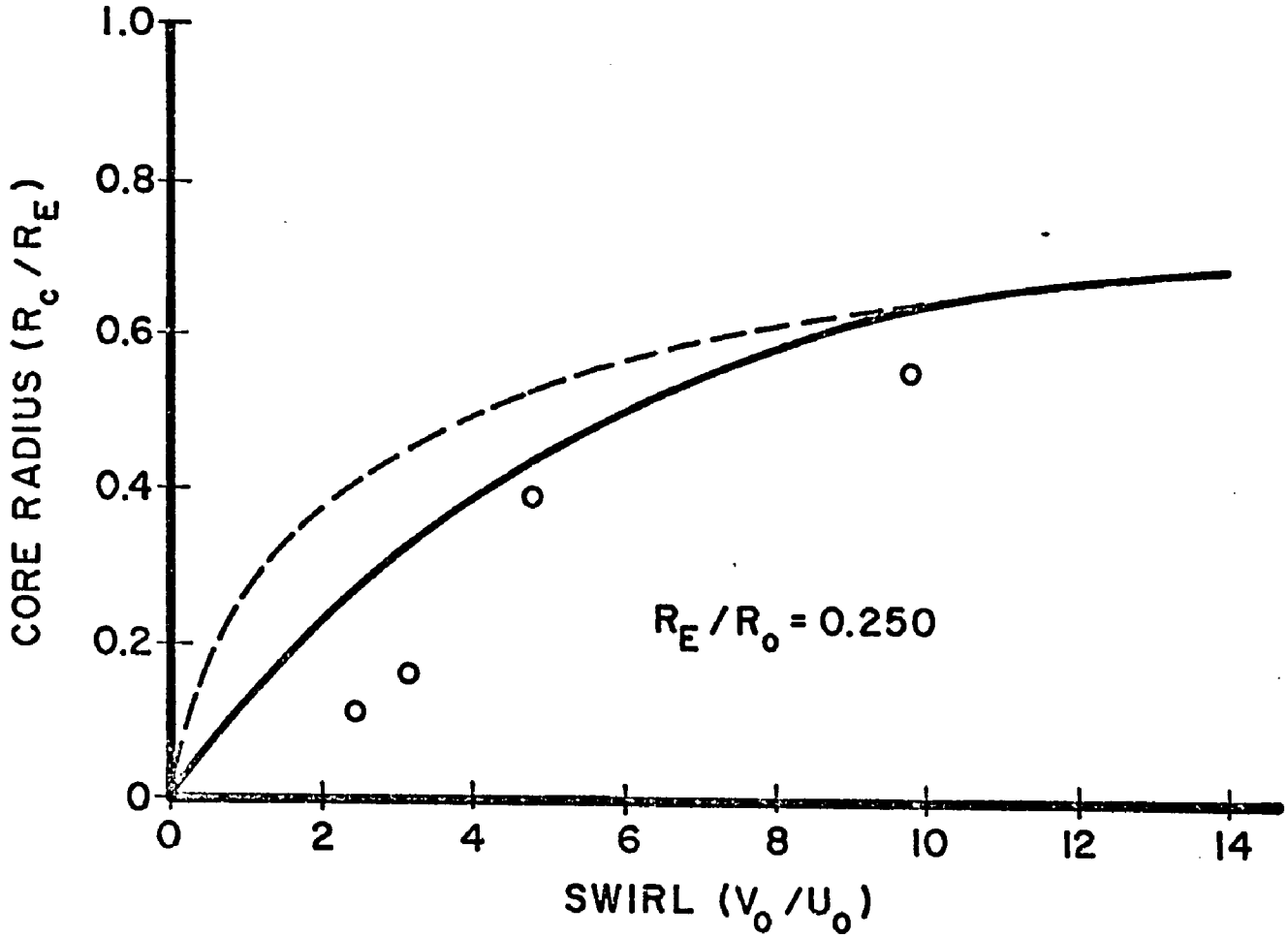

Figure 44b Core size variation with swirl

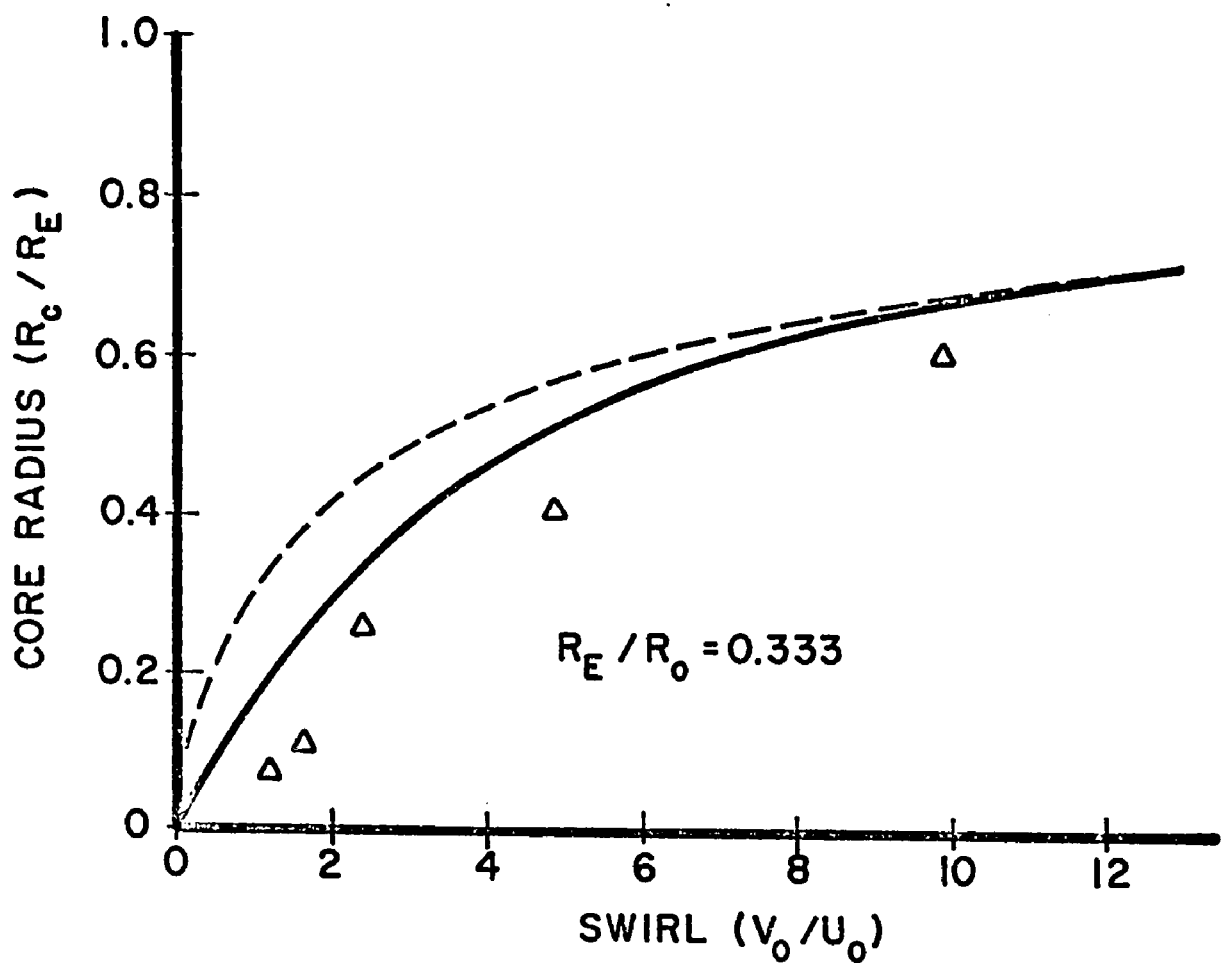

Figure 44c Core size variation with swirl

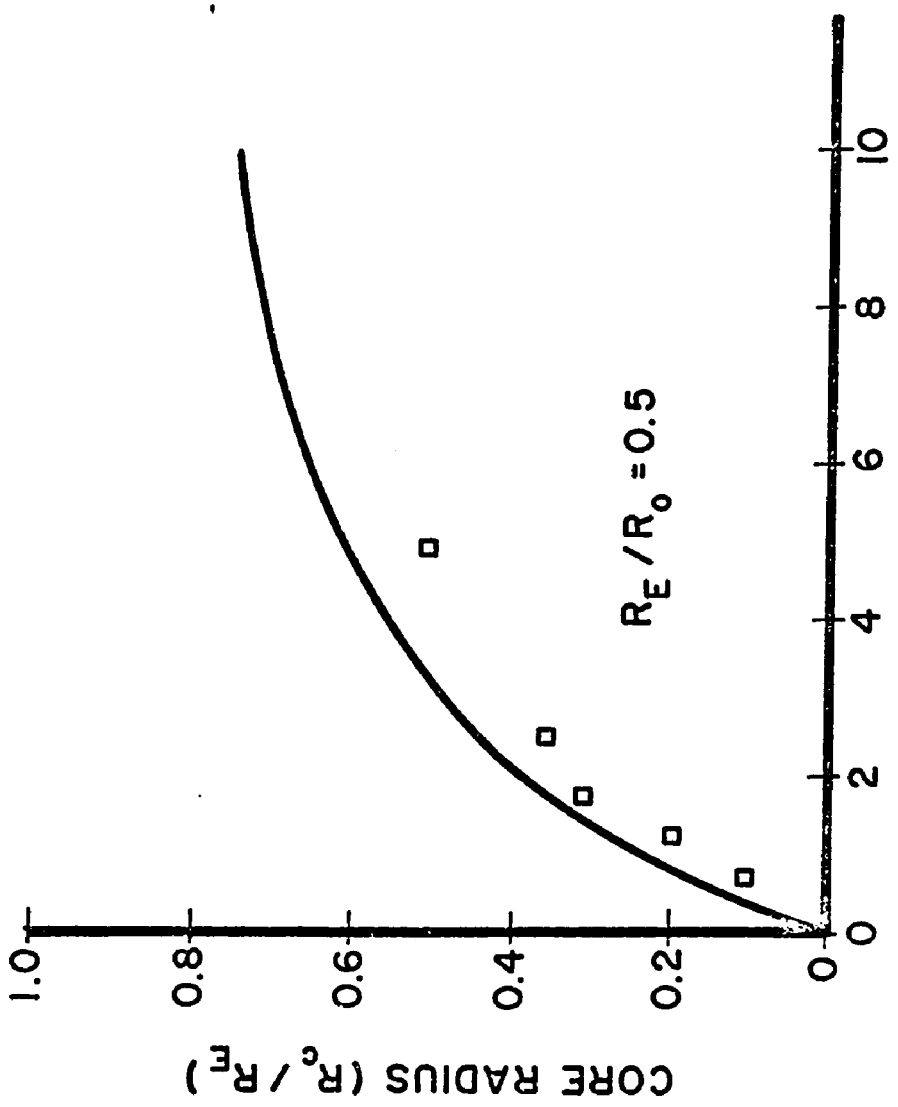

Figure 44d Core size variation with swirl

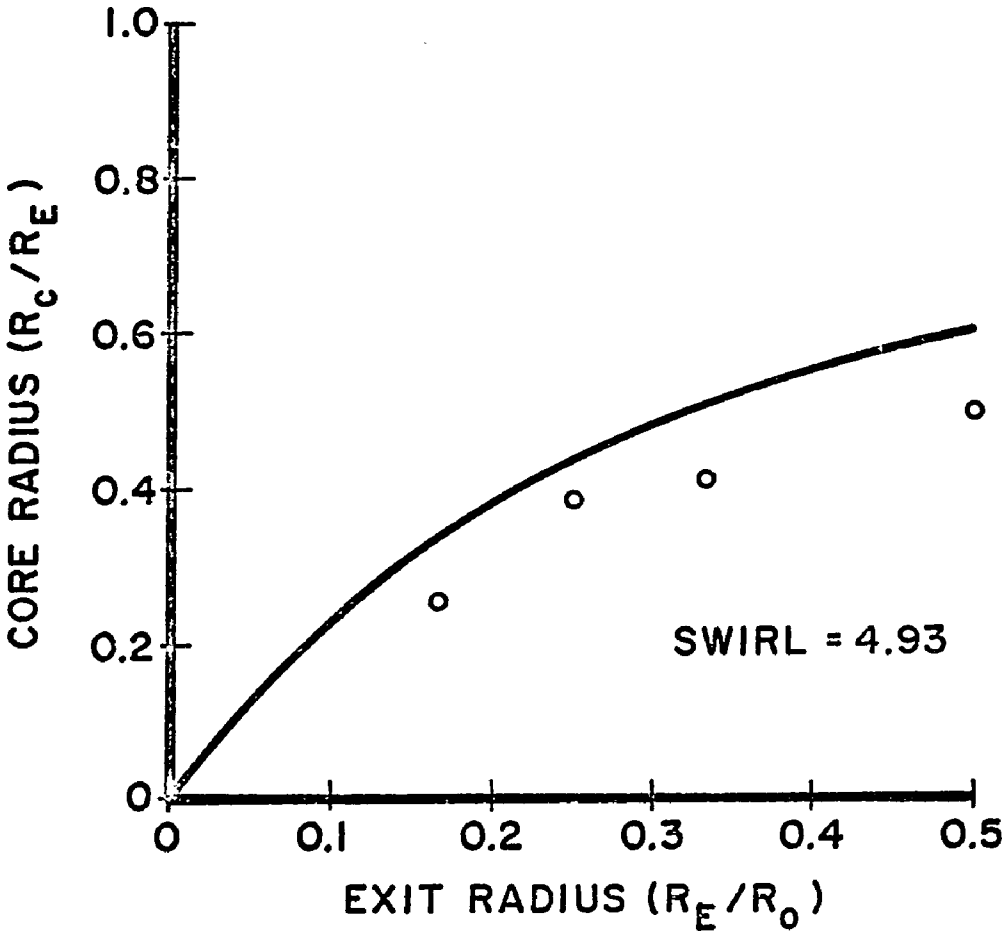

Figure 45 Core size variation with exit radius

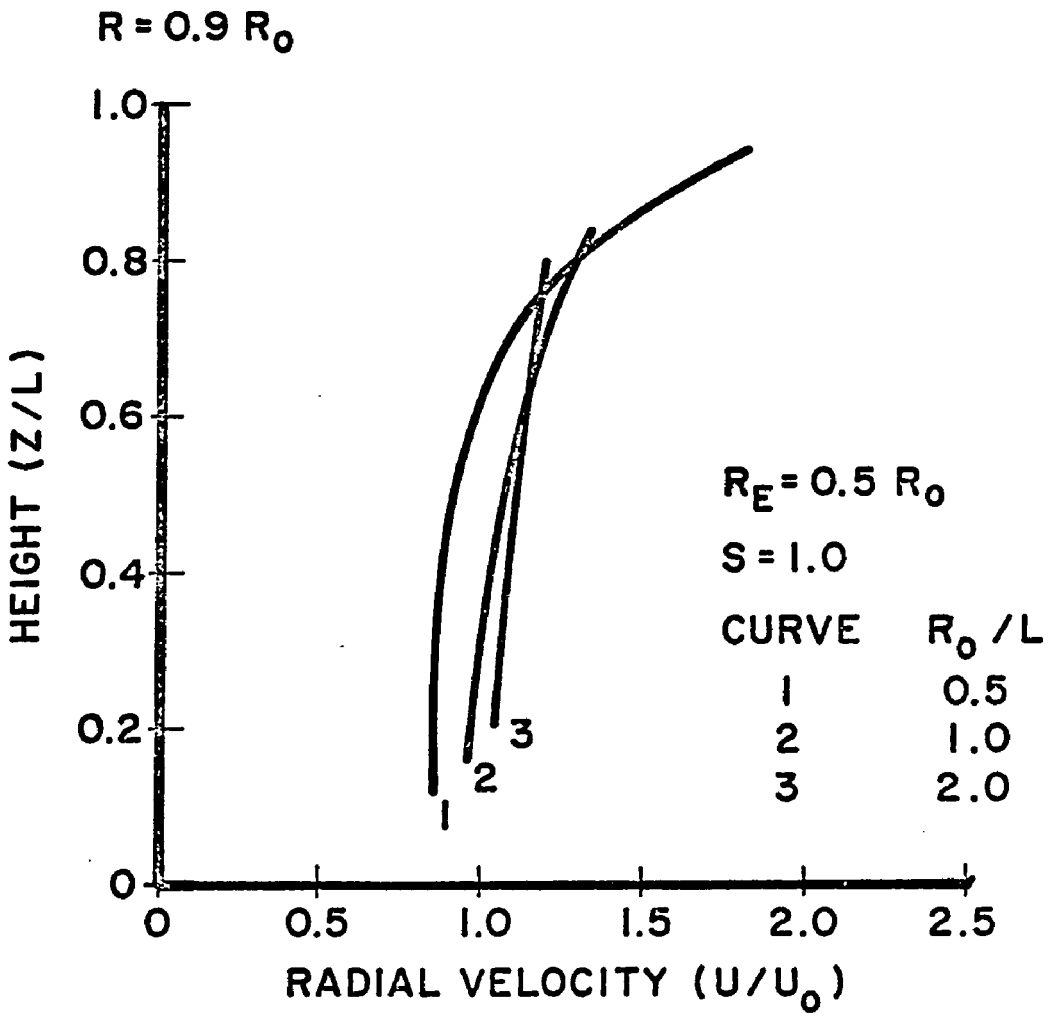

Figure 46a Parametric velocity profile

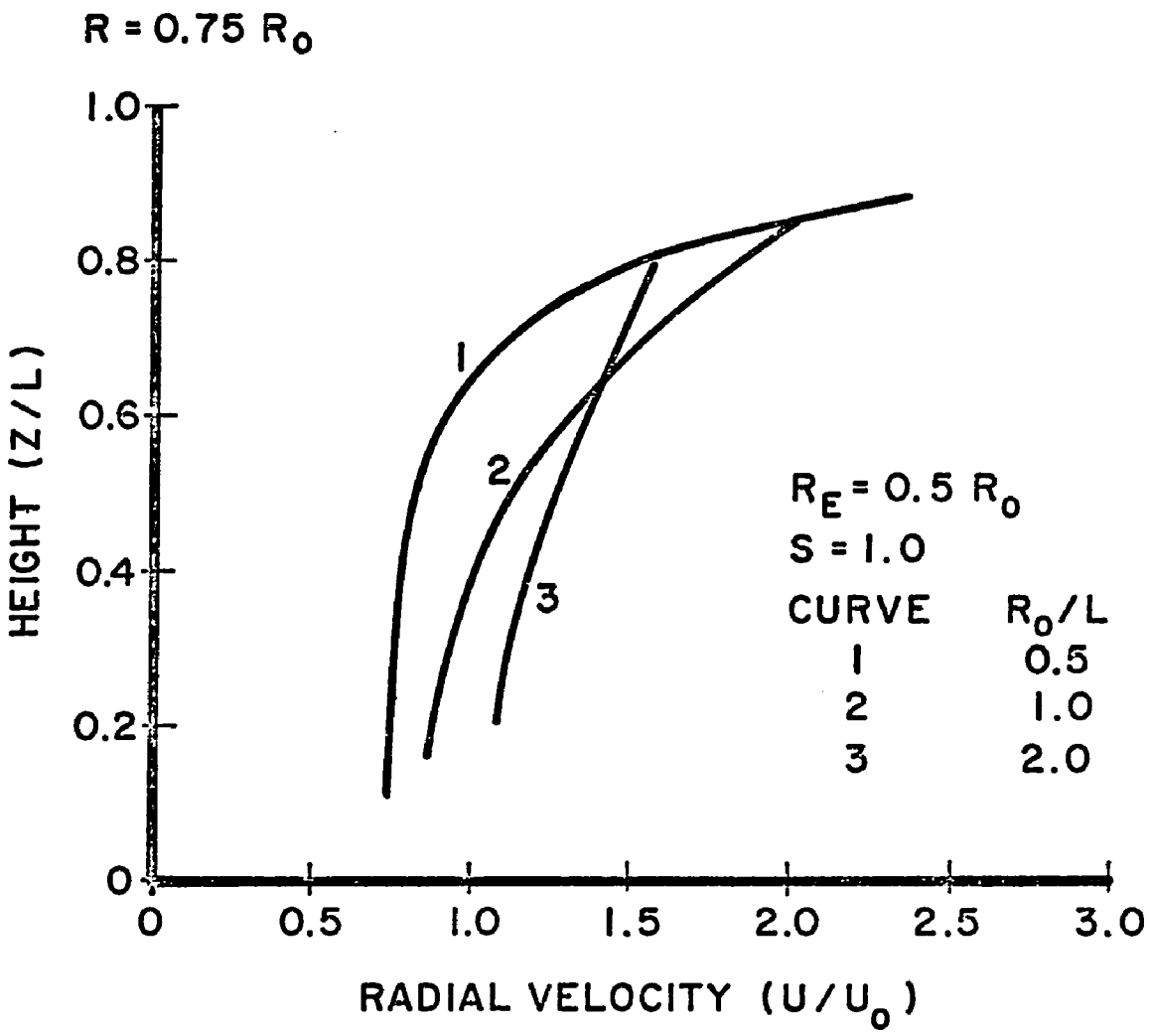

Figure 46b Parametric velocity profiles

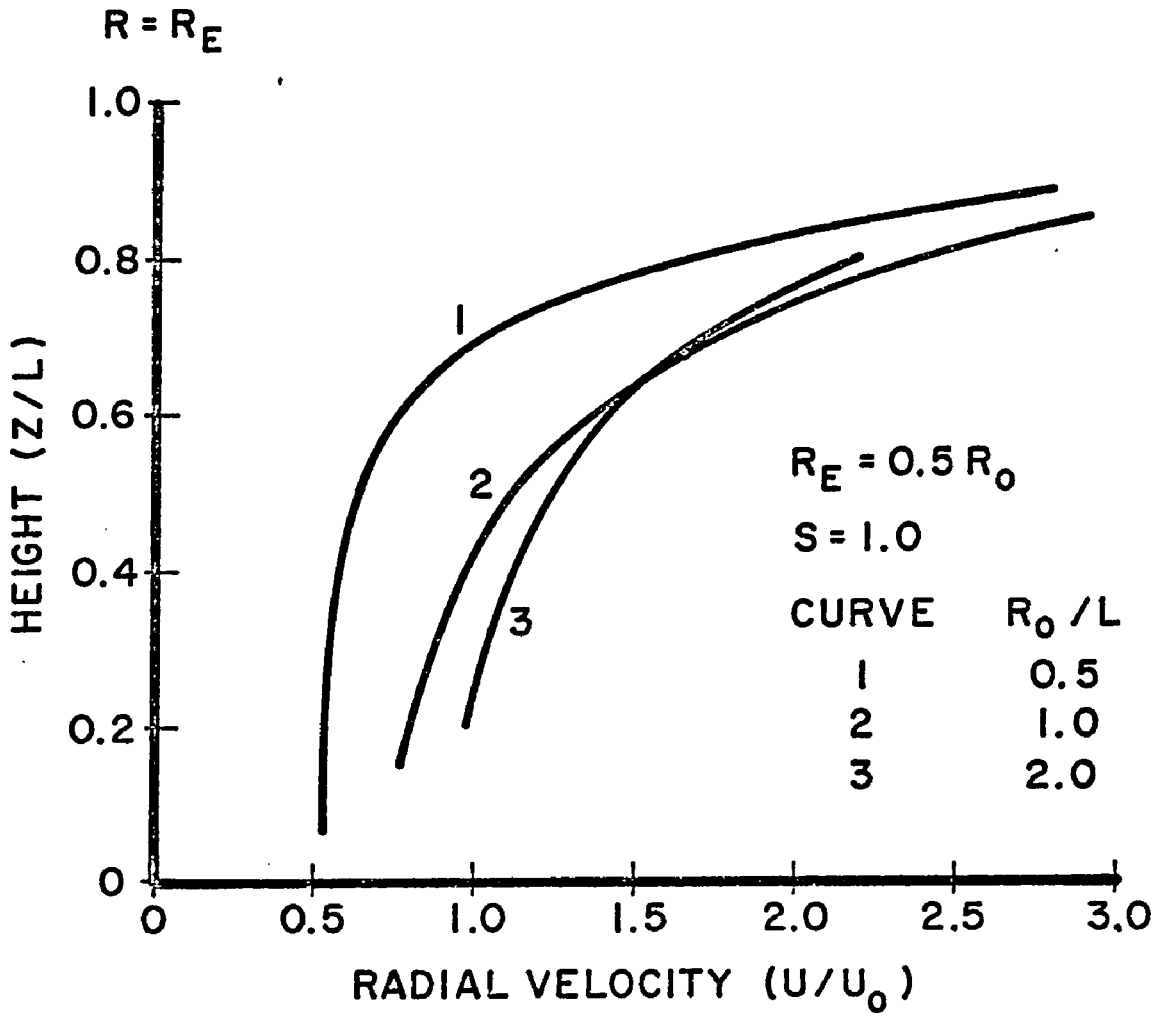

Figure 46c Parametric velocity profiles

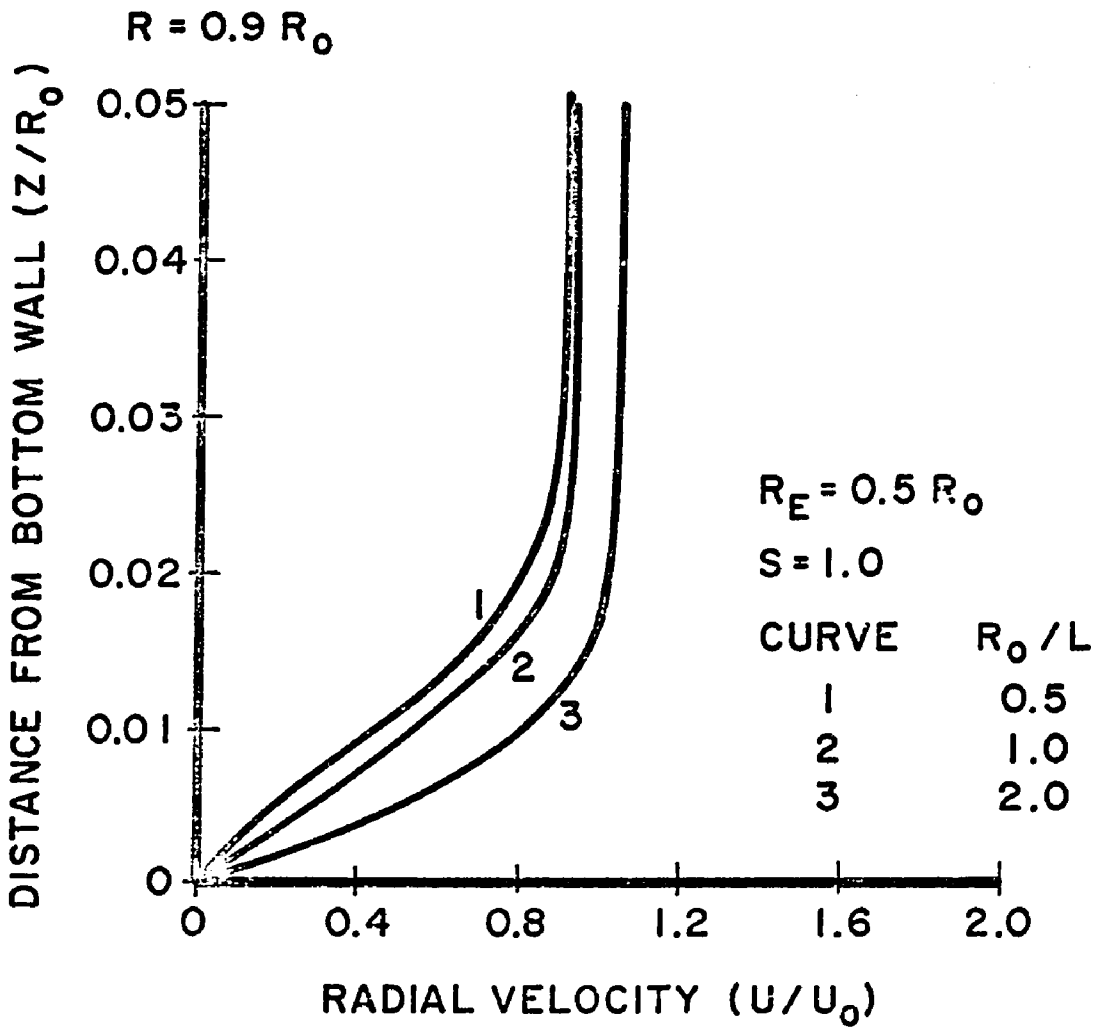

Figure 46d Parametric velocity profiles

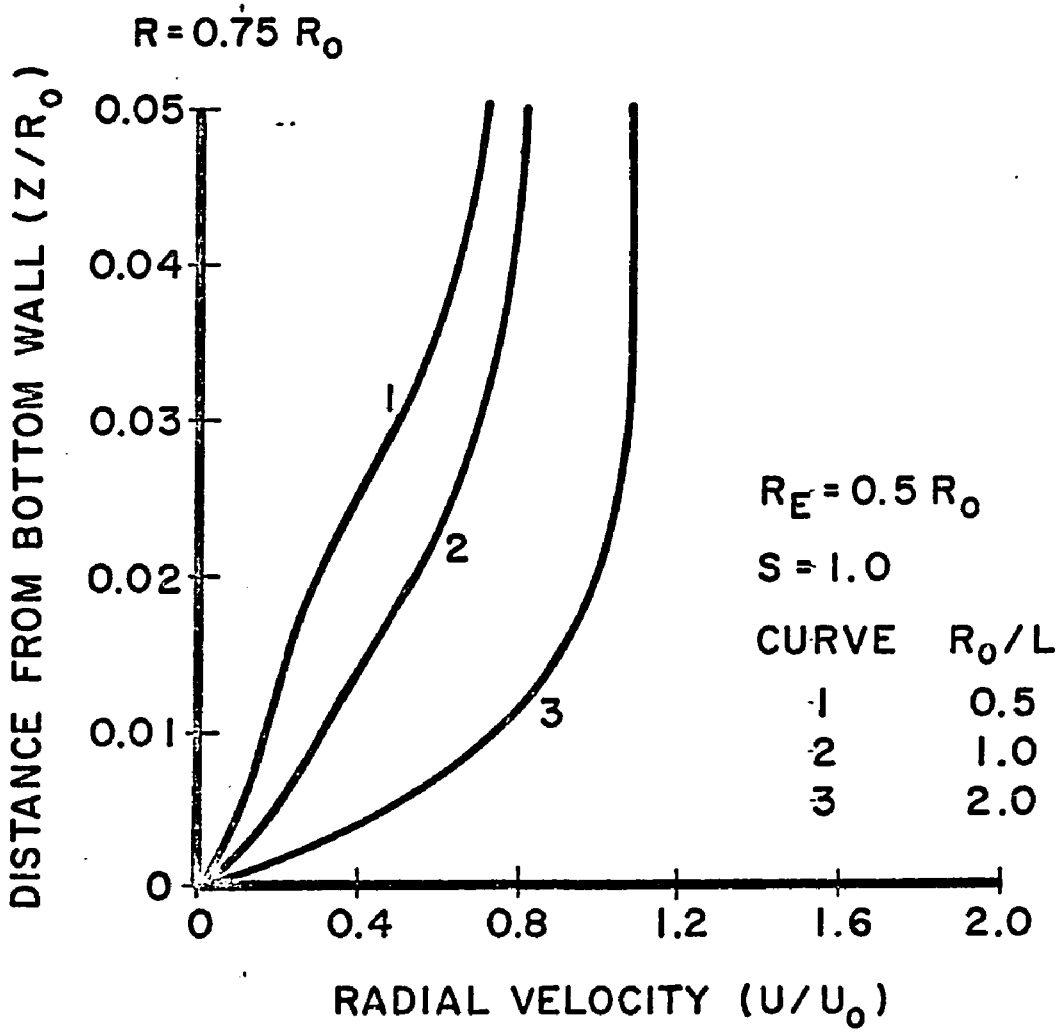

Figure 46e Parametric velocity profiles

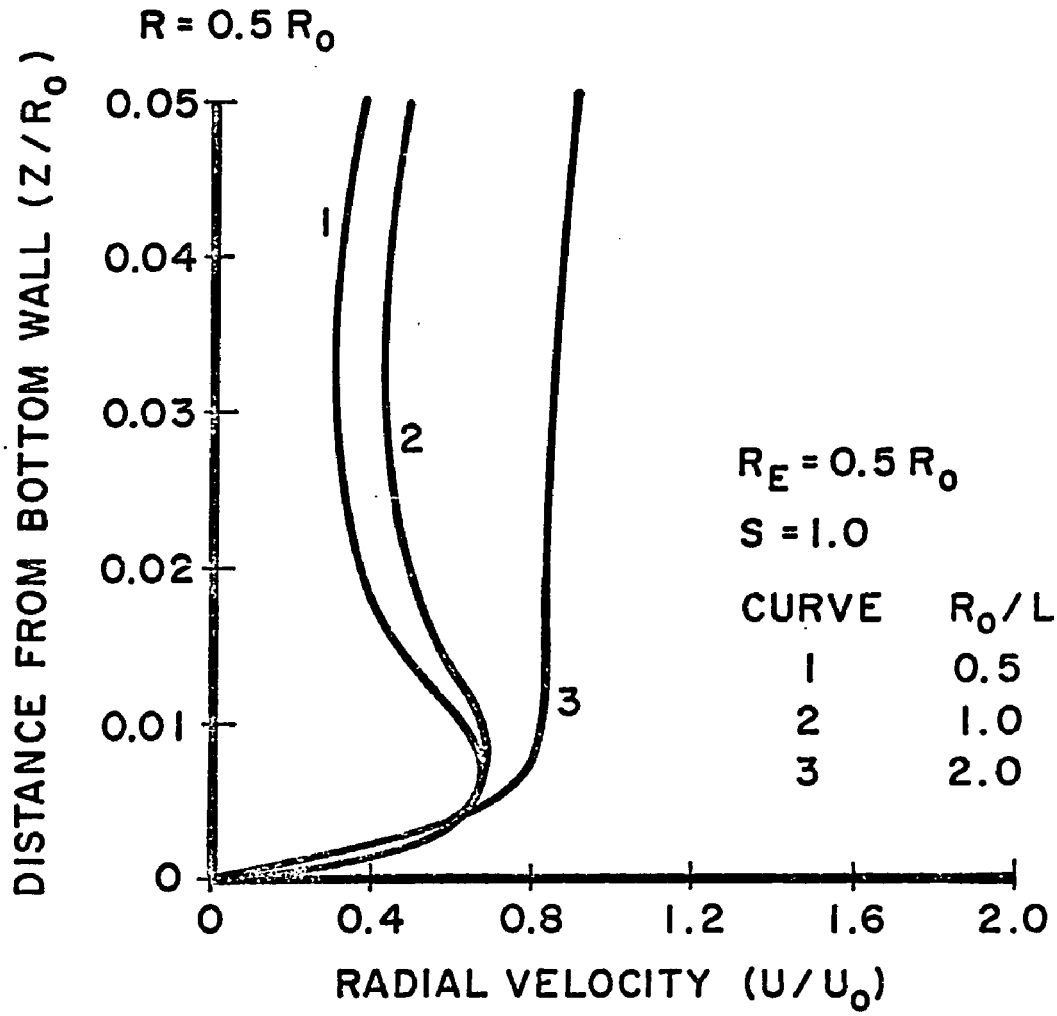

Figure 46f Parametric velocity profiles

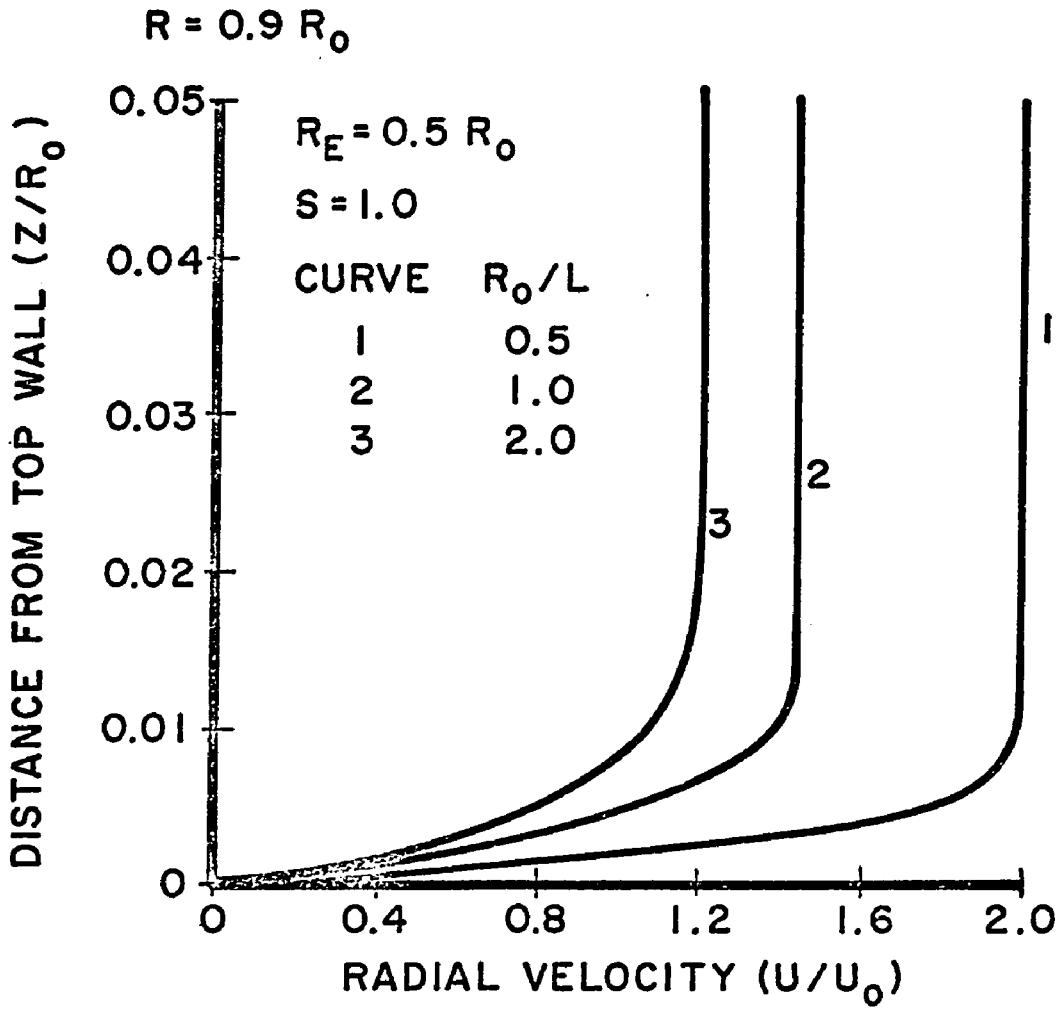

Figure 46g Parametric velocity profiles

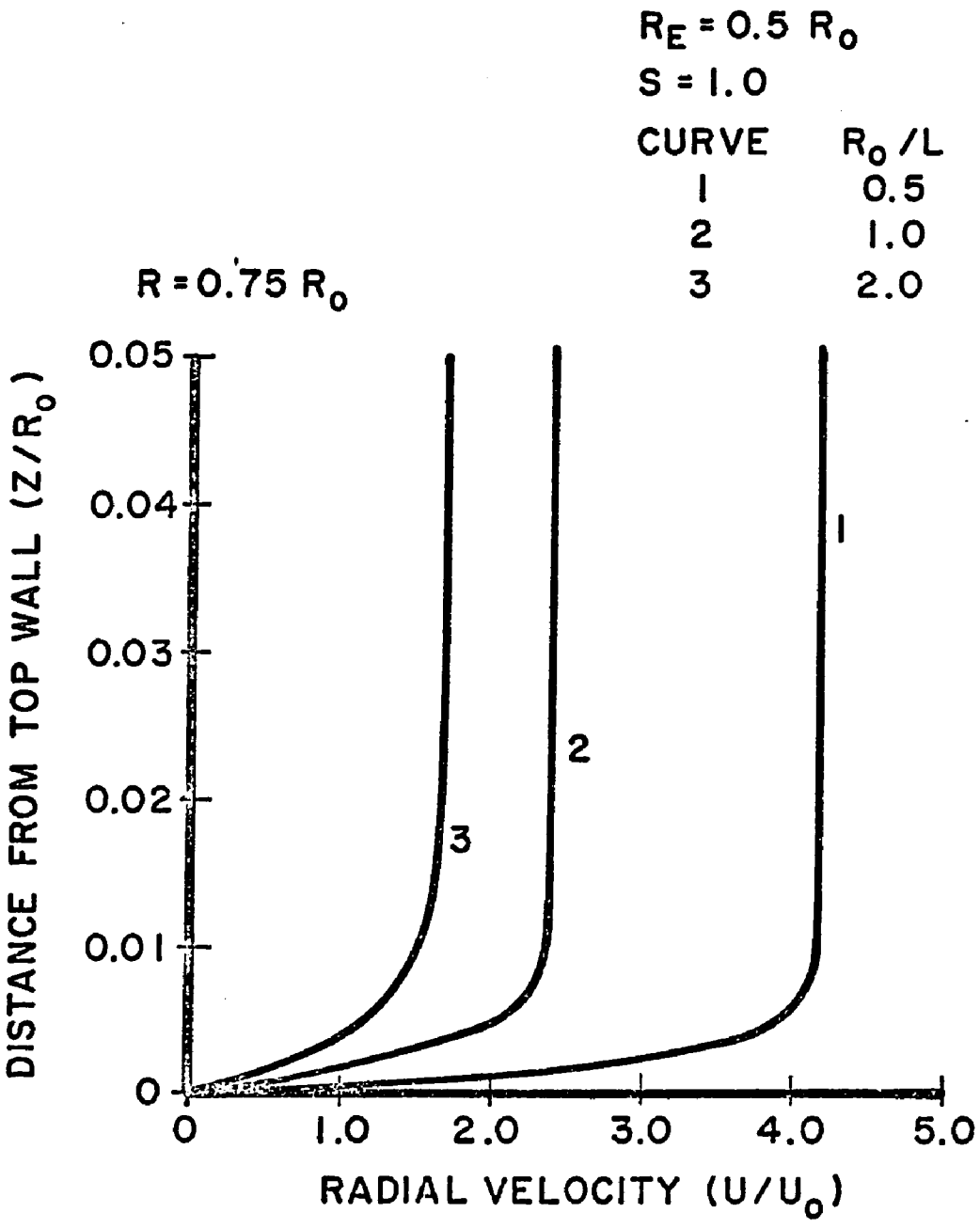

Figure 46h Parametric velocity profiles

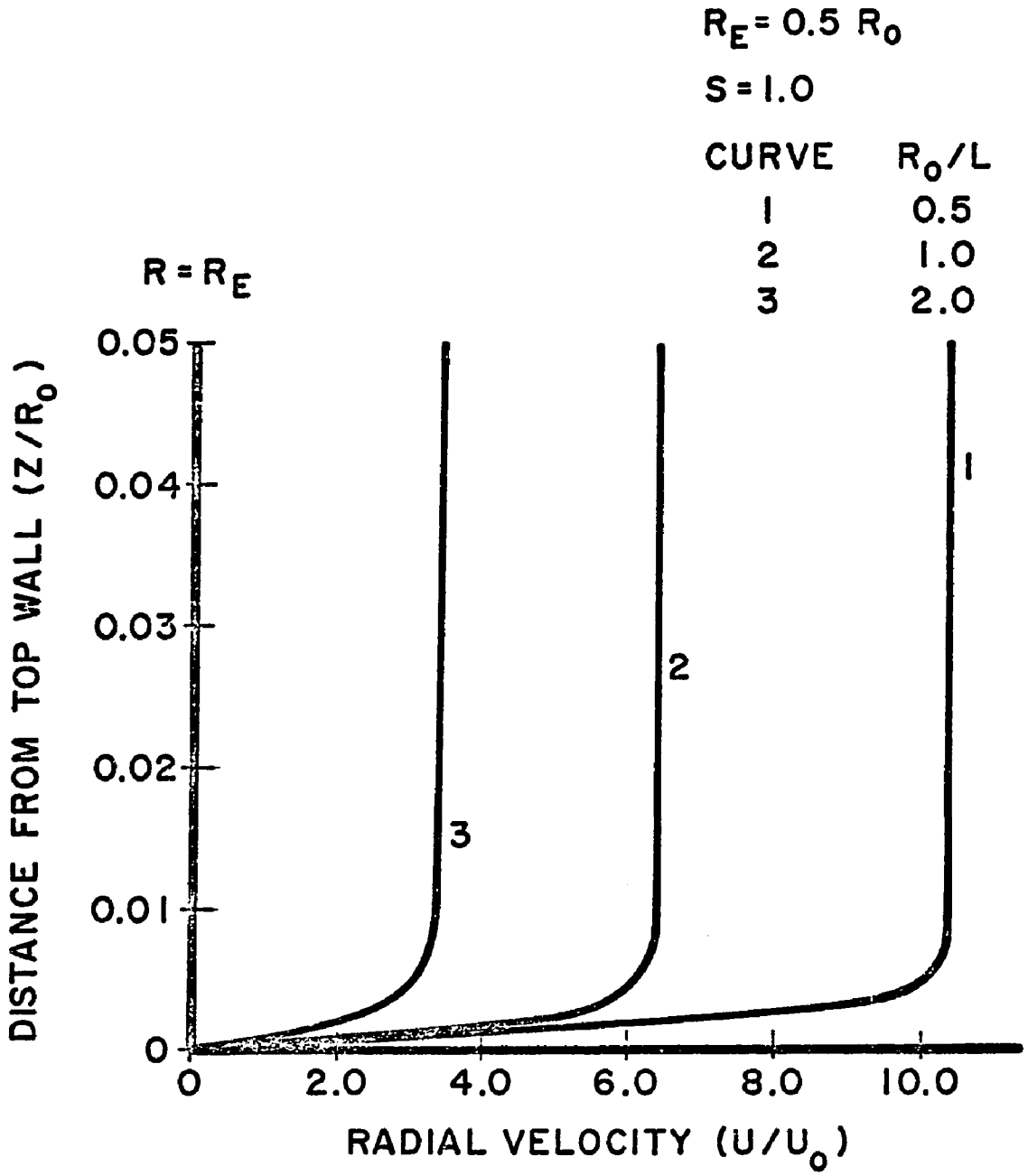

Figure 46i Parametric velocity profiles

REFERENCES

1. Levy, E., et al., "Centrifugal Fluidized Bed Combustion," Proceedings Fifth International Conference on Fluidized Bed Combustion, Washington, D.C., December 1977.

2. Kroger, D., Levy, E., and Chen, J., "Flow Characteristics in Packed and Fluidized Rotating Beds," to be published in Powder Technology.

3. Metcalfe, C. and Howard, J., "Combustion Experiments within a Rotating Fluidized Bed," Proceedings 1977 International Fluidized Bed Combustion Conference, Washington, D.C., December 1977.

4. Lewellen, W. S., A Review of Confined Vortex Flows, NASA CR 1772, 1971.

5. Ying, S. J. and Chang, C. C., "Exploratory Model Study of Tornado Like Vortex Dynamics," J. Atm. Sci., Vol. 27, No. 1, 1970, p. 3.

6. Wan, C. A. and Chang, C. C., "Measurement of the Velocity Field in a Simulated Tornado Like Vortex Using a Three-Dimensional Velocity Probe," J. Atm. Sci., Vol. 29, No. 1, 1972, p. 116.

7. Kotas, T. J., "An Experimental Study of the Three-Dimensional Boundary Layer on the End Wall of a Vortex Chamber," Proc. R. Soc. London, A, Vol. 352, 1976, p. 169.

8. Rott, N., "On the Viscous Core of a Line Vortex," ZAMP, Vol. IXb, 1958, p. 543.

9. Smithson, I. K., "Some Pressure Characteristics of Confined Vortex Flow," J. Inst. Fuel, March 1972, p. 47.

10. Roschke, E. J. and Pivirotto, T. J., "End Wall Pressure Distributions in a Confined Vortex," AIAA J., Vol. 5, No. 4, 1967, p. 817.

11. Donaldson, C. DuP. and Snedeker, R. S., Experimental Investigation of the Structure of Vortices in Simple Cylindrical Vortex Chambers, ARAP Report No. 47, 1962.

12. Savino, J. M. and Keshock, E. G., Experimental Profiles of Velocity Components and Radial Pressure Distributions in a Vortex Contained in a Short Cylindrical Chamber, NASA, TN D-3072, 1965.

13. Kuo, H. L., "Axisymmetric Flows in the Boundary Layer of a Maintained Vortex," J. Atm. Sci., Vol. 28, No. 1, 1971, p. 20.

14. DISA Electronics, Anemometer 55D01 Instruction Manual.

15. The IMSL Library, Houston, Texas.

16. Johnson, N. L. and Leone, F. C., Statistics and Experimental Design in Engineering and the Physical Sciences, John Wiley and Sons, 1977.

17. Schlichting, H., Boundary-Layer Theory, McGraw Hill, 1968.

18. Wills, J. A. B., "The Correction of Hot Wire Readings for Proximity to a Solid Boundary," J. Fluid Mech., Vol. 12, 1962.

19. Hornbeck, R. W., Viscous Flow in a Short Cylindrical Vortex Chamber with a Finite Swirl Ratio, NASA TN D-5132, 1969.

20. Hoffman, J. A., "Similarity Solutions for the Interaction of a Potential Vortex with Free Stream Sink Flow and a Stationary Surface,", Trans. ASME, Vol. 96, Series I, No. 1, 1974, p. 49.

21. Burggrat, O. R., Stewartson, K. and Belcher, R., "Boundary Layer Induced by a Potential Vortex," Physics of Fluids, Vol. 14, No. 9, 1971, p. 1821.

22. Pao, H. P., "A Numerical Computation of a Confined Rotating Flow," Trans. ASME, Vol. 41, Series E, No. 2, June 1974, p. 480.

23. Farris, G. J., Kidd, G. J., Lick, D. W. and Textor, R. E., "A Theoretical and Experimental Study of Confined Vortex Flow," Trans. ASME, Vol. 36, Series E, No. 4, 1969, p. 687.

24. Wormley, D. N., "An Analytical Model for the Incompressible Flow in Short Vortex Chambers," ASME Trans., Vol. 91, Series D, No. 2, 1969, p. 264.

25. Rogers, M. H. and Lance, G. N., "The Boundary Layer on a Disk of Finite Radius in a Rotating Fluid," Quart. J. Mech. and Appl. Math., Vol. XVII, Pt. 3, 1964, p. 319.

26. Roschke, E. J. and Pivirotto, T. J., Similarity in Confined Vortex Flows, JPL Tech. Rep. No. 32-789, 1965.

27. Roschke, E. J., Flow Visualization Studies of a Confined Jet-Driven Water Vortex, JPL Tech. Rep. No. 32-1004, 1966.

28. Serrin, J., "The Swirling Vortex," Phil. Trans. R. Socl, Lond. A. Vol. 271, 1972, p. 325.

29. Greenspan, H. P., The Theory of Rotating Fluids, Cambridge U. Press, 1968.

30. Baird, D. C., Experimentation: An Introduction to Measurement Theory and Experiment Design, Prentice-Hall, 1962.

31. Carnahan, B., Luther, H. A. and Wilkes, J. O., Applied Numerical Methods, John Wiley and Sons, 1969.

APPENDIX A

Error Propagation in Three-Dimensional Hot Wire Anemometer Measurements

An estimate of the uncertainty of the experimental procedure is required. The purposes are to gain information as to the reliability of the final results and to aid in making the measurements in the most accurate way possible.

The values of velocity which are calculated from the measured hot wire anemometer voltages could contain error due to:

a) Inaccurate voltage readings

b) Incorrect angular calibration constants K_1, K_2

c) Incorrect calibration of sensing elements

The effect of the above uncertainties on the results may also depend on the orientation of the probe with respect to the measured velocity and on the magnitude of the measured velocity. Baird [30] presents a discussion of the propagation of uncertainty with emphasis on the statistical probability of uncertainty in the results. Following this development consider the y component of velocity (Figure).

$$U_y^2 = (E_1, E_2, E_3, K_1, K_2, A_1, B_1, N_1 \cdots)$$

The standard deviation of U_y, S_{U_y}, may be calculated with a given number, N, of perturbations δU_y as

$$S_{u_y} = \sqrt{\frac{\varepsilon(\delta u_y)^2}{\nu}}$$

Given a small deviation in voltages E_1, E_2, E_3. The effect on U_y may be found

$$(Su_y)^2 = \left[\frac{\partial u_y}{\partial E_1} SE_1 + \frac{\partial u_y}{\partial E_2} SE_2 + \frac{\partial u_y}{\partial E_3} SE_3\right]^2$$

and

$$S^2_{u_y} = \frac{1}{N} \Sigma \left[\left(\frac{\partial u_y}{\partial E_1} SE_1\right)^2 + \left(\frac{\partial u_y}{\partial E_2} SE_2 \frac{\partial u_y}{\partial E_1} SE_1\right) + \left(\frac{\partial u_y}{\partial E_3} SE_1 \frac{\partial u_y}{\partial E_1} SE_L\right)\right.$$

$$+ \left(\frac{\partial u_y}{\partial E_2} SE_2 \frac{\partial u_y}{\partial E_1} SE_1\right) + \left(\frac{\partial u_y}{\partial E_2} SE_2\right)^2 + \left(\frac{\partial u_y}{\partial E_3} SE_3 \frac{\partial u_y}{\partial E_2} SE_2\right)$$

$$\left. + \left(\frac{\partial u_y}{\partial E_3} SE_3 \frac{\partial u_y}{\partial E_1} SE_1\right) + \left(\frac{\partial u_y}{\partial E_3} SE_3 \frac{\partial u_y}{\partial E_2} SE_2\right) + \left(\frac{\partial u_y}{\partial E_2} SE_3\right)^2\right]$$

Since perturbations SE_1, SE_2 and SE_3 are presumably independent

$$\Sigma\, SE_i SE_j = 0 \qquad i \neq j$$

Also

$$\frac{\epsilon(SE_1)^2}{N} = SE_1^2 \qquad \frac{\epsilon(SE_2)^2}{N} = SE_2^2 \qquad \frac{\epsilon(SE_3)^2}{N} = SE_2^2$$

hence

$$S^2_{u_y} = \left(\frac{\partial u_y}{\partial E_1} SE_1\right)^2 + \left(\frac{\partial u_y}{\partial E_2} SE_2\right)^2 + \left(\frac{\partial u_y}{\partial E_3} SE_3\right)^2$$

$$u_y^2 = f\left(u_1(E_1, K_1, K_2) \;,\; u_2(E_2, K_1, K_2) \;,\; u_3(E_3, K_1, K_2)\right)$$

$$\frac{\partial u_y}{\partial E_1} \doteq \frac{1}{2} f^{-1/2} \frac{\partial f}{\partial u_1} \frac{\partial u_1}{\partial E_1} \;, \ldots$$

The functions $U_1(E_1, E_2, E_3, K_1, K_2)$ are known from the calibration

data. In this way, an expression for the expected standard deviation of any of the velocity components with a deviation in any of the voltages or other parameters such as K_1 or K_2 may be obtained. The expected uncertainties in the measured parameters are:

$$SK_1 = 0.02$$

$$SK_2 = 0.005$$

$$SE_i = 0.01 \text{ volts}$$

The dependence of the expected error in a velocity component as a function of the deviations in measured voltage or K_1 and K_2 is shown in Figures and . The sensitivity of the error propagation to the orientation of the probe is shown in Figure .

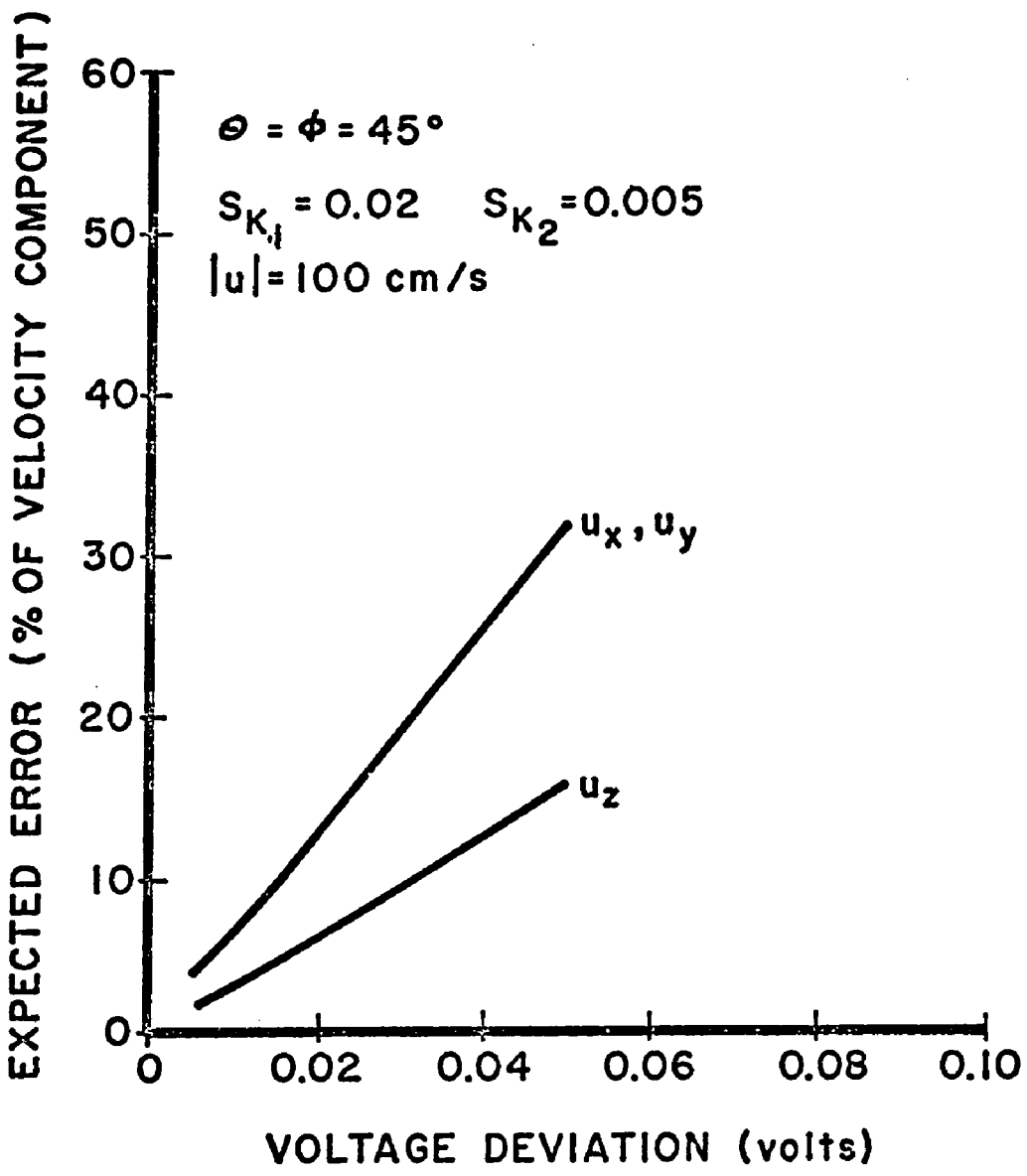

Figure A1 Sensitivity of error to voltage deviation

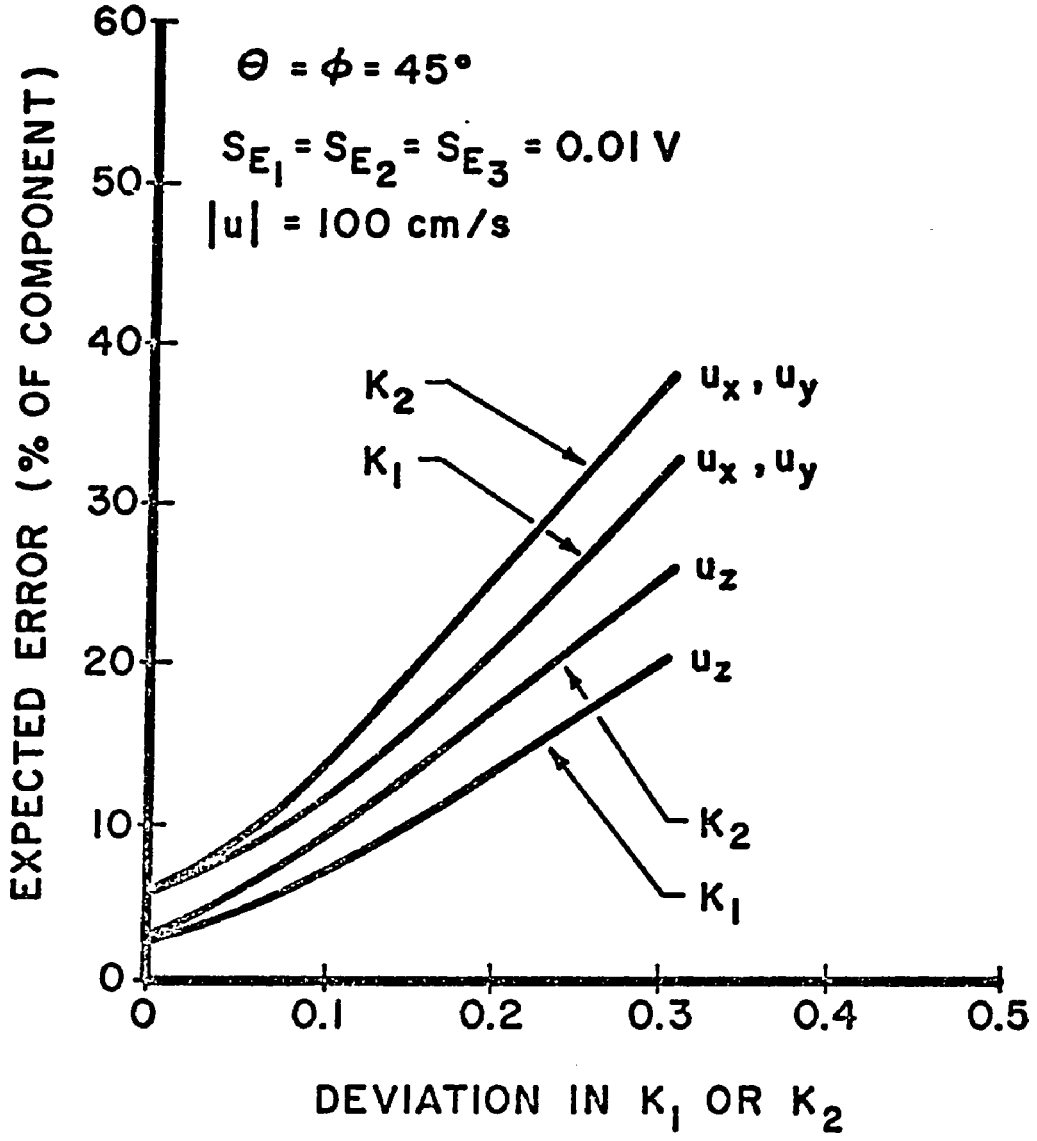

Figure A2 Sensitivity of error to deviation of K_1 or K_2

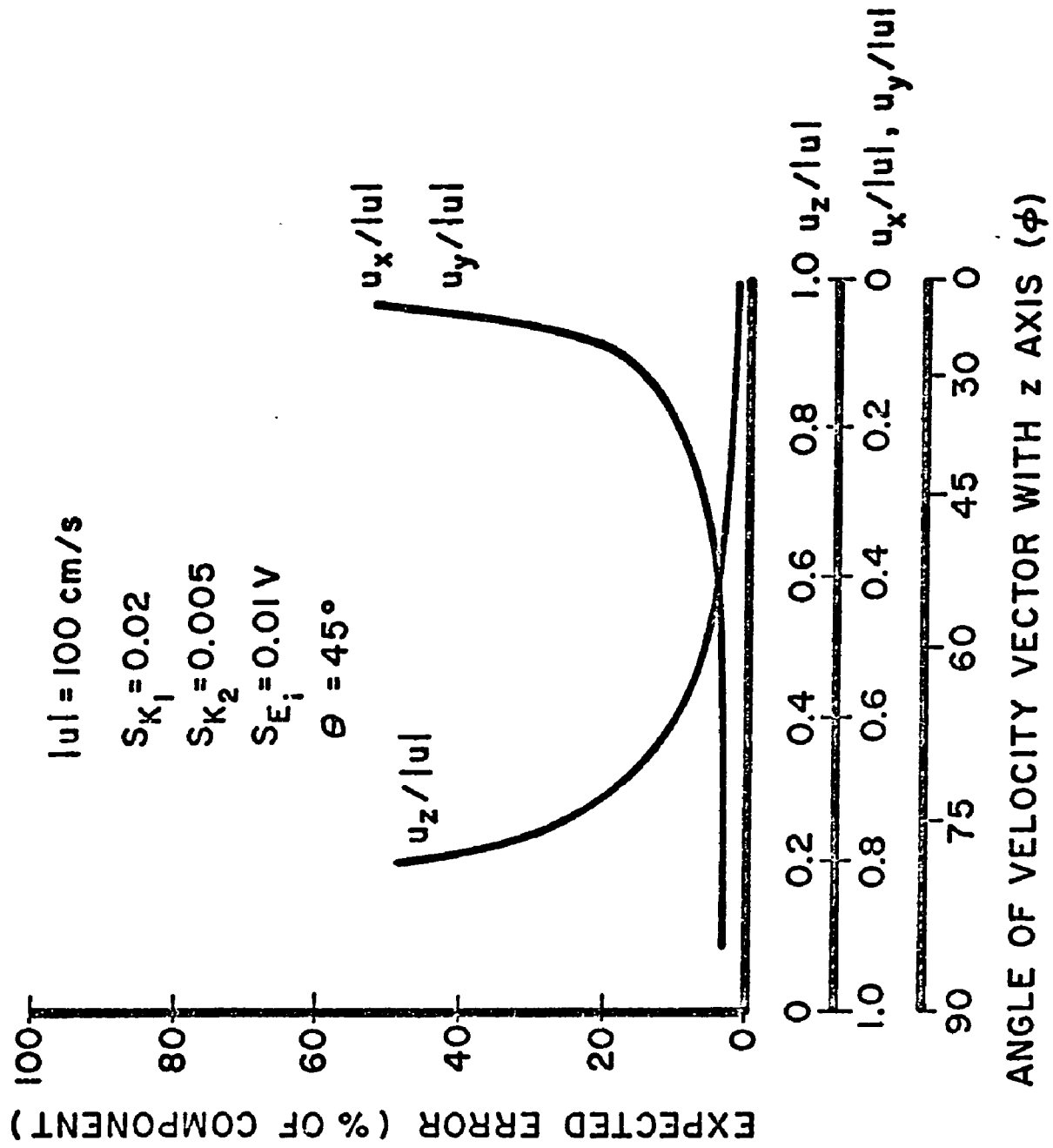

Figure A3 Sensitivity of error to orientation

APPENDIX B

Deviation of Finite Difference Approximations

Approximations to the derivatives are obtained using the Taylor series expansions for the function about a specified position. The approximations are categorized with respect to the use of neighboring points. When only points behind the desired position are used, the result is termed a backward difference, for points ahead, forward difference, and when both are used a centered difference. To preserve the most general form for the approximations, no assumptions will be made concerning the size of the intervals, each interval will be denoted by a subscript linking it with the particular grid position.

i-1	Δx_i i	Δx_{i+1} i+1

let the ratio $x_{i-1}/x_i = a$ for all i and construct Taylor series expressions for the value of some function f at points close to point i:

$$f_{i+1} = f_i + \frac{\partial f_i}{\partial x}\Delta x_i + \frac{\partial^2 f_2}{\partial x^2}\frac{\Delta x_i^2}{2!} + \frac{\partial^3 f_i}{\partial x^3}\frac{\partial x_i^3}{3!} + O\Delta x_i^4 \qquad \text{(B1)}$$

$$f_{i+2} = f_i + \frac{\partial f_i}{\partial x}\Delta x_i(1+a) + \frac{\partial^2 f_i}{\partial x^2}\frac{\Delta x_i^2}{2!}(1+a)^2 + \frac{\partial^2 f_i}{\partial x^3}\frac{\Delta x_i^3}{3!}(1+a)^3 + O\Delta x_i^4 \qquad \text{(B2)}$$

$$f_{i-1} = f_1 - \frac{\partial f_i}{\partial x^2}\Delta x_i a + \frac{\partial^2 f_i}{\partial x^2}\frac{\Delta x_i^2}{2!}a^2 - \frac{\partial^3 f_i}{\partial x^3}\frac{\Delta x_i^3}{3!}a^3 + O\Delta x_i^4 \qquad \text{(B3)}$$

$$f_{i-2} = f_i - \frac{\partial f_i}{\partial x}\Delta x_i a(1+a) + \frac{\partial^2 f}{\partial x^2}\frac{\partial x_i^2}{2!}(a(1+a))$$

$$- \frac{\partial^3 f_i}{\partial x^3}\frac{\Delta x_i^3}{3!}(a(1+a))^3 + O\Delta x_i^4 \qquad \text{(B4)}$$

The expressions for the finite difference approximations will be denoted as first or second order correct but this is strictly true only if the grid is equally spaced.

First Derivative - First Order

$$\frac{\partial f_i}{\partial x} = \frac{f_{i+1} - f_i}{\Delta x_i} + O\Delta x_i \quad \text{(Forward from B1)} \qquad \text{(B5)}$$

$$\frac{\partial f_i}{\partial x} = \frac{f_i - f_{i-1}}{a\Delta x_i} + O\Delta x_i \quad \text{(Backward from B3)} \qquad \text{(B6)}$$

First Derivative - Second Order

Forward Difference (B1 and B2)

$$\frac{\partial f_i}{\partial x} = \frac{f_{i+1}(1+a)^2 - f_{i+2} - f_i a}{a(1+a)\Delta x_i} - O(\Delta x_i)^2 \qquad \text{(B7)}$$

Backward Difference (B3 and B4)

$$\frac{\partial f_i}{\partial x} = \frac{-f_{i-1}(1+a)^2 + f_{i-2} + f_i((1+a)^2-1)}{a^2(1+a)\Delta x_i} \qquad \text{(B8)}$$

Centered Difference (B1 and B3)

$$\frac{\partial f_i}{\partial x} = \frac{f_{i+1} - f_{i-1}}{(1+a)\Delta x_i} + O(\Delta x_i(1-a)) \qquad \text{(B9)}$$

Second Derivative - Second Order

Centered Difference

$$\frac{\partial^2 f_i}{\partial x^2} = \frac{a f_{i+1} - (a+1) f_i + f_{i-1}}{\frac{a}{2}(1+a)\Delta x_i^2} - O(\Delta x_i (1-a)) \qquad \text{(B10)}$$

In each case it can be seen that as $a \to 1$ the accuracy of the approximation improves.

VITA

Walter Jeffrey Shakespeare is the only son of Walter S. and Mildred N. Shakespeare. Born in Harrisburg, Pennsylvania on November 23, 1951, he graduated from Cedar Cliff High School in June of 1969 and entered Lehigh University in August of that year. Mr. Shakespeare received the Bachelor of Science degree in Mechanical Engineering with honors in May 1973 and began work as an Engineer Level I for the Pennsylvania Power and Light Company of Allentown, Pennsylvania, in June of that year. He returned to Lehigh to pursue graduate study in mechanical engineering in September 1975, under a National Science Foundation Energy Traineeship and received the Master of Science degree in May 1977. Study for the degree of Doctor of Philosophy was carried out under the direction of Professor Edward K. Levy. Mr. Shakespeare is currently employed by the Bell Telephone Laboratories in Holmdel, New Jersey.